

University of Louisville

ThinkIR: The University of Louisville's Institutional Repository

Electronic Theses and Dissertations

8-2021

Mixed metal oxide nanowires via solid state alloying.

Veerendra Atla
University of Louisville

Follow this and additional works at: <https://ir.library.louisville.edu/etd>



Part of the [Other Chemical Engineering Commons](#), and the [Other Materials Science and Engineering Commons](#)

Recommended Citation

Atla, Veerendra, "Mixed metal oxide nanowires via solid state alloying." (2021). *Electronic Theses and Dissertations*. Paper 3705.

Retrieved from <https://ir.library.louisville.edu/etd/3705>

This Doctoral Dissertation is brought to you for free and open access by ThinkIR: The University of Louisville's Institutional Repository. It has been accepted for inclusion in Electronic Theses and Dissertations by an authorized administrator of ThinkIR: The University of Louisville's Institutional Repository. This title appears here courtesy of the author, who has retained all other copyrights. For more information, please contact thinkir@louisville.edu.

MIXED METAL OXIDE NANOWIRES VIA SOLID STATE ALLOYING

By

Veerendra Atla

B.Tech., Jawaharlal Nehru Technological University, Hyderabad, India 2008

M.Tech., Indian Institute of Technology Bombay, India, 2010

A Dissertation

Submitted to the Faculty of the

J.B. Speed School of Engineering of the University of Louisville

In Partial Fulfillment of the Requirements

for the Degree of

Doctor of Philosophy in Chemical Engineering

Department of Chemical Engineering

University of Louisville

Louisville, KY 40292

August 2021

Copyright© 2021 by Veerendra Atla

All rights reserved

MIXED METAL OXIDE NANOWIRES VIA SOLID STATE ALLOYING

By

Veerendra Atla

B.Tech., Jawaharlal Nehru Technological University, Hyderabad, India 2008

M.Tech., Indian Institute of Technology Bombay, India, 2010

A Dissertation Approved on

July 27, 2021

By the following Dissertation Committee:

Dissertation Director
Dr. Mahendra Sunkara

Dr. Thomas Starr

Dr. Gautam Gupta

Dr. Jacek Jasinski

Dr. Farshid Ramezanipour

DEDICATION

I would love to dedicate this dissertation to my beloved wife *Sudharani Vedula*, my daughter *Manasvi Atla*, and my son *Ishan Atla* for their valuable support, and encouragement. They always been a great source of inspiration.

ACKNOWLEDGMENTS

I would like to thank my advisor Prof. Mahendra Sunkara for his continued support, encouragement, and motivation throughout this PhD work. Most of the thesis experimental work was performed at advanced energy materials, LLC. The thesis concepts were developed and validated with the experimental work at advanced energy materials, LLC. I would like to thank the support from advanced energy materials Nano systems engineer-Dr. Vivekanand Kumar, R&D Scientist-Dr. Siva Kumar and Research Engineer-Dr. Tu Nguyen and other members of the team for their continuous support throughout the thesis work.

I also want to thank all my dissertation committee members Dr. Jacek Jasinski, Dr. Thomas Starr, Dr. Gautam Gupta, and Dr. Farshid Ramezanipour for taking their valuable time in reviewing my work, providing the valuable feedback, and adjusting their schedules for the evaluation of work. Especially, Dr. Jacek Jasinski for spending his valuable time and contribution to some of the discussions reported on this dissertation. Also, I am very thankful to Dr. Joshua Spurgeon and Dr. Bijandra Kumar for allowing me to use their laboratory for my dissertation work.

I would like to express my gratitude for Conn center personnel Dr. Arjun Kumar Thapa (Conn Center), Dr. William Paxton (Conn Center), Ms. Eunice Salazar (Conn Center), Mr. Andrew Marsh (Conn Center), and Dr. Gamini Sumanasekera (Conn Center) for their continued support throughout my dissertation work at University of Louisville.

Moreover, I want to thank all the lab members for their share of knowledge, help, and advice throughout the PhD work

ABSTRACT

MIXED METAL OXIDE NANOWIRES VIA SOLID STATE ALLOYING

Veerendra Atla

July 27, 2021

Mixed metal oxide materials with composition control find applications in energy conversion and storage processes such as heterogenous catalysis, photoelectrochemical catalysis, electrocatalysis, thermal catalysis, and lithium-ion batteries. Mixed metal oxides and/or complex oxides with composition control and in one-dimensional form as nanowires could be interesting to various catalysis applications due to control on single crystal surfaces, active sites, acidity versus basicity site density, and oxygen vacancies. The major challenge is to synthesize mixed metal oxide nanowires beyond binary oxides with composition control. In this dissertation, solid state alloying of binary oxide nanowires with solid and liquid precursors is studied to obtain mixed metal oxide nanowires.

Solid state alloying studies were conducted using either solid precursors of hydroxides or liquid precursor of nitrates mixed with the already synthesized binary metal oxide nanowires, dried and solid state diffused under inert atmosphere to achieve the ternary mixed metal oxides or solid solutions of mixed metal oxide nanowires. First and foremost, porous nanowires of binary oxides have been found to be more beneficial for alloying experiments. Several experiments using different precursors and solutes into commonly available binary oxides such as Zinc Oxide (ZnO), Alumina (Al₂O₃) and Titania

(TiO₂) were conducted to understand the underlying mechanism. Alloying elements included copper, zirconium, cobalt, nickel, and alkali metals. Experiments suggest that the alloying into nanowires were uniform irrespective of the uniformity of contact with precursor. Results also yielded higher solubilities of solutes into nanowires compared to those predicted from solubility in bulk materials. Specifically, the solubility of solute copper obtained is more than 8 at% for titania and alumina nanowire materials. Based on the thermodynamic phase diagram, this solubility is beyond the thermodynamic bulk solubility for these materials at these process conditions. Extended solubility could be potentially attributed to the available higher surface energy at nanoscale, surface free energy minimization, and thermodynamic stabilization. A mechanism is proposed for alloying with nanowires which suggests that the reaction of precursors with metal oxide nanowires is necessary for solute's diffusion and alloying.

The electrocatalytic behavior of porous tin oxide nanowires was investigated using electrochemical reduction of CO₂ to formate. It is concluded that the high-density grain boundary on the nano wire structure is a primary factor in the observed enhancement of the selectivity, rate of HCOOH formation, and associated minimization of the H₂ evolution reaction during the electrochemical reduction of CO₂. Formic acid formation begins at lower overpotential (350 mV) and reaches a steady Faradaic efficiency of ca. 80 % at only -0.8 V vs. RHE.

Nickel alloyed titania nanowires were tested for the effectiveness of single atom catalysis in a dry methane reforming (DMR) application. The activity of nickel alloyed into the titania nanowires displayed superior performance with 96-97% and 83-86% for CO₂ and methane conversion, respectively, with no coke deposition after 50 hours. In

comparison, the nickel supported on titania nanowires exhibited catalyst activity of 98 those predicted from solubility in bulk materials. Specifically, the solubility of solute copper obtained is more than 8 at% for titania and alumina nanowire materials. Based on the thermodynamic phase diagram, this solubility is beyond the thermodynamic bulk solubility for these materials at these process conditions. Extended solubility could be potentially attributed to the available higher surface energy at nanoscale, surface free energy minimization, and thermodynamic stabilization. A mechanism is proposed for alloying with nanowires which suggests that the reaction of precursors with metal oxide nanowires is necessary for solute's diffusion and alloying.

The electrocatalytic behavior of porous tin oxide nanowires was investigated using electrochemical reduction of CO₂ to formate. It is concluded that the high-density grain boundary on the nano wire structure is a primary factor in the observed enhancement of the selectivity, rate of HCOOH formation, and associated minimization of the H₂ evolution reaction during the electrochemical reduction of CO₂. Formic acid formation begins at lower overpotential (350 mV) and reaches a steady Faradaic efficiency of ca. 80 % at only -0.8 V vs. RHE.

Nickel alloyed titania nanowires were tested for the effectiveness of single atom catalysis in a dry methane reforming (DMR) application. The activity of nickel alloyed into the titania nanowires displayed superior performance with 96-97% and 83-86% for CO₂ and methane conversion, respectively, with no coke deposition after 50 hours. In comparison, the nickel supported on titania nanowires exhibited catalyst activity of 98-100% and 55-58% for CO₂ and methane conversion, respectively, for over 50 hours with deposited carbon on the catalyst surface and sintering of nickel particles observed.

In summary, ex-situ alloying of binary oxide nanowires could be used for producing mixed metal oxide nanowires at larger scale. Mixed metal oxide nanowire materials could present model systems for accelerated discovery of new materials and compositions for various catalysis applications.

TABLE OF CONTENTS

ACKNOWLEDGMENTS	iv
ABSTRACT	vi
LIST OF FIGURES	xiii
LIST OF TABLES	xvii
CHAPTER 1 INTRODUCTION	1
1.1 Motivation for the mixed metal oxide nanowires	1
1.2 Synthesis of mixed metal oxide nanowires and limitations of state-of-the-art methods	5
1.3 Proposed method for the synthesis of mixed metal oxide nanowires	9
1.4 Objectives of dissertation	11
1.5 Organization of dissertation	12
CHAPTER 2 BACKGROUND	14
2.1 General remarks and scope of review	14
2.2 Thermodynamics of complex metal oxide systems	14
2.2.1 Hume-Rothery rules for determining the solubility limit in alloys	14
2.2.2 Thermodynamics at the nanoscale for metastable phases	15
.....	16
2.3 Synthesis and application of complex metal oxide materials	18
2.3.1 Solid state reaction method for the synthesis of complex metal oxides	19
2.3.2 Liquid phase methods for synthesis of complex metal oxides.....	25
2.3.2.1 Sol-gel method	25
2.3.2.2 Solvothermal method	25
2.3.2.3 Co-precipitation method.....	26
2.3.3 Gas phase methods for synthesis of complex metal oxides.....	26
2.3.3.1 Flame spray pyrolysis	27
2.3.3.2 Plasma spray pyrolysis.....	27
2.4 Methods for the synthesis of binary metal oxide nanowires	28
2.5 Routes for the synthesis of mixed metal oxide nanowires	32
2.5.1 Synthesis of mixed metal oxide nanowires by in-situ methods	32
2.5.1.1 Hydrothermal synthesis method	33
2.5.1.2 Vapor phase synthesis method.....	34
2.5.1.3 Solution phase synthesis method	35

2.5.1.4	Solid state alloying synthesis method	36
2.5.2	Synthesis of mixed metal oxide nanowires by ex-situ methods	37
2.5.2.1	Solid state diffusion method using the atomic layer deposition (ALD) technique.....	37
2.5.2.2	Metal vapor vacuum arc (MEVVA) ion source doping method.....	38
2.5.2.3	Sol-gel precursor coating method	39
2.6	Applications of mixed metal oxide nanowires in energy conversion processes	43
2.6.1	Heterogenous catalysis	43
2.6.2	Photo electrochemical catalysis	44
2.7	Chapter summary	45
CHAPTER 3 EXPERIMENTAL METHODS AND CHARACTERIZATION TECHNIQUES		47
3.1	Introduction	47
3.2	Atmospheric microwave upstream plasma system.....	47
3.3	Synthesis procedure for porous nanowires (Solvo plasma method)	49
3.4	Synthesis procedure for mixed metal oxide nanowires.....	50
3.5	Materials characterization techniques	51
3.5.1	Scanning electron microscopy analysis	51
3.5.2	TEM (Transmission electron microscopy) analysis.....	52
3.5.3	X-ray diffraction analysis	53
3.5.4	BET surface area analysis.....	53
3.5.5	Thermogravimetry (TGA-DSC) analysis.....	53
3.5.6	Differential scanning calorimetry (DSC) analysis.....	54
3.6	Experimental procedure of the DMR (dry methane reforming) reaction	54
3.7	Electrochemical measurements and electrode preparation	56
CHAPTER 4 SYNTHESIS OF BINARY POROUS METAL OXIDE NANOWIRES		59
4.1	Review of synthesis methods for porous tin oxide nanowires.....	59
4.2	Solvo plasma method for synthesis of porous tin oxide nanowires	61
4.3	Synthesis of porous titania nanowires	65
4.4	Synthesis of porous alumina nanowires.....	69
4.5	Mechanism of pore formation in the nanowires	72
4.6	Chapter summary	75
CHAPTER 5 SYNTHESIS OF MIXED METAL OXIDE NANOWIRES VIA SOLID STATE		
ALLOYING OF SOLUTES WITH BINARY METAL OXIDE NANOWIRES		76
5.1	Synthesis of alloyed nanowires via solid state alloying	76
5.1.1	Synthesis of copper alloyed titania nanowires via solid state alloying	76
5.1.2	Copper alloying into the titania NWs at a shorter reaction time	80
5.1.3	Synthesis of nickel alloyed titania nanowires via solid state alloying method	81
5.1.4	Alloying experiments using various metal oxide nanowires and solutes.....	82
5.1.5	Synthesis of cobalt alloyed zinc oxide nanowires via solid state alloying	84
5.2	Differential scanning calorimetric studies of copper alloying with titania nanowires	85
5.3	Alloying studies with various physical forms of the precursors.....	89

5.3.1	Copper metal precursor coated on titania NWs	89
5.3.2	Copper nitrate precursor coated on the titania nanowires	91
5.3.3	Copper acetate and copper oxide precursor coated on titania NWs.....	92
5.3.4	Alloying studies on the solid-state precursors	94
5.4	Copper alloying with the bulk sized precursor and studies on flame environments to enhance the solubility limits.....	95
5.5	Proposed mechanism of alloying of copper into the titania NWs	97
5.6	Chapter summary	100
CHAPTER 6 MIXED METAL OXIDE NANOWIRES AS DUAL ATOM CATALYSTS IN DRY METHANE REFORMING REACTION		102
6.1	Nickel alloyed titania nanowires synthesis and material analysis.....	103
6.2	DMR test with nickel alloyed/decorated titania nanowires	104
6.3	DMR test spent catalyst material analysis.....	105
6.4	Chapter summary	109
CHAPTER 7 APPLICATION OF POROUS TIN OXIDE NANOWIRES IN ELECTROCHEMICAL CONVERSION OF CO₂		111
7.1	Introduction	111
7.2	Material analysis of the porous tin oxide NWs	113
7.3	Electrochemical testing of tin oxide NWs with cyclic voltammetry.....	114
7.4	Electrocatalyst stability analysis	116
7.5	Chapter summary	119
CHAPTER 8 CONCLUSIONS AND RECOMMENDATIONS FOR FUTURE WORK		120
8.1	Results summary and conclusions	120
8.2	Recommendations for future work.....	126
REFERENCES		128
CURRICULUM VITAE		138

LIST OF FIGURES

Figure 1.1. A) Schematic showing the changes in surface free energy and specific activity per metal atom with metal particle size and the support effects on stabilizing single atoms B) Metal single atoms anchored to (a) metal oxide, (b) metal surfaces, c) graphene (adapted from ²⁵)	4
Figure 1.2. Schematic showing the proposed process of solid-state synthesis method for the mixed metal oxide nanowires with solid/liquid precursors	10
Figure 2.1. Thermodynamic phase diagrams of a) FeO-MgO and b) TiO ₂ -ZrO ₂ systems	15
Figure 2.2. Schematic showing the free energy of mixing of binary components 1, 2 to form 1 mol of solid solution.....	16
Figure 2.3. Data showing the variation in solubility of Mn in zinc oxide based solid solution a) Solubility limit of Mn in ZnO polycrystals with grain sizes above 1000 nm b) Solubility limit of Mn in ZnO polycrystals with grain sizes between 10 and 100 nm. (adapted from ⁵³)	17
Figure 2.4. Phase diagram for CoO and ZnO system in bulk and nano sized materials (adapted from ⁵⁴).....	18
Figure 2.5 Summary of the methods for synthesis of the complex metal oxide materials	19
Figure 2.6. Schematic representation of process of solid-state reaction at the reactants (A, B) interface.....	20
Figure 2.7. Sketch of diffusional process in solids by a) vacancy diffusion b) interstitial diffusion c) interstitialcy diffusion.....	22
Figure 2.8. Schematic of formation process of Al ₂ TiO ₅ in the alumina-titania diffusion couple (adapted from ⁶⁹)	23
Figure 2.9. Sketch of the mechanism of BaSnO ₃ formation from barium carbonate and tin oxide (adapted from ⁷¹)	24
Figure 2.10. Schematic illustration of the proposed mechanism of plasma-processed nitrate-based precursors. The steps are (1) evaporation of precursor solvent (2) amorphous nitrate/nitrite/peroxynitrite phase formation (3) amorphous oxide phase formation (4) nucleation of monometallic oxides (5) alloying of oxides into intermediate compositions (6) growth of alloyed species (7) final non-stoichiometric oxide (adapted from ⁸¹)	28
Figure 2.11. Time scale and quantity of material synthesized for iron oxide nanowires using the different synthesis methods (Adapted from ref. ⁸²).....	29
Figure 2.12. Schematic illustration of mechanism of formation of binary oxide NWs using solvo plasma for high melting point metals and direct oxidation of low melting point metals (Adapted from ref. ⁸³)	31
Figure 2.13. Depiction of mechanism of formation of Na _x TiN _y O _z nanorods using hydrothermal method (Adapted from ref. ⁸⁶).....	34

Figure 2.14. Schematic illustration of mechanism of formation of ternary oxide NWs using direct vapor phase transport (Adapted from Ref. ⁸⁷).....	35
Figure 2.15. Schematic representation of the ex-situ synthesis of nanowires using the ALD method.....	38
Figure 2.16. Schematic illustration of ex-situ synthesis of nanowires using the MEVVA ion source doping method (Adapted from ref. ⁴⁵).....	39
Figure 2.17. Schematic of the ex-situ synthesis of nanowires using the sol-gel precursor doping method (Adapted from ref. ⁴⁴)	39
49	
Figure 3.1. Sketch of the atmospheric microwave upstream plasma reactor system used for binary metal oxide nanowire synthesis	49
Figure 3.2. Schematic representation of synthesis of mixed metal oxide nanowires with the vacuum furnace	50
Figure 3.3. Schematic of transition of events during the heating of a sample.	54
Figure 3.4. Schematic of packed bed reactor and GC system used for the testing of dry methane reforming catalyst.....	56
Figure 4.1. SEM image analysis, TEM image analysis, X-ray diffraction analysis of as synthesized and porous tin oxide nanowires.....	63
Figure 4.2. a) TEM image analysis of porous tin oxide NWs b) Brunauer–Emmett–Teller (BET) analysis of tin oxide nanowires before and after the acid wash treatment. ...	64
66	
Figure 4.3. a) Scanning electron microscopy image analysis of porous titania NWs b) Hi resolution TEM image analysis of porous titania NWs, and c) BET surface area analysis of porous titania NWs	66
Figure 4.5. Experimental data of a) Calcined porous titania NWs X-ray diffraction analysis at different temperatures (1) at 450 deg C for 2 h (2) 600 deg C for 2h (3) 800 deg C for 6 h b) SEM image analysis of calcined porous titania nanowires at 800 deg C for 6 h.....	68
Figure 4.6. X-ray diffraction analysis of alumina NWs (1) After the calcination at 650 deg C (2) Before the calcination.....	71
Figure 4.7. Electron microscopy images of porous alumina nanowires: (a) SEM image analysis and (b) & (c) Brightfield TEM image analysis.	71
Figure 4.8. Schematic representation of the pore formation mechanism in the titania nanowires	72
Figure 5.1. SEM image analysis of cu (8 at%) alloyed titania nanowires a) before alloying b) after alloying; c) X-ray diffraction analysis of alloying from 0 at% to 15% of Cu into the titania NWs; d) Peak shift analysis of copper alloyed titania NWs; e) Raman analysis of copper alloyed titania NWs; and f) Raman peak shift analysis of copper alloyed titania NWs.....	78
Figure 5.2. TEM image analysis of copper alloyed titania NWs: a) before alloying and b) after alloying. TEM EDX line profile analysis of copper alloyed titania NWs along the diameter of NWs c) before alloying, and d) after alloying	79
Figure 5.3. TEM EDX elemental analysis of copper (8 at%) alloyed titania NWs in a vacuum furnace.....	80
Figure 5.4. Nickel alloying into the titania NWs a) SEM image analysis of nickel alloyed titania NWs; b) TEM EDX elemental analysis of nickel alloyed titania NWs; and c)	

X-ray diffraction analysis of nickel alloyed titania NWs and titania NWs d) Peak shift analysis of nickel alloyed titania NWs.....	81
Figure 5.5. TEM EDX elemental analysis of a) copper alloyed alumina NWs (up to 20%) b) Zirconia alloyed titania NWs up to 8% c) X-ray diffraction analysis of copper alloyed alumina NWs d) UV-Vis analysis of copper alloyed titania NWs.....	82
Figure 5.7. DSC analysis of copper alloyed titania NWs a) with different heating rates; b) with in different atmospheres; c) copper nitrate loaded (12 at%) TiO ₂ NWs and TiO ₂ bulk powder; and d) on copper nitrate precursor	86
Figure 5.8. a) Gibbs free energy calculated as a function of increase in temperature b) Inset of 5.8 (a).....	87
Figure 5.9. X-ray diffraction analysis of copper alloying in titania NWs at a temperature lower than the decomposition temperature (at around 190 deg C).....	88
Figure 5.10. Kissinger plot obtained from the data using the DSC experimental technique to determine the kinetic parameters of the reaction	88
Figure 5.11. Thermal evaporation of cu metal layer on the titania NWs a) Metal copper 20nm layer as coated; b) after the In-situ heating in the TEM at 500 deg C for 1h; and c) vacuum annealing of copper metal coated on titania NWs at 500deg C	90
Figure 5.12. TEM image analysis at different resolutions of a) as synthesized titania porous nanowires; b) copper nitrate precursor coated porous titania nanowires with discreet nanoclusters of copper nitrate; and c) copper alloyed titania nanowires after solid state alloying under inert atmosphere.....	91
Figure 5.13. a) &b) X-ray diffraction analysis of copper acetate precursor alloyed with titania NWs; and c) DSC analysis of titania nanowires coated with the copper acetate precursor.	93
Figure 5.14. a) &b) TEM EDX elemental analysis of copper oxide alloyed with the titania NWs; and c) DSC analysis of the copper oxide precursor coated titania NWs	93
Figure 5.15. SEM image analysis and X-ray diffraction analysis of the lithium aluminate, sodium aluminate and nanowires.....	94
Figure 5.16. a) TEM EDX elemental analysis; b) X-ray diffraction analysis of the copper alloyed titania NWs and bulk titania; and c) Exposure of copper nitrate coated titania NWs under different flame environments.....	96
Figure 5.17. Structural model depiction of mechanism of copper alloying process into the titania NWs using the VESTA software A) Schematic of alloying process on the nanowires B) Atomic model visualization of copper alloying process in the titania NWs.	97
104	
Figure 6.1. Nickel alloyed titania sample (8 wt%) a) SEM image analysis of fresh catalyst sample c) TEM EDX analysis of nickel alloyed titania sample c) XRD analysis of fresh catalyst sample d) Peak shift analysis of nickel alloyed titania sample.....	104
Figure 6.2. Nickel alloyed/decorated titania NWs sample DMR test performance a) nickel alloyed sample b) Ni metal decorated on titania NWs, Methane and CO ₂ conversion at different temperatures (at 750-850 deg C, GHSV of 60000mlgr ⁻¹ h ⁻¹ , feed ratio of methane to carbon dioxide of 1).	105

Figure 6.3. DMR reaction spent catalyst samples nickel alloyed and decorated titania NWs TGA analysis a) spent catalyst sample of nickel alloyed titania NWs b) spent catalyst sample of nickel decorated on titania NWs	106
Figure 6.4. Nickel decorated titania NWs a) X-ray diffraction analysis of fresh catalyst sample and spent catalyst sample of the dry methane reforming reaction c) TEM EDX analysis of fresh catalyst sample d) TEM EDX analysis of spent catalyst sample of the DMR testing.....	107
Figure 6.5. Nickel alloyed titania NWs spent catalyst sample of DMR reaction a) SEM image analysis b) &d) TEM image and EDX analysis of spent sample showing the distribution of nickel and titania c) X-ray diffraction analysis of spent sample in comparison with fresh sample e) Molecular level depiction of proposed DMR reaction mechanism on Ni alloyed titania NWs	109
Figure 7.1. Experimental data of a)&b) SEM image analysis c)&d) TEM image analysis and, e) X-ray diffraction analysis of as synthesized and porous tin oxide nanowires	113
Figure 7.2. CO ₂ electrochemical reduction performance data (a) J-E curves obtained in CO ₂ -saturated 0.1 M KHCO ₃ solution for reduced Sn-NWs, Sn-NPs, Sn-pNWs, and bare GDL (substrate). Faradaic efficiency vs. potential collected over 2 h at each potential for (b) all carbon products, (c) HCOOH, and (d) CO. (Hydrogen was the only other species detected during the experiments)	115
Figure 7.3. Catalyst stability: Current density (black line) and product faradaic efficiency (F.E.) vs. time for (a) a bare porous carbon GDL substrate; (b) Sn-pNWs; (c) Sn-NPs; and (d) Sn-NWs. In each case, the potential was maintained at -0.8 V vs. RHE. ..	117
Figure 7.4. Comparison of the catalyst activity for formic acid formation (a) Measured BET surface area per catalyst mass and partial current density of formic acid production, J _{HCOOH} , of Sn-NW, Sn-NP, and Sn-pNW catalysts. Partial current density was calculated at -0.8 V vs. RHE. (b) Overview of various reported catalysts performance for HCOOH production from electrochemical CO ₂ reduction in aqueous electrolyte. Here the letters represent: Sn-pNWs, Sn-NWs and Sn-NPs (this study), A – Sn plate, ¹⁵² B - SnO _x /carbon black, ¹³⁹ C - Sn dendrite (heated), ¹⁴⁶ D - SnO _x /graphene, ¹³⁹ E - Sn metal electrode, ¹⁴³ F - Sn foil, ¹⁵³ G - Cu ₅₇ Sn ₄₃ , ¹⁵⁴ H - Sn dendrite (heated), ¹⁴⁶ I - Sn dendrite, ¹⁴⁶ J - Sn ₆ O ₄ (OH) ₄ , ¹³⁸ and K - Sn/SnO _x /Ti ¹⁴⁰	118

LIST OF TABLES

Table 2.1. Selected mixed metal oxide nanowires synthesis routes	-----40
Table 4.1 Review on the porous tin oxide nanowires synthesis methods	-----60
Table 4.2 Free volume calculations and mesoporous phase transformation temperature for different nanowire systems.	-----74
Table 5.1 Values of kinetic parameters evaluated from the DSC data-	-----89
Table 6.1 Comparison of DMR catalyst performance	-----105

CHAPTER 1 INTRODUCTION

1.1 Motivation for the mixed metal oxide nanowires

Chemical and materials sciences have mostly focused on unveiling the scientific aspects of structure-function relationships with the aim of achieving the targeted property or processes by modifying the material atomic arrangement. A U.S. Department of Energy report states that “Chemical and materials sciences have traditionally focused on understanding structure– function relationships with the goal of predicting *where the atoms should be placed* to achieve a targeted property or process. Much less effort has been directed toward a predictive science of synthesis— understanding *how to get the atoms where they need to go* to achieve the desired structure”¹. Advancement in predicting materials by design is needed to make progress in this field. One of the ways to achieve this is by controlling composition in materials and designing the interfaces at nanoscale. Mixed metal oxide or complex oxide materials with composition control would allow for tuning various properties such as acid-base redox properties, electronic conductivity, ionic conductivity that arise from charge imbalance, vacancies, defects, and other synergistic activity of the complex structure.

Mixed metal oxide materials have applications in heterogenous catalysis, electrochemical energy storage, energy harvesting (solar cells), superconductors, thermoelectric, purifications and separations, and gas storage^{2,3}. Few examples include the following: super conducting oxides such as Sr_2RuO_4 ⁴, photo electrochemical conversion

using the complex metal oxides BiVO_4 ⁵, SrTiO_3 ⁶, electrochemical energy storage with lithium nickel manganese cobalt oxide and lithium titanate materials^{7, 8}, in heterogenous catalysis $\text{LaFe}_{1-x}\text{Co}_x\text{O}_3$ mixed-oxide for combined methane reforming, Ni/Mg–Al mixed metal oxide catalyst for steam reforming of ethanol, and $\text{Fe}_x\text{Ce}_{1-x}\text{O}_2$ mixed metal oxides for N_2O decomposition³. The composition control in mixed metal oxides combined with morphology control in nano dimensions would offer new opportunities to discover new materials for advancing various energy conversion and storage technologies.

In particular, nanowires a new class of materials with one of the dimensions ranging from 1-100nm have received special attention due to their interesting physical and chemical properties over their bulk counterparts⁹. Much of the research on nanowires dates back into 1964, in BELL LABORATORIES to the discovery of nano whiskers by using vapor-solid-liquid method ¹⁰. Since then, there has been significant development of nanowires for various fields of science and technology. Nanowires have been synthesized and assembled with specific geometries, hetero junctions, and architectures with the applications in electronic, photonic, biomedical, energy conversion and storage applications¹¹⁻¹⁵. Nanowires are extensively used in the thermo electrics for the low thermal conductivity arising from strong boundary phonon scattering. Also, nanowires find applications in solar to fuel conversion because of their high surface area, tunable bandgap, and efficient charge transport and collection. Nanowires also find application in energy storage batteries since they could maintain electron transport along the long axis and have confinement effects across the diameter. Nanowires are a particularly promising bio interfaces, given (1) their unique optical and electronic properties and (2) their high degree of synthetic control and versatility¹⁶.

However, it is important to design/modify physical, chemical, thermal, and catalytic properties of the nanowires for improving their efficient use¹⁷⁻¹⁹. One dimensional nanostructure with control of composition would play key role in control of surface reactivity, selectivity, and efficiency for catalysis applications, electron, or hole transfer barriers at the interfaces in energy harvesting, electrical conductivity, and thermal conductivity control in thermo electrics, control of surface area, network connectivity, crystal structure, redox activity, and electrical conductivity in energy storage applications. Particularly, compositional tunability of the mixed metal oxide nanowires is used for introducing the oxygen vacancies, structural defects, to change the binding energy of the active sites and tuning acid-base sites on the exposed active facets along with the unique structural characteristics of the nanowires²⁰⁻²².

Mixed metal oxide nanowires with highly dispersed metals at atomic scale could provide the synergistic interactions that are not possible with traditional metal supported nanowires. Traditionally, industrial catalysts were prepared by dispersing metal particles on high surface area support for the efficient use of the active sites. Most of these supported catalyst materials undergoes sintering at high temperatures by particle migration/coalescence or by Ostwald's ripening. Catalyst activity deteriorates as the reaction progresses²³. Mixed metal oxides nanowires, on the contrary, offer atomic level dispersion along with single crystal faceted surfaces, large surface area, and a uniform surface offering active site management for higher selectivity and conversion. Furthermore, metastable mixed metal oxides are yield enhanced kinetics relative to the stable mixed metal oxides. For example, for the reduction of nitrobenzene on $\text{La}_{0.8}\text{Sr}_{0.2}\text{FeO}_3$ activation energy is 73.9 kJ/mol compared to the stable oxides LaFeO_3 (88.9 kJ/mol), SrFeO_3 (84.4 kJ/mol)

activation energies²⁴. Lower activation energy means the better catalytic activity. Figure 1.1 shows the surface energy increase with the reduction in size. Quantum confinement led to changes in physical and chemical properties, also the size reduction increases the unsaturated coordination environment of the metal species. Hence, the surface energy reaches the maximum and is highly reactive to the adsorbates and chemical species.

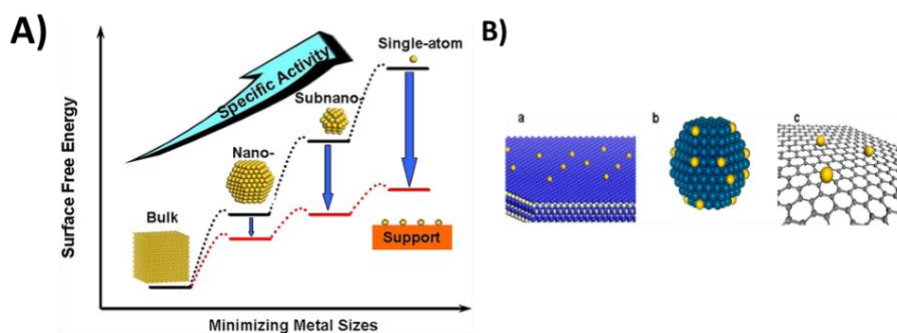


Figure 1.1. A) Schematic showing the changes in surface free energy and specific activity per metal atom with metal particle size and the support effects on stabilizing single atoms B) Metal single atoms anchored to (a) metal oxide, (b) metal surfaces, c) graphene (adapted from ²⁵)

Mixed metal oxide nanowires (more than one metal ion) would be a good supporting material to anchor the highly dispersive atoms. The surface of the nanowires can be functionalized with active metals by annealing or functionalizing with different chemical moieties to tune acid/base properties of the catalyst. Using single crystal nanowires as model systems, one can design high performance catalysts and define both activity and selectivity through designing uniform density of active sites and surfaces with composition. Furthermore, metal oxide nanowires when used in industrially relevant formats such as extrudates and coatings on high surface area supports can still exhibit high density of single crystal surfaces and high density of active sites for improved selectivity and activity with a particular chemical reaction.

Mixed metal oxide nanowires selectively used in electro chemical and heterogenous catalysis reactions such as high catalytic performance for CO oxidation to CO₂ was achieved in ceria nanowires by alloying with the foreign metal (lanthanides) on a selective facet. Higher activity is attributed to the formation of high-density oxygen vacancies and enhanced the mobility of oxygen from bulk to the surface of the active facets of the alloyed ceria NWs ²⁶. For bimetallic CuSn nanowires (NWs) used for electrochemical CO₂ reduction reaction with a higher formate selectivity of 90.2% at -1.0 V vs RHE. Superior performance is ascribed to the Sn atoms doping on CuO (111) facet as well as the selective adsorption of intermediates on the nanowire support to suppress the hydrogen evolution reaction ²⁷. Ti-doping hematite nanorods exhibited excellent repeatability and durability. It was found that the Ti alloying in hematite nanowires promoted the band bending, increased the carrier density, and improved surface state. Eighty percent of the fabricated photoanodes reproduced the steady photocurrent density of 1.9–2.2 mA/cm² at 1.23 V vs RHE at least 3 h in a strong alkaline electrolyte solution²⁸. The catalytic oxidative coupling of methane (OCM) on transition metal doped titania nanowire catalysts was performed and they found that alloyed nanowires seemed to improve the catalytic activity and selectivity for OCM reaction to convert methane to C₂ products. The electric and optical properties of nanowires were tuned to attain the higher catalyst performance²¹.

1.2 Synthesis of mixed metal oxide nanowires and limitations of state-of-the-art methods

Currently, research scale binary metal oxide nanowires are synthesized by using bottom up approaches such as vapor phase synthesis²⁹, solution phase synthesis³⁰, metal catalyst assisted laser ablation technique, and template-based methods^{19, 31}. Top-to-bottom approaches for binary metal oxides include metal assisted chemical etching and electron

beam lithography⁹. The bottom-up approaches binary metal oxides use vapor-solid-solid (VSS) and vapor-liquid-solid (VLS) methods with a foreign metal as catalyst to control one-dimensional growth³²⁻³⁴. Many of the above-mentioned techniques are not scalable beyond gram scale. In the last few years, there has been a significant progress with scale-up of production of binary metal oxide nanowire materials such as TiO₂, SnO₂, ZnO, WO₃, Al₂O₃, MoO₃, MnO₂, Fe₂O₃ systems using the dry manufacturing of nanowires^{35,36}. Binary metal oxide nanowires using the low melting point metals are synthesized by thermal oxidation of the corresponding metal precursors. Metal powders are exposed with highly excited plasma or hydrocarbon flame in a fluidized bed. For high melting point temperature metals, metal powders are mixed with salts and then exposed to plasma flames termed as solvo-plasma method³⁶.

The scalable synthesis methods of binary metal oxide nanowires may not be used to synthesize mixed metal oxide nanowires. Direct oxidation of mixed metal precursors produces a segregated mixture of binary metal oxide NWs (nanowires). This is because of the difference in melting points of the metals and their varied affinity towards the oxygen. Individual binary oxides grow out as separate oxide phases from molten melt. On the other hand, solvo plasma method needs to form a molten alloy of alkali with the respective metal precursors. The metals with tendency to form molten alloy with the alkali will grow faster than the other leading to the separate oxide nanowire phases. Both above methods are unsuitable for synthesis of mixed metal oxide nanowires.

There are few studies on synthesis of stable phase compositions of certain mixed metal oxides using template-based methods for ZnFe₂O₄, NiCo₂O₄ and ZnCo₂O₄³⁷⁻³⁹. There have been attempts at making mixed metal oxides using both in-situ and ex-situ synthesis

method. In the case of in-situ techniques, the solute or alloying species are introduced during the synthesis of mixed metal oxide nanowires. In the case of ex-situ techniques, solute or alloying species are alloyed with the already synthesized nanowires. In-situ synthesis of mixed metal oxide nanowires were reported in literature by using template directed synthesis^{37, 38}, vapor phase^{40, 41}, solution-based^{42, 43}, hydrothermal²⁶ and ex-situ methods^{20, 28, 44, 45}. However, in-situ synthesis methods exhibit limited success with range of composition control. Vapor phase methods are based on nucleation of alloy species with the metal catalyst and the supersaturation of species in the molten mixture lead to the formation of nanowires. However, uniformity, scalability, use of metal catalyst, substrate choice at higher temperatures and most importantly achieving the higher solubility were hindrances to this method. In solution-based in-situ synthesis, sol-gel method is based on the nucleation of precursors followed by hydrolysis and condensation of ions to form oxide NWs. In molten salt-based solution methods, the higher amount of salt concentrations assist in achieving the eutectic temperature and higher mobility of ions in the presence of salt. In these techniques, the reaction conditions such as P^H , viscosity and solvation of metal ions seem to impact the production of mixed metal oxide nanowires with composition control. Hydrothermal methods were based on metal ion complex formation followed by supersaturation lead to the growth of nanowires, alloyed metal ions coprecipitate with hydroxide ions. It is also possible that the alloying elements may possibly be incorporated after nanowires of stable phase compounds formed like the ex-situ procedure. It has been observed that structural changes, no control over the phase or morphology, smaller quantities, high pressures, and longer reaction times (at least 12-24 h) are the impedances to this method. In the wet chemical techniques such as hydrothermal and solvo-thermal,

the underlying mechanisms responsible for one-dimensional growth are also not well understood.

Ex-situ alloying of the already synthesized nanowires is a viable option for scalability and enables independent control over the amount of solute to be alloyed. Earlier studies on ex-situ solid state diffusion of precursors into the nanowire has been studied for TiO₂ nanowires alloyed with MnO_x and ZrO_x, iron oxide nws alloyed with TiO_x solute phases^{20, 28}. These studies used an atomic layer deposition (ALD) technique to deposit solute phase uniformly on the surface and allowed solid-state diffusion into the nanowires. However, the process of ALD is not an easy technique for scaling up for nanowire powders. Also, ex-situ sol-flame synthesis of TiO₂ nanowires with W and C co doping, a sol-gel liquid dip was used to coat the precursor material on already synthesized nanowires. Dip coating lacks control over the coating of the precursor material. Though the flame process accelerates the diffusional process, this method uses sol-gel precursor as solute that was prepared by multistep process and the pristine nanowires are also made by non-scalable hydrothermal method. The results show the surface to bulk concentration gradient along the diameter of the nanowires. Also, high energy based molecular beam epitaxy and metal vapor vacuum arc (MEVVA) has been used in the synthesis. These methods have disadvantage of using high energy beams or electrons that destroys the NWs structures and non-uniformity in alloying.

Mixed metal oxide nanowires synthesized by current state of the art ex-situ and in-situ synthesis techniques lack uniformity in alloying and are difficult to achieve the controlled composition in alloying. Lack of understanding on the solid-state alloying of nanowires with other solid/liquid precursors makes it difficult to scale up and expand the

techniques for other complex oxide systems. Solid state reaction in the bulk materials is a common synthesis method to obtain the thermodynamically stable/meta stable products from reactants treated at high reaction temperature for longer times. Solid state reactions are intrinsically slow because of inhomogeneous mixing at the atomic level, so liquid or gas phase transport needed to get homogenous mixing of reactants. Usually, several hours to days are required to undergo complete reaction⁴⁶. Factors that affect the solid-state reaction are chemical and morphological properties of the reagents including the surface area and free energy with the solid-state reaction. Also, it depends on the temperature, pressure and the environment of the reaction⁴⁷. These limitations/factors that hinder the solid-state alloying in bulk materials could be solved by using the highly porous nanomaterials as solvent phase and liquid precursors as a solute phase to achieve the uniform and controllable alloying in nanowire morphology. The limitations of size, homogenous mixing and surface energy states are very favorable in high surface area nano structures to obtain the desired solid state diffusion reactions.

1.3 Proposed method for the synthesis of mixed metal oxide nanowires

Here, this dissertation work focuses on studying an ex-situ alloying concept using liquid and solid precursors for alloying elements with porous nanowire and nanostructured materials. Solid state diffusion in nanostructures is highly favorable due to the nanoscale species, increased defects, higher surface areas and higher exposed surfaces. A simple scalable method shown in Figure 1.2 is proposed for producing mixed metal oxide nanowires by overcoming the challenges with the synthesis of mixed metal oxide nanowires. This concept uses solid state diffusion of solute species into the solvent phase of the nanostructured materials. Ex-situ modification of already synthesized nanowire

material by mixing with liquid or solid precursors, followed by drying and solid-state diffusing into the nanowires under the inert/vacuum atmosphere. The solute species forms a uniform ultrathin discrete nanosized layers on the surface of pristine nanowires and the solute atoms are solid state diffused into the pristine nanowire under inert environment that produces the mixed metal oxide nanowires.

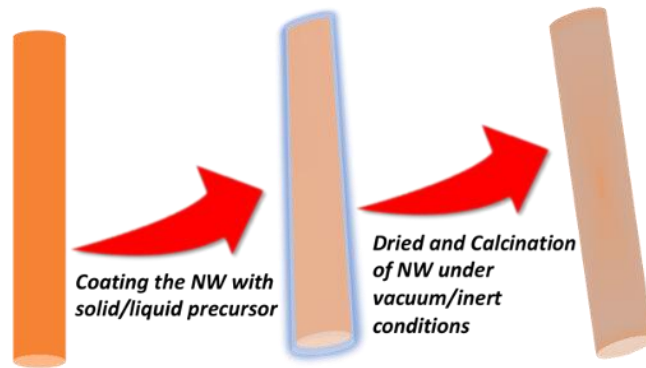


Figure 1.2. Schematic showing the proposed process of solid-state synthesis method for the mixed metal oxide nanowires with solid/liquid precursors

There are many unresolved questions about solid state alloying with nanowire systems prior to rationalizing the proposed approach for making mixed metal oxide or even complex oxide nanowires from binary or stable compound nanowires.

1. Mechanism of alloying – the reaction between the metal oxide nanowires and the precursor and the diffusion of the alloying element. Whether uniformity of alloying inside a nanowire controlled by the uniformity of coating over nanowire with precursor
2. Is the alloying composition control is governed by bulk equilibrium solubility limits for nanowires?

1.4 Objectives of dissertation

The overall goal of this dissertation is to develop a method for producing mixed metal oxide nanowires from binary metal oxide nanowires. Understanding the formation mechanism of the porous binary metal oxide nanowires and mixed metal oxide nanowires. Applicability of proposed mixed metal oxide nanowire synthesis method for the other systems of mixed metal oxide nanowire and the applications of synthesized mixed metal oxide nanowire materials in heterogenous catalysis and electrochemical catalysis reactions.

The specific objectives of the dissertation are the following:

- Investigate the production of porous nanowires using solvo plasma techniqueTM and other wet chemical techniques. Control of the process parameters for the binary metal oxide nanowires such as temperature and acid concentration on the porosity changes in the binary metal oxide nanowires.
- Understanding the mechanism of pore formation in various nanowire systems and its's applicability to the other nanowire systems
- Investigate ex-situ alloying of porous and solid binary oxide nanowires using various alloying elements. Specifically, study alloying into common binary oxide nanowires such as titania, alumina and zinc oxide using both solid and liquid precursors. Understand the mechanisms involved.
- Understand the solubility and uniformity of alloying in nanowires.

Study the performance of porous nanowires and alloyed nanowires with catalysis applications. In the case of thermal heterogeneous catalysis applications, study the effectiveness of single atom catalysis with nickel alloyed titania nanowires in terms of

preventing coke formation in reforming applications at high temperatures. Propose a mechanism for the dry methane reforming reaction on the nickel alloyed titania nanowires.

This thesis research is focused on understanding and rationalizing ex-situ alloying of nanowires with various solute and alloying elements to create mixed metal oxide nanowires. The dissertation explores the possibility of generalizing the method for various metal oxides. The development of this method allows wide range of opportunities to synthesize various mixed metal oxide nanowire systems that potentially could be used in various applications of energy conversion and storage processes.

1.5 Organization of dissertation

This dissertation is divided into eight chapters.

Chapter 1 introduces the importance and potential applications of nanowires. The challenges and limitations of current methods for the synthesis of mixed metal oxide nanowires.

Chapter 2 includes the background of state-of-the-art methods for the complex oxide materials, binary metal oxide nanowires and the limitations of state-of-the-art methods used for binary metal oxide to synthesize the mixed metal oxide nanowires. The current methods in literature used for the synthesis of mixed metal oxide nanowires and their disadvantages. The growth-related mechanisms of mixed nanowires have been discussed. Also, the role of Gibbs free energy of mixing at nanoscale and identifying the favorable solubility limits with the Hume Rothery theory is presented.

In chapter 3 the synthesis of materials and methods here studied are discussed. The methodology and characterization techniques used for the current work are explained. Vacuum furnace and other equipment used for the solid-state diffusion is discussed here.

Also, the testing equipment used for both the electrochemical CO₂ conversion and packed bed reactor used in the DMR (Dry methane reforming reaction) is discussed here.

Chapter 4 focusses on the development of methods for the synthesis of porous binary metal oxide nanowires such as titania, tin oxide, and alumina NWs and the study of parameters effecting the porosity in the nanowires. A proposed mechanism for the pore formation is discussed.

Chapter 5 presents the synthesis of mixed oxide nanowires using the solid-state diffusion, their characterization to identify important structural parameters, generalizing the method for the other nanowire systems and possibility of alloying with other metals. The systems of copper alloyed titania NWs, copper alloyed alumina NWs, cobalt alloyed zinc oxide NWs, and zirconia alloyed titania NWs are studied. The process parameters such as temperature, pressure, and role of thermodynamics in alloying process is discussed. The solubility limit of bulk size solvent phase material and gas environment effect on alloying is studied. A mechanism is proposed for the alloying process.

Chapter 6 Mixed metal oxide nanowires application in the DMR (Dry Methane reforming reaction) to compare the role of alloyed catalyst with the metal supported on nanowires catalyst. A reaction mechanism is proposed for the formation of products.

Chapter 7 focusses on potential applications of porous tin oxide nanowires for electrochemical conversion of carbon dioxide to formic acid

Chapter 8 Summarizes the main conclusions and future recommendations that could be done to expand this work.

CHAPTER 2 BACKGROUND

2.1 General remarks and scope of review

This chapter provides a review of the conventional and state-of-the-art methods used for the synthesis of complex oxides, binary metal oxide nanowires and mixed metal oxide nanowires. The details about the current scalable methods for the synthesis of binary metal oxide nanowires are also discussed. In terms of mixed metal oxide nanowires, various challenges with state-of-the-art methods and strategies are detailed. The concept of solid-state alloying and the role of thermodynamics in solubility limit in nanoscale materials is explained. Finally, the uses for mixed metal oxide nanowires in energy conversion applications are reviewed.

2.2 Thermodynamics of complex metal oxide systems

2.2.1 Hume-Rothery rules for determining the solubility limit in alloys

To synthesize the mixed metal oxide materials, important parameters that govern the solid-state solubility of solute into the solvent materials needs to be investigated. Hume Rothery proposed a set of sufficient rules for the metal solute atoms to dissolve into other metal solvent to form a completely miscible solid solution at any composition. This could be applied for any complex oxide material systems. The rules are that the atomic radius of the solute is within 15% of solvent atomic size, should have the same crystal structure, and lower electronegativity difference. Higher electro negativity difference favors the formation of compounds. An example of completely soluble system of magnesium oxide in iron oxide and a limited soluble system of zirconia in titania were shown in Figure 2.1.

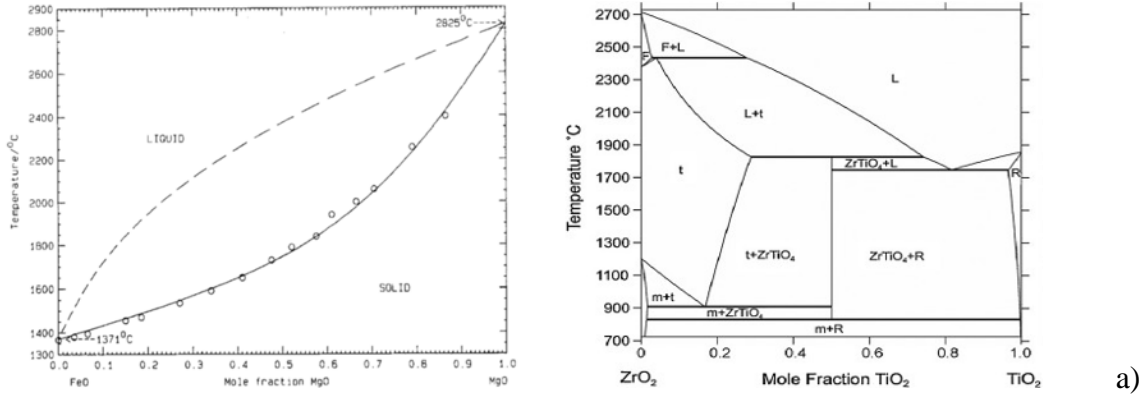


Figure 2.1. Thermodynamic phase diagrams of a) FeO-MgO and b) TiO₂-ZrO₂ systems
 Figure 2.1a shows that iron oxide and magnesium oxide are completely soluble systems at any given composition. Whereas the solubility of zirconium in titania is limited and it is about 5 at% at 1700 deg C from solidus curve of titania. As shown in Figure 2.1b, the solubility of titania in zirconia is less than 1 at% even at a temperature of 1100 deg C.

2.2.2 Thermodynamics at the nanoscale for metastable phases

Materials systems with sizes that range from 1 to 100 nm are in the intermediate state between the bulk level and molecular level. The physical properties such as electronic, magnetic, optical, chemical, and thermal properties are significantly different from the corresponding bulk materials⁴⁸. These systems are characterized by the fact that high surface to volume ratio of atoms available. This could cause the changes in the physical properties such as the melting point depression and other phase transitions of nanoparticles^{49, 50}. One way to study the thermal effect in nano size material is by introducing the surface effects in the classical thermodynamics.

Gibbs free energy is an important parameter for evaluation of the thermodynamic properties. Whenever there is a creation of additional surface or interface, it would provide an additional free energy to the system. This could be written as equation (2.1), where ΔG is the excess free energy, γ free surface energy per unit area and A is the surface area.

$$\Delta G = \gamma A \text{ ----}(2.1)$$

The Gibbs free energy of binary solution of two pure elements is obtained as follows. As shown in Figure 2.2, it is assumed that the components 1, 2 have the same crystal structures in their pure states and could be mixed in any compositions to a make solid solution. Here, G_1, G_2 are the Gibbs free energy of components 1,2 and X_1, X_2 are the mole fractions of components 1,2. The binary mixture total free Gibbs free energy before the mixing is

$$G_A = G_1 X_1 + G_2 X_2 \text{ ----}(2.2)$$

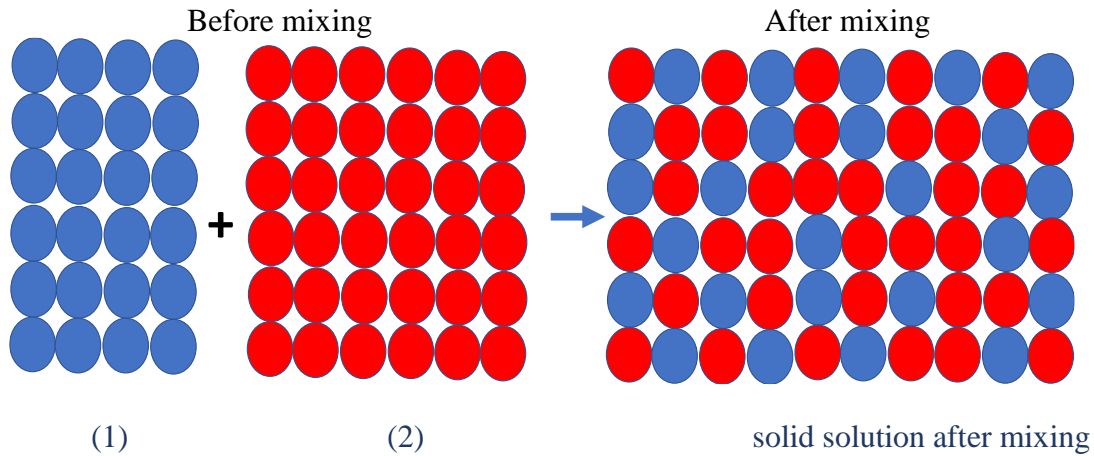


Figure 2.2. Schematic showing the free energy of mixing of binary components 1, 2 to form 1 mol of solid solution

Gibbs free energy of binary mixture after the mixing is,

$$G_B = G_A + \Delta G_{MIX} \text{ ----}(2.3)$$

Here, ΔG_{MIX} is the change in Gibbs free energy caused by mixing the binary components.

By substituting the equation for ΔG_{MIX} obtained from reference ⁵¹, Gibbs free energy after the mixing is given as

$$G_B = G_A + RT (X_1 \ln X_1 + X_2 \ln X_2) \text{ ----}(2.4)$$

So, the final equation for mixing binary components becomes

$$G_B = G_1 X_1 + G_2 X_2 + RT (X_1 \ln X_1 + X_2 \ln X_2) \text{ ----(2.5)}$$

For the nanostructures surface energy terms are added to the Gibbs free energy of bulk material. It is given by

$$G_B = G_1 X_1 + G_2 X_2 + RT (X_1 \ln X_1 + X_2 \ln X_2) + \gamma A \text{ ----(2.6)}$$

Also, the phase diagrams for the nanograined materials could drastically differ from those for the single crystals or coarse-grained poly crystal materials. Mclean et al., was probably first to notice the that the apparent solubility limit (C_{sa}) in the fine grained materials was higher than the volume solubility C_s ⁵². Also, Straumal et al., showed the increase in solubility of Mn in the zinc oxide materials with the decrease in the grain size of ZnO. They noticed higher solubility of Mn into the zinc oxide nanowires upto 30% Mn. The peaks of the secondary phase (Mn_3O_4 with cubic lattice) become visible in the X-ray diffraction spectra at 30 at% Mn. At the similar conditions, the secondary phase of manganese oxide appeared in the bulk ZnO at only 12 at% of Mn⁵³. From Figure 2.3, it is confirmed that the nanograined size promotes the higher solubility at lower temperature compared to the bulk sized material.

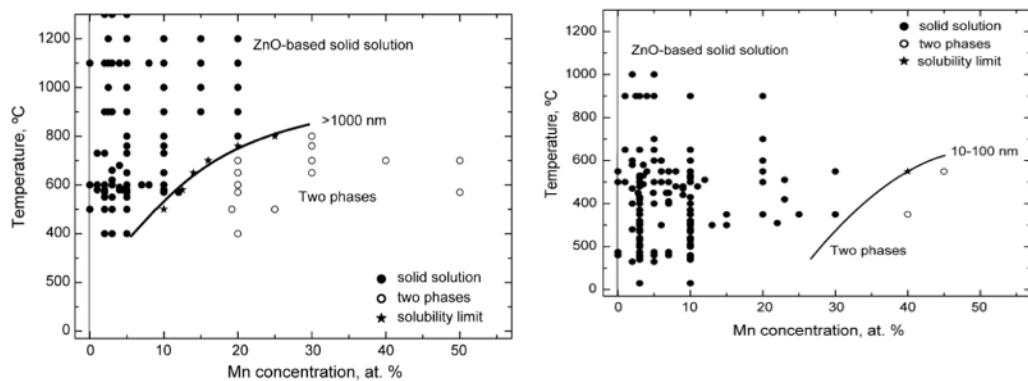


Figure 2.3. Data showing the variation in solubility of Mn in zinc oxide based solid solution
a) Solubility limit of Mn in ZnO polycrystals with grain sizes above 1000 nm
b) Solubility limit of Mn in ZnO polycrystals with grain sizes between 10 and 100 nm.
(adapted from⁵³)

Also, Ma et al., studied the bulk and nano solubility of cobalt oxide in ZnO nano particles and has shown an extended solubility of cobalt oxide in ZnO at nanoscale. As shown in Figure 2.4, at 600 K temperature, the solubility of CoO observed at 20 at% in zinc oxide for nanoscale in comparison to the bulk zinc oxide materials with the cobalt oxide solubility at 3 at%. The extended higher solubility of cobalt oxide in nano sized zinc oxide material could be related to the higher surface energy available at the surface of nanoscale zinc oxide⁵⁴.

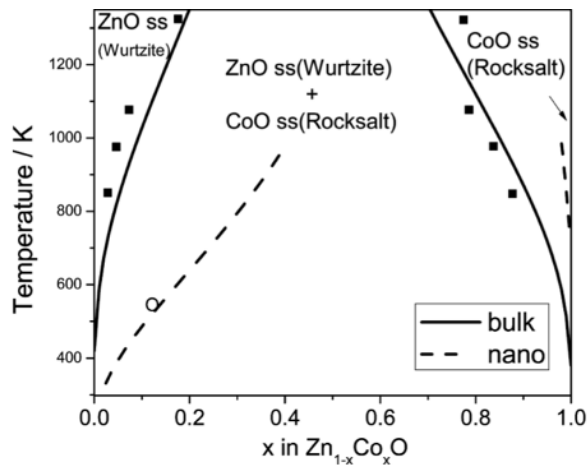


Figure 2.4. Phase diagram for CoO and ZnO system in bulk and nano sized materials (adapted from⁵⁴)

2.3 Synthesis and application of complex metal oxide materials

Complex oxides are promising for a wide variety of novel applications in thermoelectrics⁵⁵, photo-electrochemistry⁵⁶, energy conversion and storage², heterogenous catalysts⁵⁷, and nanoelectronics⁵⁸. The modification of composition and structure in complex oxides can impact their physical, magnetic, optical, and chemical properties⁵⁹.

As shown in the Figure 2.5, the synthesis techniques for complex oxides can be categorized into solid, vapor and gas phase based on the nature of reactants used. The solid-state techniques use solid state reaction for alloying different compounds to make

complex oxides. The liquid phase methods include electrochemical, sol-gel, coprecipitation, hydrothermal and/or solvo-thermal. The gas phase techniques include primarily pyrolysis-based techniques involving flames, plasmas and/or microwaves.

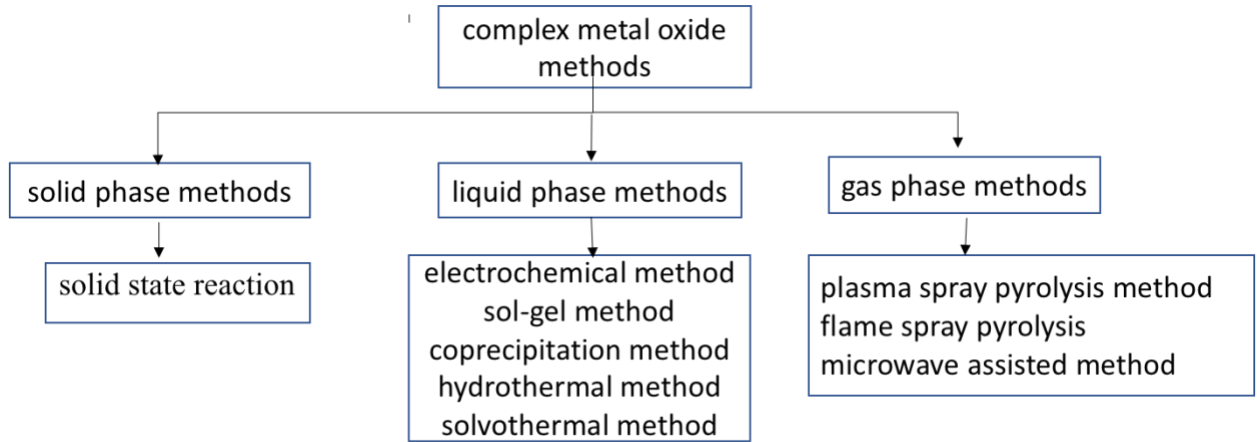


Figure 2.5 Summary of the methods for synthesis of the complex metal oxide materials

2.3.1 Solid state reaction method for the synthesis of complex metal oxides

Solid state reaction is common synthesis method to obtain the thermodynamically stable/meta stable products from reactants treated at high reaction temperature for long periods of times. Solid state reactions are intrinsically slow because of inhomogeneous mixing at the atomic level and diffusional limitations of reactants species through the product layers. The degrees of mixing and powder particle sizes determine the extent of reaction. The reaction starts at the points of contact between the initial components and continues successively by ionic inter diffusion through the product phase. Usually, solid state reactions take place over several hours to days to undergo complete reaction⁴⁶. Factors that affect the solid-state reaction are chemical and morphological properties of the reagents, the surface area, and thermodynamics of the solid-state reaction. Also, solid state reactions depends on the temperature, pressure and the environment of the reaction⁴⁷. The presence of inert atmosphere may alter the apparent kinetic characteristics of rate process

by hindering the removal of gaseous products in exothermic reaction environment by dissipating the heat. Even the presence of hydrogen or oxygen environment would change the reaction kinetics by reacting with reactants at the interfaces. Also, ball milling of reactants or presence of defects in the reactants may alter the kinetics of solid-state reaction by accelerating the diffusion mechanism in the reactant species. In general, solid-state reactions occur at interfaces under high temperature reaction conditions. The reactants usually move in opposite directions for the product formation. As shown in Figure 2.6, at the favorable reaction temperature, the reactants A, B react form intermediate product C. The product formation of D is further controlled by the diffusion of A, B through the product layer C and growth of the nucleates.

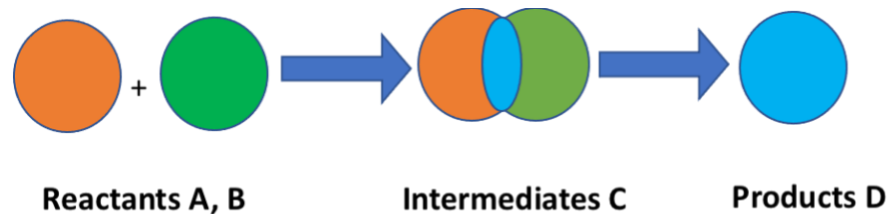


Figure 2.6. Schematic representation of process of solid-state reaction at the reactants (A, B) interface.

Reaction mechanism of solid-state alloying can be further detailed as below. Reactions at interfaces progress by simple nucleation of new phases followed by nuclei growth with reactant diffusion⁶⁰. The product formation is controlled by diffusion through the product layer, the product thickness is observed to follow the parabolic law

$$x^2=K*t,$$

Where K is rate constant obeying the Arrhenius equation.

Defects in the crystals have profound influence on the diffusion mechanisms. In general defects are classified into point defects, linear defects, and planar defects. Point

defects are atoms missing or in irregular places in the lattice. Point defects can be vacancies, substitutional defects, and interstitial defects. Linear defects are groups of atoms in irregular positions, screw dislocations and edge dislocations are examples of linear defects. Planar defects are the interfaces between the homogenous regions of the material such as grain boundaries, stacking faults and external surfaces. The higher the reaction temperature, the atoms can jump faster from original equilibrium position to another position and with the presence of higher amounts of vacancies. The number of actual vacancies N_v increases exponentially with the increase in the temperature as given below.

$$N_v = N_s \exp\left(\frac{-Ev}{K_B T}\right)$$

where N_v is the number of regular lattice sites, K_B is the Boltzmann constant, and Ev is the energy needed to form a vacant lattice site in a perfect crystal.

The presence of different types of defects give rise to different types of diffusion mechanisms. Vacancy diffusion mechanism: if an atom on the normal site jumps into adjacent unoccupied site, then the diffusion is said to be takes place by vacancy diffusion mechanism as shown in the Figure 2.7. Interstitial diffusion mechanism: when the atom on the interstitial site moves to one of the neighboring interstitial sites, then the diffusion occurs by an interstitial mechanism as shown in Figure 2.7. Interstitialcy diffusion mechanism: In the interstitialcy mechanism an interstitial atom pushes one of the nearest neighbors on a normal lattice site into another interstitial position and itself occupies the lattice site of the displaced atom. Also, solutes could diffuse through the dislocations and grain boundaries inside the material lattice as well.

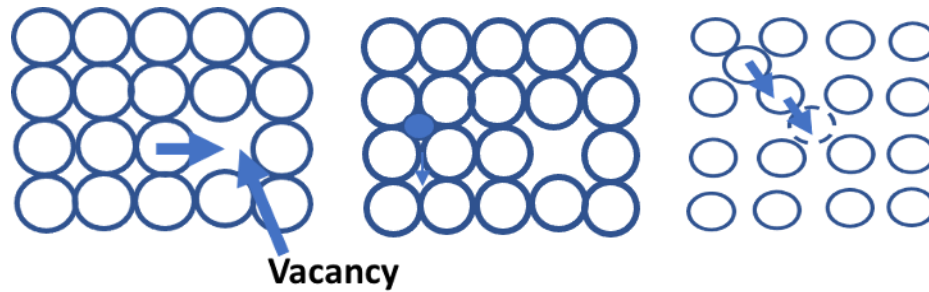


Figure 2.7. Sketch of diffusional process in solids by a) vacancy diffusion b) interstitial diffusion c) interstitialcy diffusion

Solid state reaction synthesis exists from the long time, however the first mechanistic understanding solid state reaction was described by Koch and Wagner⁶¹ for the formation of Ag_2HgI_4 from AgI and HgI_2 occurred by the counter diffusion of cations through the reaction product layer. Linder⁶² found from marker studies that zinc aluminate and nickel aluminate form from their component oxides by diffusion of zinc or nickel and oxygen through aluminate. Carter⁶³ found later that the formation of MgAl_2O_4 occurred by the similar mechanism of counter diffusion. Later, Schmalzried⁶⁴ reported that CoAlO_4 and NiAl_2O_4 are formed from the individual oxides by counter diffusion of cations through the spinel layer. Polycrystalline, transparent YAG ($\text{Y}_3\text{Al}_5\text{O}_{12}$) ceramics were fabricated by a solid-state reaction method by the using the high-purity Al_2O_3 and Y_2O_3 powders⁶⁵. Goodenough et al., Prepared LiCoO_2 by heating a pelletized mixture of lithium carbonate and cobalt carbonate in air at 900°C for 20 h followed by further heating⁶⁶. $\text{LiCo}_{0.333}\text{Ni}_{0.333}\text{Mn}_{0.333}\text{O}_2$ was prepared by solid state alloying mixing the precursor and alloying at higher temperatures^{67, 68}. Various thermodynamically stable materials of oxides, sulphides, nitrides oxides, nitrides, halides, carbides, borides, chalcogenides, intermetallic, alloys, solid solutions have been synthesized by solid state method. Solid state reaction mechanisms can be differ in different systems as detailed below.

1. Mechanism of alumina-titania system solid solution formation

For the formation of Al_2TiO_5 , the solid-state reaction between the alumina and titania under Ar atmosphere was investigated by the diffusion couple method. The temperature range of 1723 to 1873 K is used. Here, the diffusion of Al^{3+} and Ti^{4+} were related to the presence of vacancies. The vacancies are created by the dissolution of Al^{3+} in titania and Ti^{4+} in alumina. Among the three ions, the diffusion of oxygen ion is negligible compared to the diffusion of Ti ions and Al ions. This is due to the larger ionic radius of oxygen ion compared to the other ions. To maintain the charge balance, one cation vacancy is created for every three Ti^{4+} ions entering the alumina structure. The rate controlling step in the formation of Al_2TiO_5 is the interdiffusion of Ti and Al ions⁶⁹. The product formation is primarily related to the diffusion through the oxygen vacancies. The mechanism of ions transfer is shown in the Figure 2.8.

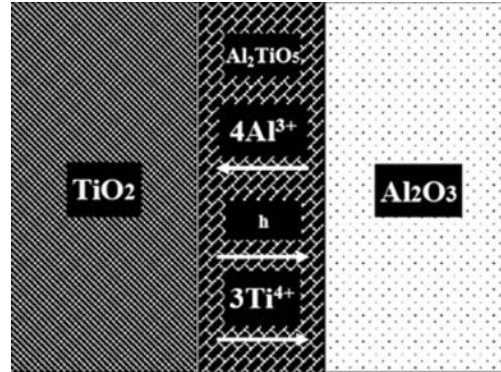


Figure 2.8. Schematic of formation process of Al_2TiO_5 in the alumina-titania diffusion couple (adapted from ⁶⁹)

2. Mechanism of $\text{Cd}_{1-x}\text{Zn}_x\text{Se}$ solid solution formation

The solid solution was synthesized by using the CdSe/ZnSe core/shell nanocrystals. Here the solid solution is achieved through the diffusion of Zn^{2+} ions by dissociation of bonds between Zn^{2+} and Se^{2-} ions. Furthermore, the formation mechanism is determined as the diffusion of Zn^{2+} through the matrices of $\text{Cd}^{2+}\text{-Se}^{2-}$ ⁷⁰.

3. Mechanism of BaSnO₃ formation from the reaction between the BaCO₃ and SnO₂

Here, barium stannate was prepared by the solid-state reaction of barium carbonate and tin oxide at a temperature of 600-1200 deg C for 15 h in dry air atmosphere. It was found that barium carbonate diffuses rapidly on the surface of tin oxide at the initial stage of reaction, forming a uniform shell of barium stannate. Later, the barium stannate grows in two different mechanisms depending on the calcination temperature. When the reaction was carried out below the 820 deg C, barium stannate phase further grew by diffusion of barium ions across the barium stannate layer to tin oxide phase. A higher temperature above 820 deg C, Ba₂SnO₄ were generated by the reaction between the barium stannate and barium carbonate. In this case, barium stannate formation could further promoted by the diffusion of barium ions from Ba₂SnO₄ across barium stannate to tin oxide. The rate limiting step in both cases was attributed to the diffusion of barium ions across the product layers⁷¹. The reaction mechanism is shown in Figure 2.9.

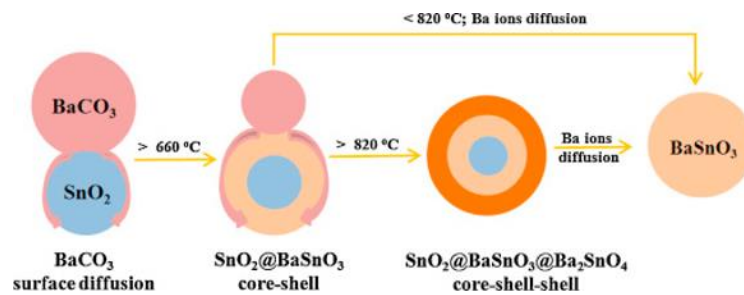


Figure 2.9. Sketch of the mechanism of BaSnO₃ formation from barium carbonate and tin oxide (adapted from ⁷¹)

4. Formation mechanism of MgCr₂O₄ spinel from magnesium oxide and chromium oxide

Spinel phase of MgCr₂O₄ is formed by the solid-state reaction of MgO and Cr₂O₃ at 1823 K in air atmosphere. The formation mechanism is related to the rate determining step of diffusion of chromium vacancy or chromium interstitial ion through the spinel. Two types of mechanisms of the spinel formation were considered from the charge neutrality.

One is the diffusion of chromium ion and hole or electron through the spinel and another is the counter diffusion of 2 moles of chromium ion (3+) and 3 moles of magnesium ion (2+) through the spinel to produce 4 moles of MgCr_2O_4 . This means that the mechanism of spinel formation by the counter diffusion of Mg^{2+} ion and Cr^{3+} ion through the spinel⁷².

2.3.2 Liquid phase methods for synthesis of complex metal oxides

Liquid techniques have attracted much attention to synthesize complex metal oxide materials. These methods are more efficient than the solid-state methods in terms of homogenous dispersion of reactants, low temperature requirements, and products with high phase purity.

2.3.2.1 Sol-gel method

In sol-gel method, liquid precursors were mixed in the required atomic ratio. Precursors undergo hydrolyzed, polycondensation, dried and calcined to yield the desired materials. The limitations of this method include the post calcination of reactants of the synthesized material, longer processing time and formation of impure phase amorphous materials. Materials such as perovskite-type complex oxides $\text{LaFe}_{1-y}\text{A}_y\text{O}_{3-\lambda}$ (A = Mn, Al, Co) were prepared by sol-gel method using citric acid as complex agent⁷³. Ultrafine high-temperature (HT) LiCoO_2 powders were synthesized by the sol-gel method using polyacrylic acid (PAA) as a chelating agent⁷⁴

2.3.2.2 Solvothermal method

Hydrothermal or solvothermal fabrication of materials is well known to prepare complex oxides. In this process, synthesis carried out in a closed vessel under high pressure. Here, the contents in the autoclave were heated to above 100 deg C (above the solvent normal boiling point). This method has limitations of requiring the soluble

precursors, large amounts of solvent, difficult to control the reaction conditions such P^H , viscosity, and temperature. This method also generates waste mineral acids such as HNO_3 and HCl . This method was used to synthesize the following spinel ferrites $CuFe_2O_4$, $MgFe_2O_4$ and $ZnFe_2O_4$, prepared in an autoclave under the same physical conditions but with two different liquid medium and different surfactant. Water is used as the medium and trisodium citrate as the surfactant for one method (Hydrothermal method) and ethylene glycol as the medium and polyethylene glycol as the surfactant for the second method (solvothermal method)⁷⁵.

2.3.2.3 Co-precipitation method

This method involves simultaneous occurrence of nucleation, growth, coarsening and agglomeration processes. This process includes the heating of the precipitates and liquor followed by the precipitation of mixed precursors. The formation of the mixed metal oxide materials depends on the impurity of the precipitate formed. It has advantages of simple and rapid preparation, easy control of particle size, and composition. This method operates at low temperature and is energy efficient method. However, this method has disadvantages of reactants needed to precipitate at similar rates, and time consuming. Cobalt ferrite ($CoFe_2O_4$) and spinel $LiNi_{0.5}Mn_{1.5}O_4$ have been synthesized by using the coprecipitation method^{76, 77}.

2.3.3 Gas phase methods for synthesis of complex metal oxides

Gas phase method has the advantage of direct conversion of liquid precursor aerosols to the solid particles after exposing to the heating media in a shorter time duration. Also, this process eliminates the presence of undesired waste materials in the reaction. The reaction process is completed very fast, and it is possible to achieve the metastable states

instead of the equilibrium state. Product particle size can be controlled by tuning the precursor droplet size of liquid in the aerosol. Also, composition of the product materials can be controlled by the controlling composition of the precursor aerosol media. Based on the type of energy supplied to the liquid aerosol precursor conversion to solid particle, these methods are classified into the flame pyrolysis and plasma pyrolysis.

2.3.3.1 Flame spray pyrolysis

In this process, the reactants are used in the form of salts or in the salt solution. They are converted into droplets by using the nebulizer or atomization techniques. Flame spray pyrolysis (FSP) process is a highly promising and versatile technique for the rapid and scalable synthesis of nanostructured materials with engineered functionalities. Various oxide materials have been synthesized by the flame spray pyrolysis at pilot scale of 100 g/h such as carbon black, fumed SiO₂, ZrO₂, Al₂O₃, FePO₄, ZnO, CeO₂/ZrO₂, and other ceramic nanoparticles⁷⁸. However, this method needs improvement in composition control of the mixed metal oxide materials due to the difference in evaporation rates and condensation rates of multi precursors.

2.3.3.2 Plasma spray pyrolysis

This method is very similar to the flame pyrolysis method except that the plasma is used as the heating media instead of flame. Plasmas can be considered as the fourth state of existence, together with solid, liquid and gas. Plasmas are defined as quasi-neutral gas of charged and neutral particles which exhibits the collective behavior⁷⁹. This concept has been demonstrated by synthesizing binary and ternary transition metal oxide solid solutions with control over entire range of composition using the metal precursor solution droplets oxidized by atmospheric oxygen plasma flame synthesis method⁸⁰. The mechanism of

plasma spray pyrolysis for mixed metal oxide materials are shown in Figure 2.10.

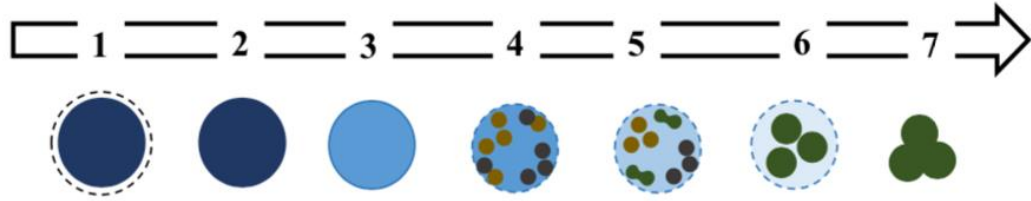


Figure 2.10. Schematic illustration of the proposed mechanism of plasma-processed nitrate-based precursors. The steps are (1) evaporation of precursor solvent (2) amorphous nitrate/nitrite/peroxynitrite phase formation (3) amorphous oxide phase formation (4) nucleation of monometallic oxides (5) alloying of oxides into intermediate compositions (6) growth of alloyed species (7) final non-stoichiometric oxide (adapted from ⁸¹)

Here the first nucleation of monometallic oxides was noticed, followed by the alloying of these monometallic phases into more stable bimetallic intermediate phase is observed. The mechanism strengthens the argument that the non-stoichiometric alloying is favorable at nano scale monometallic oxides.

2.4 Methods for the synthesis of binary metal oxide nanowires

Currently, binary metal oxide nanowires were synthesized by using bottom up approaches such as vapor phase synthesis²⁹, solution phase synthesis³⁰, metal catalyst assisted laser ablation technique and template-based methods^{19, 31}. Top-to-bottom approaches include metal assisted chemical etching and electron beam lithography⁹. The bottom-up approaches use vapor-solid-solid (VSS) and vapor-liquid-solid (VLS) method developed by Wagner in 1964¹⁰ with a foreign metal as catalyst to control one-dimensional growth³²⁻³⁴. However, all the conventional methods for binary metal oxide nanowires are limited to the milligram to gram scale synthesis. Many of the above-mentioned techniques are not scalable beyond gram scale. As shown Figure 2.11, Plasma flight technique seemed

to produce with $5 \times 10^{-5} \text{ g min}^{-1}$ of $\alpha\text{-Fe}_2\text{O}_3$ NWs and the production rate are much lower for the wet chemical techniques.

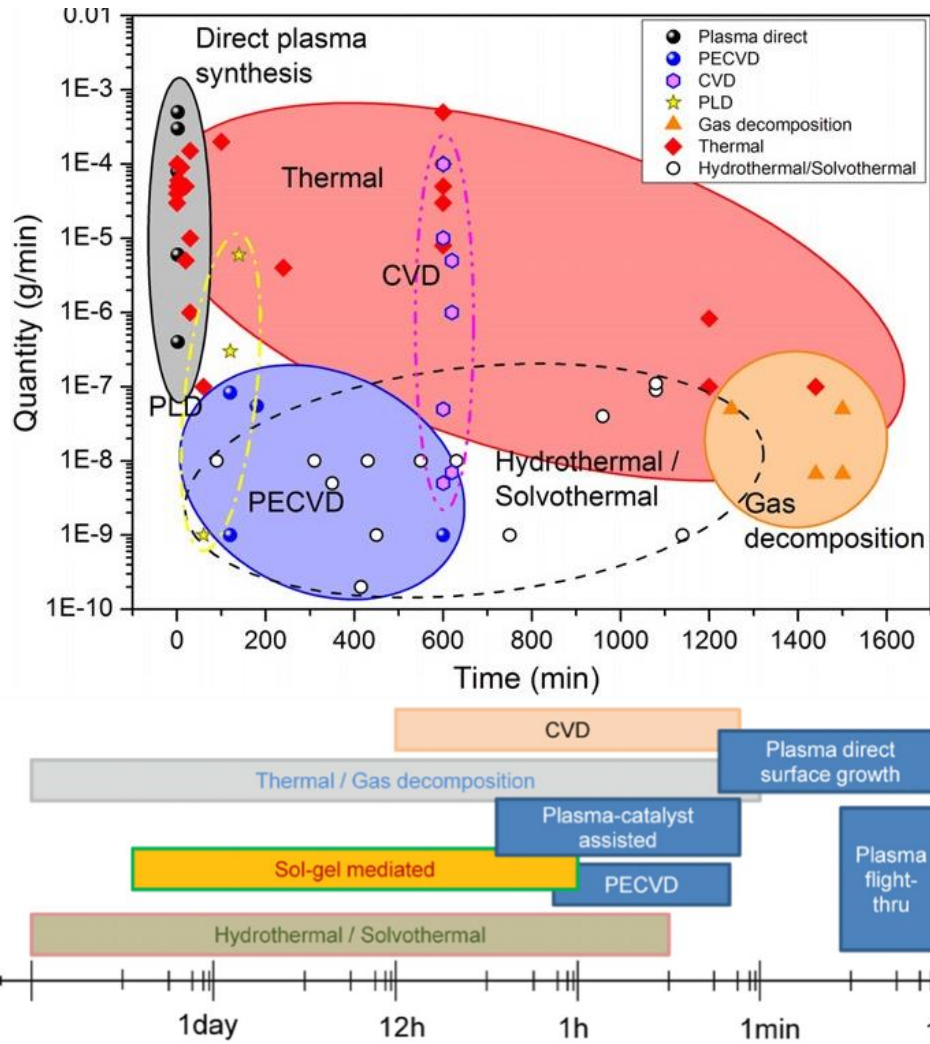


Figure 2.11. Time scale and quantity of material synthesized for iron oxide nanowires using the different synthesis methods (Adapted from ref.⁸²)

In the last few years, there has been a significant progress with scale-up of production of binary oxide nanowire materials such as TiO_2 , SnO_2 , ZnO , WO_3 , Al_2O_3 , MoO_3 , MnO_2 , FeO systems^{35, 36} using the dry manufacturing techniques. For example, nanowires of low melting point metals are synthesized by thermal oxidation of the metal precursors. The oxidation method involves direct exposure of molten metals to the

microwave plasma-excited gas or hydrocarbon flame in a fluidized bed reactor can result in oxide nanowires. The role of plasma activation here is to enable rapid dissolution of solutes such as oxygen and keeping the surface of molten metals clean. Growth condition needs to be maintained near the melting points of metal which preferentially support growth in one dimension such that metal remains in molten condition during the growth.

For, high melting point temperature metals, such as TiO_2 , WO_3 , MnO_2 , solvo plasma method was used to synthesize the nanowires. Solvo-plasma technology uses the atmospheric plasma or direct oxidation in the presence of alkali reagent to produce metal oxide and porous metal oxide NWs. Plasma oxidation allowed for the observed ultrafast timescales (on the order of a few tens of seconds) compared to conventional hydrothermal oxidation using large quantity of water (on the order of several hours). A simple lab-scale setup can produce up to 300 grams of nanowire powder per hour. The reaction time scales are on the order of a minute. This method is generic and is demonstrated with the synthesis of TiO_2 , Co_3O_4 , Mn_3O_4 and WO_3 nanowires as oxides of high melting point metals and SnO_2 and ZnO nanowires as oxides of low melting point metals. Respective metal or metal oxide powders mixed with alkali reagents when exposed directly to atmospheric pressure microwave plasma discharge for a few tens of seconds. Produced binary metal oxide nanowires. Solvo plasma method and direct oxidation growth mechanisms are described in Figure 2.12. In the first step, tin oxide forms a molten melt with the alkali metal during exposure to plasma flame. This process leads to the formation of molten metal alloy of potassium tin oxide material. The continuous dissolution of oxygen radicals into molten alloy forms the 1D-nanostructures. In the case of direct oxidation, the metal itself nucleates in the form of molten metal alloy.

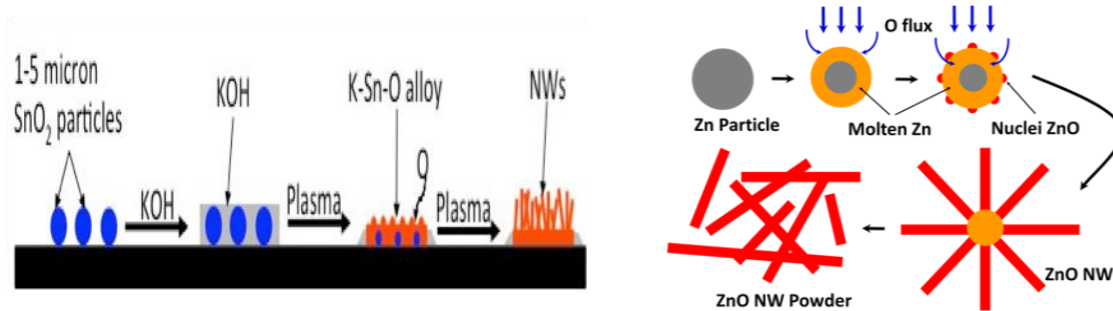


Figure 2.12. Schematic illustration of mechanism of formation of binary oxide NWs using solvo plasma for high melting point metals and direct oxidation of low melting point metals (Adapted from ref. ⁸³)

Challenges in the synthesis of mixed metal oxide nanowires

The synthesis methods used for binary oxide nanowires, i.e., direct oxidation techniques, cannot be used to synthesize the mixed metal oxide nanowires. The direct oxidation of mixture of metals produces mixture of separate oxide NWs. Because of the difference in melting points of the metals and their varied affinity towards oxygen, individual binary oxides grow out as separate oxide phases from molten melt. For example, to synthesize Cu-Zn mixed metal oxide nanowires using this approach. The metals need to be melted to form a mixed alloy with oxygen at the same temperature to grow out as the mixed metal oxide NWs (zinc has melting point of 419 deg C and copper melts at 1083 deg C). Even with the oxidation of an alloy of brass ($\text{Cu}_{0.7}\text{Zn}_{0.3}$) lead to the formation of different oxide phases. Initially, zinc oxide nanowire formation was observed due to the higher affinity of zinc towards the oxygen than that of Cu metal ⁸⁴.

By comparison, solvo plasma method needs to form a molten alloy of alkali with the respective metal precursors. The metals with stronger affinity to form a molten alloy with the alkali will grow faster, and this leads to the formation of separate oxide nanowire phases. Both methods seem unsuitable for the synthesis of mixed metal oxide nanowires.

2.5 Routes for the synthesis of mixed metal oxide nanowires

Mixed metal oxide nanowires are synthesized in gas phase, solution phase and solid phase form of the precursors. The compositional tunability while maintaining the targeted one-dimensional structure is crucial for the synthesis of mixed metal oxide nanowires. Thermodynamically stable oxides are easier to synthesize at the given temperature and composition. Based on the introduction of solute species, the methods are classified either as in-situ or ex-situ synthesis methods. In the in-situ synthesis method, all the reaction species are introduced together at the start of the reaction, whereas in the ex-situ synthesis method utilizes nanowire materials as solvent phase.

2.5.1 Synthesis of mixed metal oxide nanowires by in-situ methods

Several in-situ synthesis methods for mixed metal oxide nanowires are reported in the literature and they are template directed synthesis^{37, 38}, vapor phase method^{40, 41}, solution-based methods^{42, 43}, and hydrothermal methods²⁶

2.5.1.1 Template directed synthesis method

Templates of nanowires are mixed with the sol gel precursors followed by the removal or dissolution of templated nanowires. Also, solid substrates, surfactants, polymeric membranes, and porous alumina have been used as the sacrificial templates. The sol gel precursor nucleates on the surface of templated nanowires in the form of nanowires. The following materials have been synthesized with the template directed synthesis ZnFe₂O₄ Nanotubes using the ZnO NWs (Nanowires) as sacrificial templates³⁷. Poly ethylene glycol was used as a template for precursors of nickel and cobalt precursor in the synthesis of NiCoO₄ NWs³⁹. The precursors along with the PEG were dried and calcined to get mixed metal oxide nanowires. Also, iron alloyed ZnO NWs with a polymer template of P123 was

used as to alloy up to 5 at% of iron into the zinc oxide nanowires.⁸⁵ This method has the disadvantages of poor crystallinity with heterogenous nucleation growth, template removal and contamination caused from the templates. Sometimes, alloying precursor metals could be separated from the solutions as well.

2.5.1.1 Hydrothermal synthesis method

Hydrothermal synthesis methods were usually carried out at high pressures conditions in the autoclaves. Under high-pressure conditions, first the precursors dissolved into the solution and react each other to form a highly disordered phase intermediate (metal ion complex formation). It is found that nanowires seem to result when intermediates are supersaturated. The mechanism is not understood. The disadvantage of this method is that there is no control over the phase and morphology. It was observed that there were structural changes to the material as well. Also, smaller quantities, high reaction pressures and longer reaction times (in the order of 12-24h) as inherent disadvantages of this method.

The following examples of titania doped with nitrogen and boron illustrate the formation of mixed metal oxides nanowires. The predicted mechanism of formation is shown in Figure 2.13. Here, autoclave with TiN, NaOH, H₂O and air are kept under high pressure conditions. Initially, TiN dissolved into the solution and began to react with NaOH, O₂ to form a trititanate intermediate phase (Ti₃N_xO_{7-x}²⁻). Finally, Supersaturation of intermediate nanoclusters lead to the crystallization of Na_xTiN_yO_z nanorods. Using this method, less than 1 at% of boron or nitrogen alloyed into the titania nanorods⁸⁶.

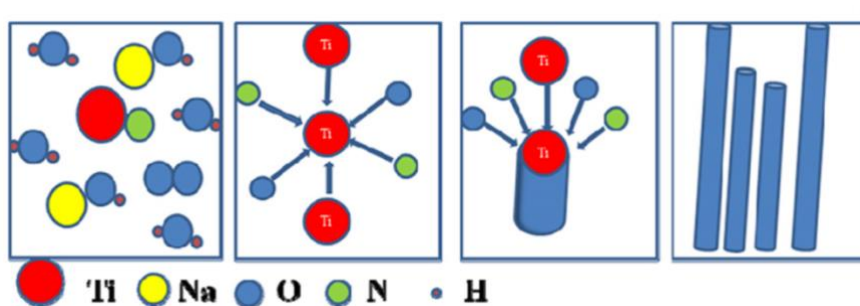


Figure 2.13. Depiction of mechanism of formation of $\text{Na}_x\text{TiN}_y\text{O}_z$ nanorods using hydrothermal method (Adapted from ref. ⁸⁶)

2.5.1.2 Vapor phase synthesis method

In the vapor phase methods nanowires grown by using the vapor liquid solid (VLS) or vapor solid (VS) mechanisms. The growth of nanowires consists of dissolution of vapor species into the nanosized liquid metal catalyst droplets followed by nucleation and supersaturation of the vapor species in the nucleate droplets to form the nanowires. In catalyst free vapor phase method, vapor species are subsequently transported and condensed onto the surface of a solid substrate placed in a zone with temperature lower than that of the source material. This process yielded very less amount of material (in mg's scale), use of metal catalyst, uniformity and substrate choice at the higher temperatures were the limitations of the vapor phase method. Using this method 2 at% of indium alloyed into the zinc oxide nanowires and copper (4 at%) alloyed into the zinc oxide nanowires ⁴⁰ ⁴¹.

For the system of $\text{Ir}_{1-x-y}\text{Ru}_x\text{V}_y\text{O}_2$ nanowires⁸⁷, ternary mixed metal oxide nanowires are directly grown on the Si(001) without the catalyst using simple vapor phase transport method. The growth of ternary mixture was likely because all three oxides have same crystal structure in a tetragonal phase as well as the similar ionic radius. For the synthesis of ternary mixture, various compositions of RuO_2 - IrO_2 powders mixed and sonicated for

homogenous mixing. The mixture is taken into a quartz boat and loaded into the quartz tube furnace in high temperature region, in another quartz boat VO_2 powder is located 5 cm downstream of $\text{RuO}_2\text{-IrO}_2$ precursor mixture. The growth substrate was kept 15 cm downstream of the $\text{RuO}_2\text{-IrO}_2$ precursor mixture. The temperature was at $1050\text{ }^\circ\text{C}$ and the helium as carrier gas with the flow of 400 sccm. The temperatures measured in the growth region is about 700 deg C . The mechanism is shown in Figure 2.14, first highly volatile VO_2 forms nano droplets on the substrate first, followed by dissolution of $\text{RuO}_2\text{-IrO}_2$ into the nanodroplets of VO_2 . Ostwald ripening and coalescence process to further grow the nanodroplets. Crystallization along favorable growth direction of the c-axis resulted in tetragonal crystal phase of mixed metal oxide nanowires.

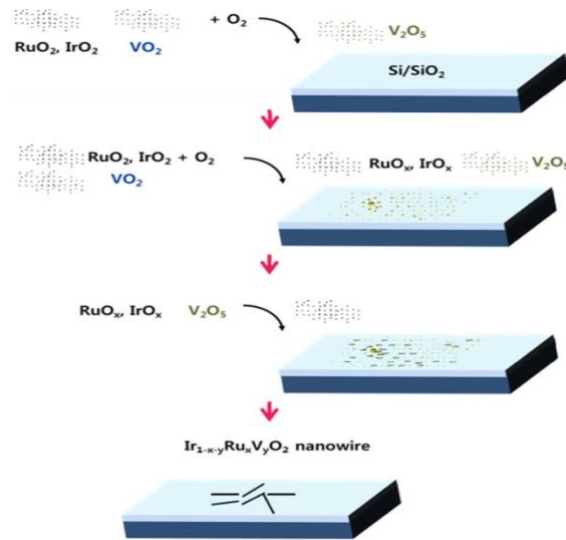


Figure 2.14. Schematic illustration of mechanism of formation of ternary oxide NWs using direct vapor phase transport (Adapted from Ref. ⁸⁷)

2.5.1.3 Solution phase synthesis method

In the solution phase synthesis method, all the reactant and dopants species are co-dissolved into the solution. The formation of aquo ions from the salts of precursor followed by hydration and condensation aquo salts leads to the growth of nanowires. The dopants

are usually incorporated during the growth of nanowires. Doping in non-aqueous solution avoids the formation of inert metal ion aquo complexes and this could favor the incorporation into the lattice of nanowires. Cobalt doped zinc oxide nanowires have been synthesized by co dissolving a desired amount of cobalt acetate with zinc acetate in trioctylamine. Typically 60mg samples were made with cobalt concentrations up to 11 at%⁴³. Also, zinc nitrate with different nickel acetate and HMT used to synthesize 1 at% nickel alloyed into the zinc oxide NWs⁴².

2.5.1.4 Solid state alloying synthesis method

Solid state reaction is common synthesis method to obtain the thermodynamically stable/meta stable products from reactants treated at high reaction temperature for longer times. Solid state alloying further extended to synthesis of metastable alloy thin films such as Co-doped ZnO, Mn-doped ZnO bulk materials⁸⁸. Solid state alloying in nano structures also been studied for the system of Mn or Eu doped ZnS sample. All precursors were milled together to obtain a homogenous mixture and calcined to obtain the doped samples. ZnFe₂O₄ nanoparticles were prepared using a low-temperature solid-state reaction (LTSSR) method, by mixing the precursors along NaOH in the desire molar ratio and calcined at 850 deg C temperature⁸⁹. Furthermore, solid state alloying was extended to the thermodynamically stable nanostructures. In this case, nanostructures are used to alloy with the nanosized precursors instead of bulk counterparts to obtain the desired alloys. For example, Barium titanate nanowires were obtained by solid-state reaction at 700 deg C using titania fiber-like crystals coated with BaCO₃ nanoparticles⁹⁰. Carbon-coated LiMn₂O₄ nanowire was prepared by using the carbon-coated MnO₂ nanowire and LiOH in the desired molar ratio were annealed in air environment⁹¹.

2.5.2 Synthesis of mixed metal oxide nanowires by ex-situ methods

All the in-situ methods are prone to change the crystallinity/morphology of alloyed materials compared with the unalloyed materials. Ex-situ method is used to prevent the change of crystallinity/morphology pristine nanowires during the alloying. Ex-situ alloying is a solid-state diffusion of solute precursors into the already synthesized nanowires. Ex-situ method could be used to meet the following disadvantages of in-situ methods. Such as vapor phase synthesis is limited by the different evaporation rates of multi precursors and foreign metal contamination. Solution phase synthesis often produces a material in poor crystalline form. The control of synthesis parameters (P_H , viscosity) for multi precursors, longer reaction times, multi-step processing, liquids processability at larger scales limits the synthesis of mixed metal oxide nanowires. Physical synthesis methods use high energy beams or electrons which destroy the structure of materials and surface of the nanostructures. The following ex-situ methods were used in the literature such as solid-state diffusion using ALD/sol-gel precursor coating, molecular beam epitaxy nanolayer diffusion and metal vapor vacuum arc (MEVVA) ion source doping.

2.5.2.1 Solid state diffusion method using the atomic layer deposition (ALD) technique

In the solid-state diffusion method, the atoms are randomly moved from one position to another by a thermally activated process. In this method, the pristine NWs are coated with thin nano layer (5-50nm) of solute precursors using the atomic layer deposition (ALD) process. The solute species solid state diffuse into the solvent NWs by using substitutional diffusion mechanism under inert atmosphere and higher temperature environments (700-800 deg C). This method was used for manganese alloyed into the titania NWs by using the titania NWs as solvent phase and by using the ALD deposition

of manganese precursor²⁰. Figure 2.15 shows the as synthesized nanowires were prepared by using the ALD coating method followed by solid state diffusion under the inert atmosphere. First titania nanowires were synthesized with the hydrothermal method and followed by coating with the manganese oxide using the ALD process. The nanolayers of manganese oxide were solid state diffused into the nanowires under inert atmosphere and high temperatures.

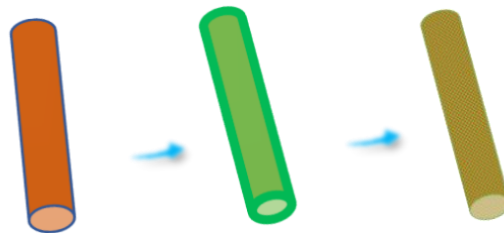


Figure 2.15. Schematic representation of the ex-situ synthesis of nanowires using the ALD method

2.5.2.2 Metal vapor vacuum arc (MEVVA) ion source doping method

Nickel doped ZnO NWs are prepared by using the ion source doping method. Here, zinc oxide nanowires were prepared by using VLS (vapor- liquid- solid) growth mechanism. As shown in Figure 2.16 the prepared zinc oxide nanowires doped by MEVVA with Ni ion at a dose of $2 \times 10^7 \text{ cm}^{-2}$ and an incident angle of 5° . The vertical NWs are kept at an extraction voltage of 100 kV and a temperature of 200 deg C. The doped samples were then treated by thermal annealing at 950 deg C for 2 h in oxygen environment for eliminating the doping induced defects. However, the high energy doping sources damages the structure of nanowires compared to pristine nanowires, and there is a possibility to synthesize non uniform alloyed nanowires.

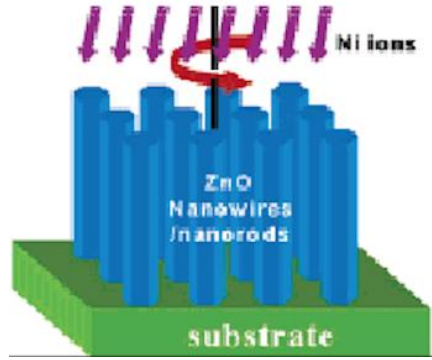


Figure 2.16. Schematic illustration of ex-situ synthesis of nanowires using the MEVVA ion source doping method (Adapted from ref. ⁴⁵)

2.5.2.3 Sol-gel precursor coating method

As shown in Figure 2.17 tungsten and carbon ex-situ doped into the titania NWs by using the sol-gel precursor method⁴⁴. As prepared TiO₂ NWs from hydrothermal method are dip coated with sol gel tungsten precursor and dried by blowing the air. This left a uniform thin layer of W precursor on the surface of TiO₂ NWs. The tungsten precursor coated NWs are exposed in the hydrocarbon flame for short duration of 2 min and this would promote the diffusion tungsten into the titania NWs. Finally, for carbon doping the tungsten-alloyed titania NWs annealed in CO atmosphere to at 550 deg C for 30min in a tube furnace. However, this method yielded non-uniform alloying of the tungsten and carbon on the surface of nanowires.

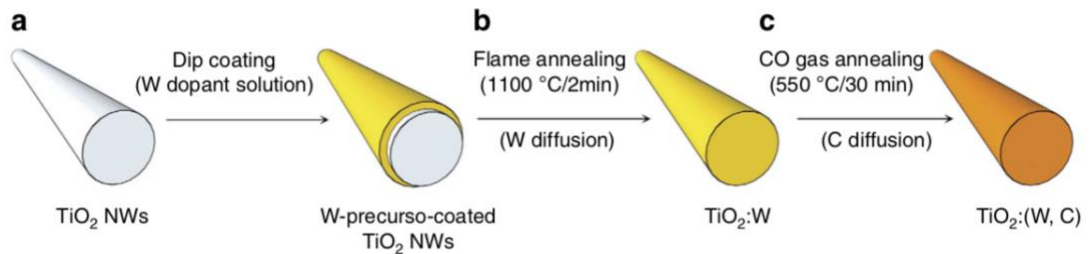


Figure 2.17. Schematic of the ex-situ synthesis of nanowires using the sol-gel precursor doping method (Adapted from ref.⁴⁴)

Table 2.1. Selected mixed metal oxide nanowires synthesis routes

Method used	Material synthesized	Application used and performance	Remarks	Ref
ALD coating followed by solid state diffusion	TiO ₂ Nanowires were alloyed with manganese and zirconium	Used in the photo electrochemical water splitting, obtained the photo current density 50 mAcm ⁻² at $\eta=500$ mV.	8 at% of Mn is alloyed into the titania nanowires. Trace levels of zirconium is alloyed. Solid state diffusion in nanostructures favored the alloying process.	20
ALD coating of titanium precursor on iron oxide followed by the solid-state diffusion.	Iron oxide (Fe ₂ O ₃ nanorods alloyed with titanium)	Used for photo electrochemical water splitting. photocurrent density of 2.28 mA/cm ² at 1.23 V vs reversible hydrogen electrode (RHE) and 4.18 mA/cm ² at 1.70 V vs RHE.	Ti doping promoted band bending and largely increased the carrier density as well as the surface state. Uniformly alloyed the titanium into the iron oxide nanowires.	28
Sol gel dip coating of precursor on titania nanowires followed by the flame exposure	Tungsten alloyed into the titania nanowires	Photocurrent density of 1.22 and 1.41 mA/cm ² , is obtained respectively, for W/TiO ₂ and TiO ₂ :C at 1.23 Vs RHE.	Non uniform alloying of the tungsten and carbon on the surface of nanowires. Because of faster time scales and materials are not distributed uniformly. Variation of 13 at% to 1 at% from surface to bulk of nanowire is observed.	44
Metal vapor vacuum arc (MEVVA) ion source doping	Nickel alloyed into the ZnO NW's	The UV emission peak is centered at 389 nm for the Ni-doped ZnO NWs, this exhibits a red shift of 5 nm compared to the undoped ZnO NWs. Electrical conductivity was	Upto 6 at% of Ni is doped in the ZnO NWs. Defects in the nanowires were observed due to exposure of the high energy beam on the surface of the nano structures.	45

		enhanced for over 30 times after doping.		
Solution-phase synthesis	Zinc oxide nanowires alloyed with cobalt	A full sun efficiency of 1.5% was demonstrated with a nanowire photoanode.	ZnO nanowires were doped with cobalt. Alloyed upto 11 at% of cobalt. However, more data analysis needs to be performed to confirm.	43
Vapor phase synthesis	Indium 2 at% alloyed into the zinc oxide nanowires	The photoluminescence spectrum for the doped sample shown a blue shift in the UV region, shows a prominent tuning in the optical band gap. Also, the electrical resistivity is decreased.	Indium doped NWs are found to be single crystalline with [0 0 0 1] as the preferred growth direction. Small scale milli gram sample was synthesized.	40
Vapor phase synthesis (Chemical vapor deposition)	Cu-doped ZnO nano nails and nanoneedles.	The band-edge UV emission and the broad green emission are red-shifted by ~7 and 20 nm. X-ray photoelectron spectroscopy study revealed a higher level of oxygen vacancies in nanoneedles, and this was found to enhance the green emission.	Cu-doped zno nanoneedles and nano nails were synthesized by thermally evaporating Zn and CuCl ₂ powders. Copper (4 at%) alloyed into the zinc oxide.	41
Vapor phase transport	Ir _{1-x} - _y Ru _x V _y O ₂ nanowires on Si substrate	Not applied	The growth of ternary mixture was likely because all the three oxides have same crystal structure in a tetragonal phase and similar ionic radius.	87

Hydrothermal method	Titania alloyed with nitrogen and boron	The BNTRs showed a higher photocatalytic activity and a bigger photocurrent response than N-TiO ₂ nanorods under visible light irradiation.	Less than 1 at% of boron or nitrogen alloyed into the titania nanorods.	86
Template directed synthesis	Iron alloyed ZnO NWs	Not applied	Polymer template of P123 was used as to alloy upto 5 at% of iron into the zinc oxide nanowires.	37 90
Solid state reaction	BaTiO ₃ Nanowires	Used as a ferroelectric material. Piezo response force microscopy measurements show a strong piezo activity and stripe domain patterns with domain width of 20-50 nm.	Single crystal BaTiO ₃ nanowires with tetragonal structure were obtained by an original solid-state process. By using the layered titania nanowires coated with BaCO ₃ nanocrystals as reactive templates.	90
Solid state reaction	Carbon coated LiMn ₂ O ₄ material	Used as high-power cathode materials in lithium-ion batteries	Prepared by using the carbon coated MnO ₂ nanowire and LiOH in the desired molar ratio and They were thermally annealed in air environment.	91
Auto combustion method	Mn doped zinc oxide nanowires	Optical absorption studies show an increment in the band gap with increasing Mn content	Mn doped ZnO was synthesized by a combustion method from the nitrates of Zn and Mn taken in the appropriate ratio. Higher thermodynamic solubility of Mn in zinc oxide favored this process feasible.	92

2.6 Applications of mixed metal oxide nanowires in energy conversion processes

Particularly, compositional tunability of the mixed metal oxide nanowires is used for introducing the oxygen vacancies, structural defects, to change the binding energy of the active sites and tuning acid-base sites on the exposed active facets along with the unique structural characteristics of the nanowires²⁰⁻²². Mixed metal oxide nanowires with highly dispersed metals at atomic scale could provide the synergistic interactions that are not possible with traditional metal supported nanowires. These special properties are useful in heterogenous catalysis, electrochemical catalysis, photo catalyst and as transparent conducting oxides.

2.6.1 Heterogenous catalysis

Catalysis plays an important role in bulk chemical production, fossil fuels processing and in environmental pollution control, where efficient and selective chemical transformations are of great concern. Nanowires are used in heterogenous catalysis due to their large surface to volume ratios, active surface facets and surface chemical composition. The catalytic properties of materials are determined by its electronic structure, so the goal is to engineer the electronic structure by changing the composition and morphology⁹³. Mixed metal oxide nanowires play important role in control of electronic properties by modifying the composition of nanowire. For example, for the reduction of nitrobenzene on $\text{La}_{0.8}\text{Sr}_{0.2}\text{FeO}_3$, the activation energy is 73.9 kJ/mol compared to the stable oxides LaFeO_3 (88.9 kJ/mol), SrFeO_3 (84.4 kJ/mol) activation energies³. The lower the activation energy means the better the catalytic activity. Mixed metal oxide nanowires shown high catalytic performance for reaction of CO oxidation to CO_2 . This reaction was carried out

using ceria nanowires alloyed with foreign metal (lanthanides) on a selective facet. Higher activity is attributed to the formation of high-density oxygen vacancies and enhanced mobility of oxygen from bulk to surface of active facets of alloyed ceria NWs²⁶.

2.6.2 Photo electrochemical catalysis

Photo electrochemical catalysis involves the conversion of solar energy into chemical energy stored in the form of liquid fuels or hydrogen. Two major processes such as photo electrochemical water splitting: electrolysis of water in hydrogen and oxygen under solar light and carbon dioxide electrochemical reduction to hydrocarbon chemicals are under intensive research^{94, 95}. Nanostructured wide bandgap metal oxide semiconductors exhibit an enhanced PEC (Photo electrochemical conversion) performance compared to the bulk materials. Nevertheless, these metal oxides still have unfavorable material properties such as limited visible light absorption and electrochemical instability. These should be addressed through rational chemical modifications such as band gap engineering through elemental doping, improving the electronic conductivity by modifying electronic band structures. For example, titanium (Ti) doped hematite nanorods with precise control of Ti amount and morphology for highly effective PEC water splitting been used to obtain pronounced photocurrent density of 2.28 mA/cm^2 at 1.23 V vs reversible hydrogen electrode (RHE) and 4.18 mA/cm^2 at 1.70 V vs RHE, respectively. The high performance attributed to the Ti doping promoted the band bending, long term stability and increased the carrier density²⁸.

Electrodes that have been developed for CO₂ reduction suffer from the low energy conversion efficiency, low selectivity, low faradaic efficiency, poor stability and unable to suppress the competing hydrogen evolution reaction. Recently, metal alloyed

nanostructures drawn great attention because they have ability to improve the stability of key intermediates. For example, bimetallic CuSn nanowires (NWs) used for electrochemical CO₂ reduction reaction with a formate selectivity of 90.2% at -1.0 V vs RHE, superior performance is ascribed to the Sn atoms doping on CuO (111) facet as well as the selective adsorption of intermediates to suppress the hydrogen reaction²⁷.

2.7 Chapter summary

In this chapter, various synthesis methods for the complex metal oxide materials in general and binary and mixed metal oxide nanowires had been discussed. The methods that are used for the synthesis of binary metal oxide may not be used for the synthesis of mixed metal oxide nanowires. There are several in-situ and ex-situ methods reported for the synthesis of mixed metal oxide nanowires. However, in-situ methods have inherent limitations. In vapor phase synthesis method, different evaporation rates of multi precursors and foreign metal contamination are hindrances to this method. Solution phase synthesis often produces a material in poor crystalline form. The control of synthesis parameters (P_H, viscosity) for multi precursors, longer reaction times, multi-step processing, and liquids processability at larger scale are limitations of this method. Physical synthesis methods use high energy beams or electrons which destroy the structure of materials and surface of the nanostructures. Ex-situ synthesis methods seemed to be promising for the synthesis of mixed metal oxide nanowires in terms of material quality and easy to scale up. However, ALD coating for large scale manufacturing of material would not be feasible. So, in this dissertation a simple method based on using dry or liquid precursor coating on binary metal oxide nanowires and their solid-state diffusion under inert atmosphere to synthesize mixed metal oxide will be discussed. Also, the role of

thermodynamics at nanoscale favoring the solid-state reactions is explained. The importance of use of mixed metal oxide nanowires in the energy conversion applications is explained as well

CHAPTER 3 EXPERIMENTAL METHODS AND CHARACTERIZATION TECHNIQUES

3.1 Introduction

This chapter describes details about the experimental procedure of synthesis of binary and mixed metal oxide nanowire systems. It includes the type of reactors used, reaction conditions, design of reactors and construction of reactors. Several characterization and analytical methods employed to determine the qualitative analysis and quantitative analysis of composition, structure analysis and phase analysis are described here. A collection of characterization techniques such as scanning electron microscopy (SEM), energy dispersive spectroscopy (EDX), X-ray diffractometer (XRD), Brunauer-Emmett-Teller (BET) surface area analysis, transmission electron microscopy (TEM), differential scanning calorimetry (DSC) and thermogravimetric analysis (TGA) will be discussed in this chapter. Electroanalytical techniques such as chrono amperometry, cyclic voltammetry, electrode preparation and gas chromatography techniques will be covered in this chapter as well.

3.2 Atmospheric microwave upstream plasma system

The microwave plasma system includes standard components such as a magnetron, a circulator, a dummy load, a power detector, an impedance matching system, and a custom-design applicator. All the components are in communication through a rectangular waveguide WR284. The magnetron generates microwaves of 2.45 GHz into the

waveguide. The circulator connected to water cooled dummy load only allows the propagation in one direction and is used to prevent the reflected microwave from entering the magnetron. The power detector measures the forward and reflected power. The impedance matching system comprises of a circuit of resistors and capacitors matches the impedance of the source (magnetron) and the load (plasma) for maximum power transmission and to reduce the reflected power to zero. The applicator is designed in such a way that the microwave is concentrated at the center of a quartz tube inserted in applicator. Argon is introduced into the applicator at an angle (60 deg) to form the downward helical flow. The helical flow is used to prevent the heating on quartz tube causing by plasma flame. A copper rod is used create the dielectric breakdown of gases and to ignite the plasma. The plasma is ignited with low dielectric breakdown gas such as Ar. Later, the plasma flame is maintained by introducing gases such as air, oxygen, nitrogen, or hydrogen depends on the application. A schematic of plasma system is shown Figure 3.1 below.

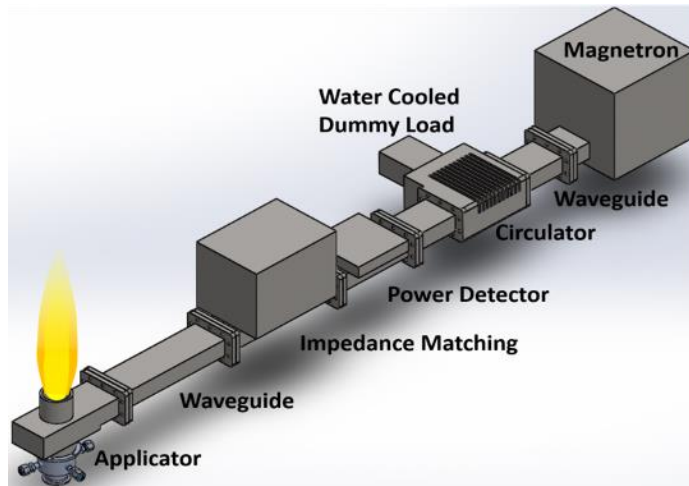


Figure 3.1. Sketch of the atmospheric microwave upstream plasma reactor system used for binary metal oxide nanowire synthesis

3.3 Synthesis procedure for porous nanowires (Solvo plasma method)

Metal/metal oxide particles (1-5 μm size, Atlantic Equipment Engineer, Inc) are mixed with KOH/KCl powder in a 1.5-3:1 (Metal-salt) ratio by atomic percentage. The mixture is grounded, and desired amount of water is added to make a paste. The precursor paste coated about 100 microns thick on a 25 x 25 mm quartz substrate. The substrate is then exposed to the plasma flame at power ranges of 1.0-1.4 kW, with the flowrate of 10 lpm of Air for 30 seconds to 5 min. The thick film from the quartz substrate is scraped off with the razor leaving small amount on it to avoid contamination from the quartz substrate and grounded material to a fine powder. The formed products are dissolved in 100 ml-1L deionized water in beaker and then ultra-sonicated for 1 hour. After ultra-sonication, the resultant mixture is taken into the centrifuge bottles and leaving behind the undissolved salts at bottom. The solution mixture is centrifuged for 1 hour at 7000rpm. The precipitate is separated out from the centrifuge bottles and annealed at 80°C to get the potassium-contained metal oxide nanowires. The nanowires are immersed in 0.1 M hydrogen chloride solution for 1 hour to etch the potassium from the metal oxide nanowires. Then the clarified solution is removed

and dried the mixture at 80°C. The dried powder is calcined at 500°C for 2-4 hours. Thus, the porous metal oxide nanowires are formed.

3.4 Synthesis procedure for mixed metal oxide nanowires

As prepared porous nanowires in the solvo plasma method weighted along with the desired composition of solute precursor of solid or liquid lithium hydroxide, lithium carbonate or copper nitrate, copper acetate, cobalt nitrate, or zirconyl nitrate. The precursor is dissolved in water to make completely soluble solution. The solution is then mixed with the porous nanowires to make a thick paste, the resulting material is dried under atmosphere at 100-120 deg C for 2-4 h to dry out the water. The dried material is collected in the crucibles and vacuum annealed in vacuum furnace as shown in Figure 3.2 at a temperature range of 190-500 deg C for 30 min -1h under the inert atmosphere to synthesize the alloyed nanowires. The system is kept under 10-15 tor inert nitrogen atmosphere pressure with nitrogen flowrate maintained at around 100-200 sccm.

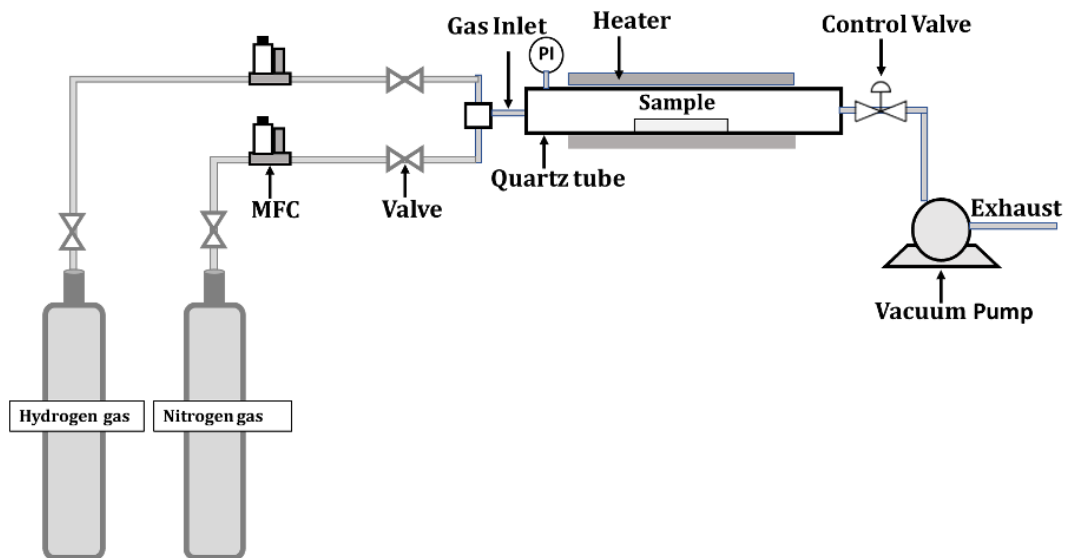


Figure 3.2. Schematic representation of synthesis of mixed metal oxide nanowires with the vacuum furnace

3.5 Materials characterization techniques

3.5.1 Scanning electron microscopy analysis

Scanning electron microscope comprises of two main components- (i) electron gun column and (ii) detector. The electron gun column generates and focuses the electrons on the sample. An electron gun is consisting of a cathode that emits electrons by thermal heating or by applying high electric fields. When the cathode material is heated resistively by applying a high voltage, electrons gain kinetic energy, when kinetic energy of the electrons exceeds the work function, a thermodynamic barrier for electron emission into vacuum, the electrons are emitted from the hot cathode. This mechanism is called as thermionic emission. Tungsten metal and lanthanum hexaboride (LaB_6) are typically used as the materials for the thermionic emission cathodes.

Electron emission by field emission happens through tunneling effect, when a high voltage is applied to material with a very sharp tip, the potential at the tip of the material is deformed creating a pathway for the escape of electrons. The electrons emitted from the cathode are accelerated by the electric field applied between the wehnelt cap and the anode. The function of the wehnelt is to crudely focus the electron beam that is emitted in all directions from the cathode and to control the number of electrons reaching the anode. The point where the electron beam converges after the wehnelt is called as the cross-over point. Electromagnetic lenses are used to further focus the electron beam, these comprise of wound coils enclosed in cast iron yolks with a small narrow opening. When a current pass through the coils, it produces a magnetic field around that axis of the coils that deflects and focuses the electron beam. The strength of the magnetic field can be varied by changing the current passing through the coils. The condenser lens is used to reduce the diameter of

the electron beam that has been accelerated towards the anode and the objective lens is used to focus the electron beam on the sample. Defects in the coils can change the circular cross-section of the electron beam to an elliptical cross-section. Stigmators apply a magnetic field to correct this defect.

The focused electron beam from the objective lens can be rastered along the sample using scanning coils that deflect the position of the electron beam by applying a small voltage between the coils. The secondary electrons emanating from the sample and are finally detected using an everhart-thornley detector (ETD).^{96, 97} The SEM is coupled with an energy dispersive spectroscopy (EDX) which determines the elemental composition and elemental mapping of the sample.

In a typical experiment the following instrument parameter were used. FEI Nova 600 is used for high resolution images typically operated in a voltage range of 10-30 kV and a TESCAN VEGA3 SB-Easy Probe scanning electron microscopes (SEM) is used for low resolution imaging and EDX profiles with a voltage operating window of 10-30 kV.

3.5.2 TEM (Transmission electron microscopy) analysis

The components in the electron gun column of the TEM are like that of SEM. SEM uses secondary electrons and back scattered electrons are detected. The TEM is used to detect the elastically scattered electrons that are transmitted through the specimen. Transmission electron microscopy (TEM) experiments uses a Tecnai FEI microscope equipped with a Gatan 2002 GIF system. The samples were prepared on a TEM grid (PELCO® Center-Marked Grids, 50 mesh, 3.0 mm O.D) in powder the form without any further processing. The accelerating voltage used was 200 kV. TEM-EDX analysis was used to obtain the composition analysis data. Copper grids were used when the nickel

element present in the sample and nickel grids were used when copper element present in the samples for EDX analysis.

3.5.3 X-ray diffraction analysis

X-ray is used a non-destructive technique used to identify the phase, grain size, crystal defects and crystallinity of the materials. X-ray diffraction (XRD) analysis performed with an HR XRD Bruker D8 Discover diffractometer. The equipment operated at 40 kV and 40 mA with Cu K α ($\lambda = 0.1548$ nm) radiation. The scan speed used was 0.5-2 s per step with a step size of 0.02°. The sample XRD patterns were scanned between 10-90° using the θ -2 θ method. Diffrac eva software and powder diffraction file (PDF) were used to analyze the phases and alloying into the nanowires.

3.5.4 BET surface area analysis

To measure the surface area of the nanowires, Brunauer–Emmett–Teller (BET) analysis was performed with a micromeritics tristar 3000 porosimeter. Samples were carefully weighed and degassed with nitrogen before performing the measurements to remove any adsorbed contaminants from the surface and pores of the sample. Calculations for the BET surface area were performed using the triStar 3000 analysis program.

3.5.5 Thermogravimetry (TGA-DSC) analysis

A thermogravimetric analysis (TGA) (model SDT Q600 from TA Instruments) used to analyze the amount of carbon deposited on the catalyst samples and to identify the precursors decomposition temperature. Around 15 mg of sample material were placed in an alumina sample pan. The sample materials were exposed with the air flow of 100 ml/min. The instrument temperature is raised up to 800 deg C by increasing the temperature

at rate of 5-10 deg/min. Based on the weight loss analysis of sample the amount of carbon present is analyzed.

3.5.6 Differential scanning calorimetry (DSC) analysis

Differential scanning calorimetry (DSC) is an analytical thermal analysis methodology that measures the heat flow required to scan temperature in a predetermined manner, while the heat flow is quantified as a relative value over a reference with known stable thermal properties. The changes in enthalpy are measured with TA instruments Q20. DSC provides the rapid and precise transition temperature determination using the small amount of sample. The measurements shown in Figure 3.3 are usually determined. DSC is used to obtain the Arrhenius equation parameters for reactions involving the non-isothermal kinetics.

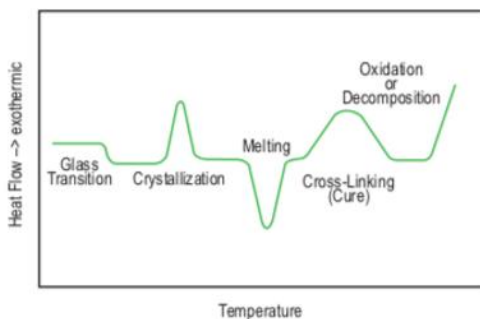


Figure 3.3. Schematic of transition of events during the heating of a sample.

3.6 Experimental procedure of the DMR (dry methane reforming) reaction

Dry methane reforming reaction is performed in a packed bed quartz tube reactor aligned with the vertical furnace and connected by mass flow controllers, gas chromatography (GC). The gas composition is controlled by the mass flow controllers calibrated with He, H₂, CO₂ and CH₄ gases. The outlet stream is partly injected into the

GC valve to identify the unreactive gases and products as shown in the Figure 3.4. The reaction conditions of temperature range from 700-850 deg C, at atmospheric pressure, with 0.5g catalyst powder, with an GHSV (gas hourly space velocity) of 6-12 Lg⁻¹h⁻¹ of reactive gases CH₄-25-50 sccm, CO₂-25-50 sccm, and nitrogen as unreactive gas with flowrate of 15 sccm feed to the reactor. The typical process includes packing the catalyst into the quartz tube reactor using the glass wool as support followed by heating the furnace with the flow of nitrogen through the reactor at 20 sccm. The temperature is raised at a ramp rate of 10 deg/min after reaching the reaction temperature conditions reactant gases are flown through the reactor. Part of the product stream is injected into the GC and the remaining gas stream is flown through the exhaust.

The GC system is an Agilent 7820A instrument with a thermal conductivity detector (TCD) and a flame ionization detector (FID) with a Shin Carbon ST micro packed column (100/120 mesh, 2m, 1/16in. OD, 1.0 mm ID). The GC analysis is performed under a flow of 10 ml/min of He as carrier gas and heating program (40 °C for 2 min, 10 °C/min heating to 220 °C and hold it for 3 min).

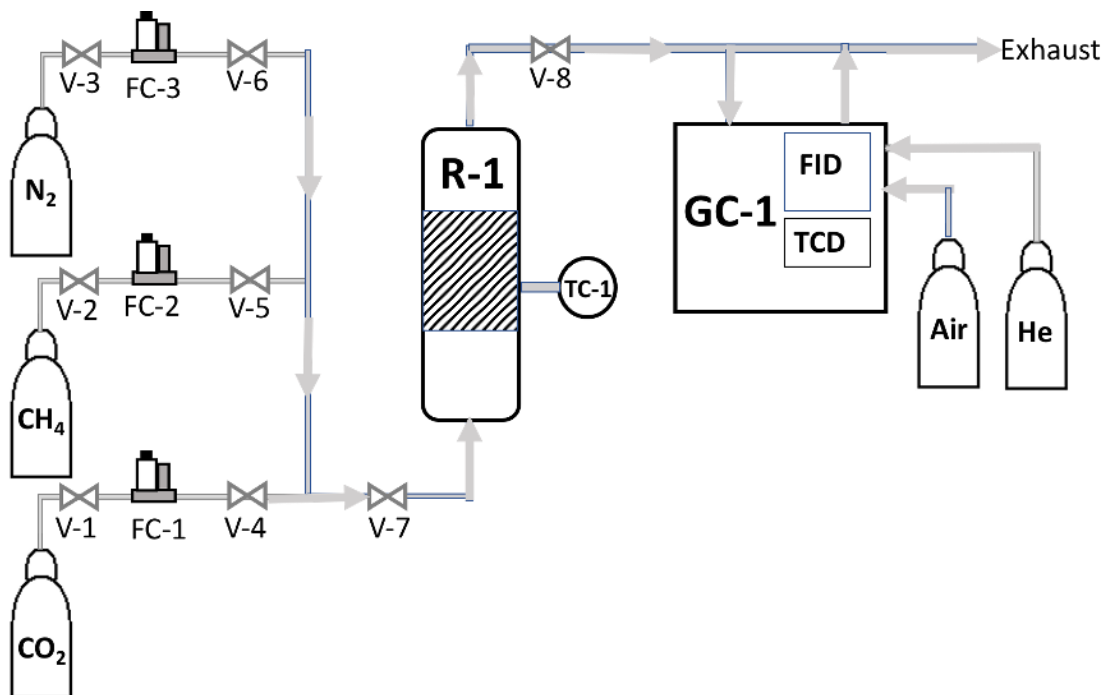


Figure 3.4. Schematic of packed bed reactor and GC system used for the testing of dry methane reforming catalyst

3.7 Electrochemical measurements and electrode preparation

Electrochemical experiments were performed in a customized gas-tight, 4-neck glass electrochemical cell. The samples were prepared by drop-casting a particle suspension on a porous carbon gas diffusion layer (GDL, Sigracet 35 BC, FuelCellsEtc) electrode. For each electrode of 5 cm² projected area, 20 mg of synthesized Sn-NWs, Sn-NCs, or commercially available Sn-NPs (~15 nm diameter) were mixed with 100 g, 5 wt% Nafion in 1 ml isopropanol (Sigma-Aldrich). After the deposition via drop-casting, the electrodes were dried at 60 °C for 1 h. During electrochemical measurements, an anion exchange membrane (Solemn AMV) was used to separate cathode and anode compartments to prevent oxidation of the reduction products at the anode. The CO₂ (99.99%, Specialty Gases) was injected into the catholyte at a flow rate of 10 sccm using a calibrated mass flow controller (MKS Instruments) and gas bubbler. A Pt mesh was used

as the counter electrode with an Ag/AgCl (saturated KCl) as the reference electrode. All CO₂ reduction experiments were performed in CO₂-saturated 0.1 M KHCO₃ (99.99%, Sigma Aldrich) aqueous solution at room temperature (298 K). A potentiostat (Biologic SP-200) with electrochemical impedance spectroscopy (EIS) was used for all measurements. The results are reported on a reversible hydrogen electrode (RHE) scale according to $V_{RHE} = V_{Ag/AgCl} + 0.197 + 0.059 \cdot \text{pH}_{\text{soln}}$. The solution pH was measured to be 6.8. Potentiostatic EIS measurements were performed before every experiment to determine the uncompensated solution resistance, R_u , and the potentiostat subsequently compensated for 85% of R_u during electrolysis. The current densities were determined relative to the geometric projected electrode area throughout this study.

Electrochemical product analysis

CO₂ reduction products were measured by gas chromatography (GC, SRI 8610) and nuclear magnetic resonance (NMR, Bruker 400 MHz) for the gas and liquid products, respectively. Both instruments were calibrated with standard gases or liquid solutions. For real-time gas phase product analysis, the outlet of the cathode compartment was connected to the GC inlet. The GC system used an automatic valve injection (1 mL sample) and a thermal conductivity detector (TCD) and flame ionization detector (FID). Ultra-high purity nitrogen (99.99%, Specialty Gases) was used as the carrier gas for all experiments and was chosen to enable accurate hydrogen quantification. In addition, NMR spectroscopy (Varian 400 MHz NMR spectrometer) was used to analyze and quantify the products in the liquid phase by performing ¹H NMR experiments. Samples were prepared by mixing D₂O and electrolyte aliquots in a 1:1 volume ratio. Faradaic efficiency (F.E.) was calculated for the chronoamperometric measurements by determining the charge required to produce the

measured product concentration and dividing by the total charge passed during the time the sample underwent electrolysis.

CHAPTER 4 SYNTHESIS OF BINARY POROUS METAL OXIDE NANOWIRES

Porous nanowires have attracted a lot of attention due to their higher surface area to volume ratios compared to solid 1-D nanostructures⁹⁸. Nanostructures have been used in a variety of applications from energy conversion to energy storage^{38, 39, 99-101}. Porosity in single crystal nanowires could be useful for alloying with other elements toward creating mixed metal oxide nanowires for influencing selectivity in chemical catalysis. The advantages of porous nanowires include large surface area, surface modifications, and nanostructured pores. This chapter covers synthesis of porous nanowires for metal oxides such as tin oxide, titanium dioxide and alumina oxide NWs with higher surface areas compared to their respective solid nanowires. Also, the mechanism involved in the pore formation and the porosity control with calcination temperature is discussed.

4.1 Review of synthesis methods for porous tin oxide nanowires

Porous tin oxide nanowires with higher surface to volume ratios are used in lithium-ion batteries, solar cells, sensors, optical devices, and electronic devices^{102, 103}. Up to date, several approaches has been used to prepare porous tin oxide nanowires such as chemical etching, hydrothermal method, electro spinning and gas solid reactions¹⁰⁴⁻¹⁰⁶. Template methods include hard and soft template methods^{107, 108}. The following table describes the methods used for the synthesis of porous tin oxide nanowires in literature. All these methods are limited to gram scale materials and are difficult for scale up.

Table 4.1 Review on the porous tin oxide nanowires synthesis methods

Type of nanowires	Method used to create pores in the nanowires	Reference article
Porous SnO ₂ nanowires	<p>Hydrothermal method</p> <ul style="list-style-type: none"> Nanowire with precursor of SnC₂O₄.2H₂O is calcined to get porous nanowires. During the calcination of nanowire precursor SnC₂O₄.2H₂O undergoes simultaneous dehydration and decomposition, with the release of water vapor, CO₂, and CO which is responsible for formation of high density of pores. 	<ul style="list-style-type: none"> Xia et al., 2003 J. Am. Chem.Soc. 125, 16176. 104
Porous SnO ₂ nanowires	<p>Hard template-assisted approach</p> <ul style="list-style-type: none"> Meso porous SnO₂ synthesized through structure replication of ordered meso porous KIT-6 silica (nano casting) Template is removed later by wet chemical etching to get porous nanowires 	<ul style="list-style-type: none"> Tiemann et al., 2010 sensors and actuators, 788-793¹⁰⁹.
Porous SnO ₂ nanotubes	<p>Hard template assisted method</p> <ul style="list-style-type: none"> One-dimensional (1D) silica meso structures as effective sacrificial templates to synthesize SnO₂. template is removed by hydrothermal method SnO₂ nano crystallites are deposited on meso structures of silica Dissolution of silica by base media to get nano structures of tin oxide 	<ul style="list-style-type: none"> Qi et al., 2009, Small, 6: 296–306¹¹⁰.
Porous SnO ₂ microfibers, nano bundles	<p>Solution based precipitation method</p> <ul style="list-style-type: none"> Tin oxalate (SnC₂O₄) precursor is used to produce nano structures Pores were created in the primary nano particles due to the removal of organic species by the annealing of SnC₂O₄. 	<ul style="list-style-type: none"> Wang et al., 2011. Nano Micro letters 3(1) 34-42¹⁰⁵.

<p>Porous SnO₂ nano tubes</p>	<p>Template assisted method</p> <ul style="list-style-type: none"> • Used carbon nanotubes as template to create porous NWs • As-prepared wet SnO₂/CNT nanocomposites were coated on the surface of the ceramic substrate • Surface of the CNTs was coated with uniform and dense SnO₂ nanoparticles • After removing the CNTs by thermal treatment the SnO₂ particles were assembled and formed porous SnO₂ nanotubes. 	<ul style="list-style-type: none"> • Liu et al., J. Phys. Chem. C 2009, 113, 9581–9587¹⁰⁸
<p>Porous SnO₂ nanowires</p>	<p>Template assisted method</p> <ul style="list-style-type: none"> • Using self-organized, highly porous anodic alumina templates • AC electro deposition of electrolyte precursor solution SnCl₂.H₂O on anodic alumina templates • Removal of tin nanowires from templates by etching templates in NaOH or cracking the templates and separating the templates by sonication then oxidizing them in air gives the tin oxide porous nanowires 	<ul style="list-style-type: none"> • Moskovits et al., Adv Mater, 2003, 15¹⁰⁶.
<p>Porous SnO₂ nanowires</p>	<p>Reactive-template method</p> <ul style="list-style-type: none"> • Used MnO₂ nano rods as the sacrificial template • Reductive nature of Sn²⁺ and oxidative nature of MnO₂ in an acidic environment is used to dissolve the MnO₂ nanorods. $\text{MnO}_2 + \text{Sn}^{2+} + 2\text{H}_2\text{O} \rightarrow \text{Mn}^{2+} + \text{Sn(OH)}_4$ • MnO₂ nano rods are completely dissolved by reduction, eventually Sn(OH)₄ nanotubes with a hollow interior is formed. • Finally, porous nanowires obtained by calcination at 500 °C according to the reaction $\text{Sn(OH)}_4 \rightarrow \text{SnO}_2 \cdot x\text{H}_2\text{O} + (2 - x)\text{H}_2\text{O}$ $\text{SnO}_2 \cdot x\text{H}_2\text{O} \rightarrow \text{SnO}_2 + 2\text{H}_2\text{O}$ 	<ul style="list-style-type: none"> • Bingqiang et al., Appl. Mater. Interfaces 2013 5, 7893–7898¹⁰⁷.

4.2 Solvo plasma method for synthesis of porous tin oxide nanowires

The solvo plasma oxidation method is based on the atmospheric plasma oxidation of metals or metal oxides in the presence of alkali reagent for producing metal oxide nanowires and porous metal oxides. Plasma oxidation allows for ultrafast timescales (on the order of a few tens of seconds) compared to conventional hydrothermal method. Also, hydrothermal methods utilize large quantity of water and oxidation time scales on the order of several hours. The solvo-plasma oxidation method has been demonstrated with the synthesis of TiO_2 , MoO_x and WO_3 nanowires as oxides of high melting point metals and the tin oxide, zinc oxide as oxides of low melting point metals. The reaction time scales are on the order of a minute or less. The experimental observations suggest that one-dimensional growth occurs due to basal growth of nuclei during oxidation of molten metal alloys with alkali metals¹¹¹.

SnO_2 nanowires were synthesized using a plasma-based synthesis technique as discussed in our previous report³⁸. In brief, bulk SnO_2 powder (1-5) μm size (purchased from Atlantic equipment engineer, Inc.) is mixed with potassium hydroxide (Sigma Aldrich) in a 3:1 weight ratio. A thick paste is prepared by using a small amount of distilled water. Small amount of the prepared paste was uniformly coated on a quartz substrate (thickness $\sim 100 \mu\text{m}$). The quartz substrate with SnO_2 paste was exposed to an atmospheric plasma for 2 minutes. The experimental conditions used in the solvo-plasma method are argon, air flowrates with 2 L min^{-1} and 10 L min^{-1} , respectively. The flowrates were kept constant throughout the experiments. The solvo-plasma process operating at a plasma power of around 1 kW. After the reaction, the resulting thick SnO_2 film was scraped from the quartz substrate with a razor. The collected materials were suspended in 100 mL of deionized water and sonicated for 1 h. After the sonication, the resultant mixture was

transferred to a centrifuge tube, leaving behind the unsuspending larger particles. The particle suspension was spun in the centrifuge for 1 h at 7000 rpm. The precipitate was separated and dried at 80 °C to get the as-synthesized potassium-rich (~7 wt%) tin oxide nanowires.

Porous tin oxide nanowires are synthesized by using the as synthesized potassium stannate nanowires. They were first immersed in 0.1 M HCl solution for 1 h. Under the etching step, the potassium ion from potassium stannate were ion exchanged with the hydrogen ion in the crystal lattice. The HCl-treated samples were washed with DI water and dried at 80 °C. Finally, the dried powder was calcined at 500 °C in air for 5 h.

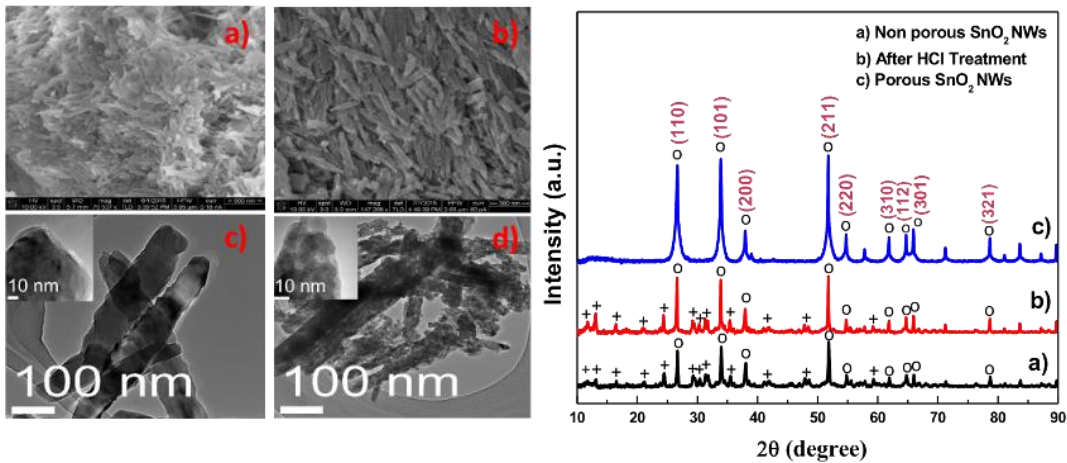


Figure 4.1. SEM image analysis, TEM image analysis, X-ray diffraction analysis of as synthesized and porous tin oxide nanowires

The morphology of as-synthesized SnO₂ NWs and porous tin oxide NWs were analyzed by using the SEM and TEM image analysis. As shown in Figure 4.1, the dimensions of porous tin oxide NWs were measured approximately, 1-2 μm in length and 80-200 nm in diameter. Figure 4.1c shows a characteristic TEM image of the SnO₂ nanowires synthesized using solvo-plasma oxidation technique. The morphology of the as-synthesized nanowires contains no observable structural defects even at the nanoscale

(Figure. 4.1c inset). After the etch treatment and calcination steps the morphology of tin oxide nanowires is still maintained (Figure 4.1d). Possibly, the defects are introduced between the atoms due to the following processes. In the acid etch treatment, the exchange of the potassium ions with hydrogen ions occurs. Also, tin oxide is a much denser phase compared to hydrogen stannate. So, during the calcination step, the phase transformation through the loss of water led to generation of voids or pores inside the lattice. See the high-resolution TEM image (Figure. 4.2a).

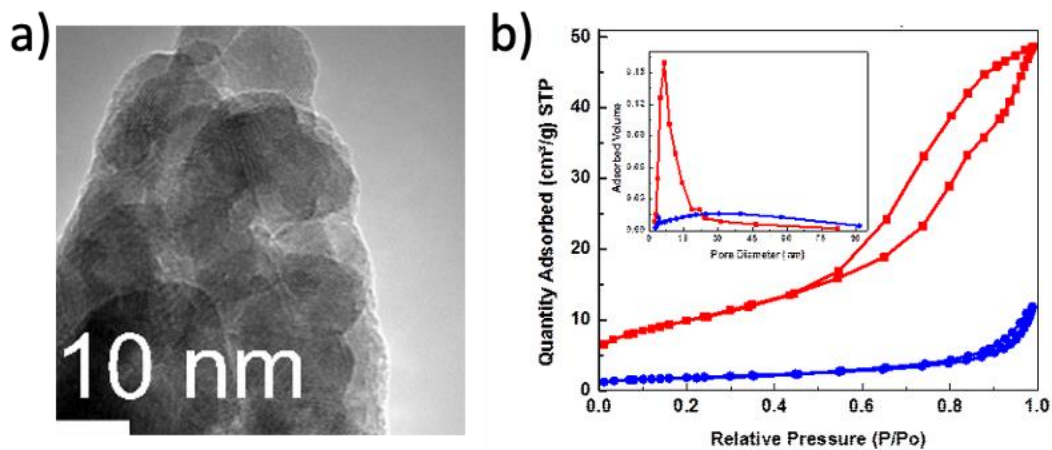


Figure 4.2. a) TEM image analysis of porous tin oxide NWs b) Brunauer–Emmett–Teller (BET) analysis of tin oxide nanowires before and after the acid wash treatment.

Nitrogen adsorption-desorption isotherm of SnO₂ porous NWs and as-synthesized SnO₂ nanowires was obtained, and the surface area of the samples were calculated by using the Brunauer–Emmett–Teller (BET) method. They showed a type-IV isotherm with a hysteresis loop in the relative pressure range of 0 to 1, this indicates the presence of mesopores in the porous tin oxide nanowires. The BET specific surface area measured for porous NWS was 35.0 m² g⁻¹ and for as-synthesized tin oxide NWs was 5.7 m² g⁻¹. The specific surface area of porous NWs was increased by 5-6 times the original surface area. Also, Barrett-Joyner-Halenda (BJH) pore size distribution is shown in the inset Figure 4.2.

The average pore diameter obtained is about 7 nm. The value of pore diameter is correlates with the model of type IV isotherm.

4.3 Synthesis of porous titania nanowires

Titania NWs find wide-spread applications because of their superior properties such as low toxicity, environmental safety, chemical stability, favorable mechanical properties, large band gap (3.2 eV) and high refractive index. With the increasing search for renewable sources as alternative routes of energy to meet growing demands, development of TiO₂ based devices grown on the account of the Ti being the 9th most abundant metal in earth crust (0.57%). Porous titania nanowires with diameters ranging from 100-200 nm and length of 4-6 μm are synthesized using the solvo plasma technique as shown in Figure 4.3. The advantages of porous nanowire structure also include large surface area (30-40 m^2/g) measured using the BET surface area analysis; nanostructured pores provide good windows to anchor active metal nanoparticles in the pores. This would potentially improve the number of the active sites and the catalyst activity. As synthesized nanowires can be made porous to improve surface area to $\sim 40\text{-}50 \text{ m}^2/\text{g}$ from $5\text{-}7 \text{ m}^2/\text{g}$ baseline value by alloying with alkali metals precursors first and removing them subsequently by 1M HCl treatment.

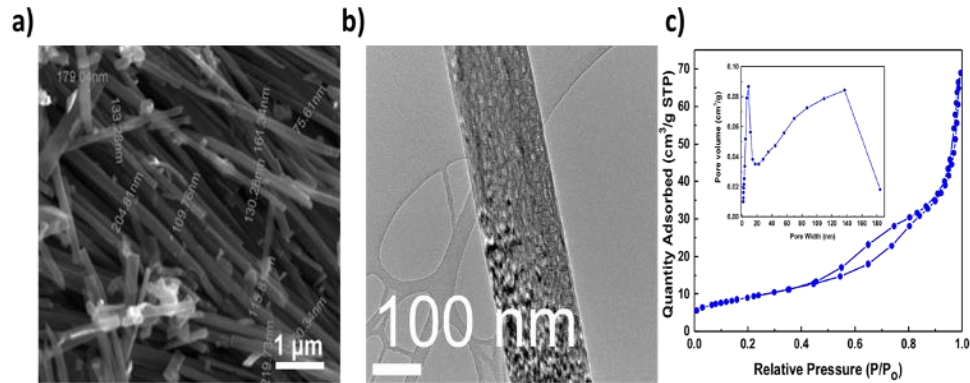
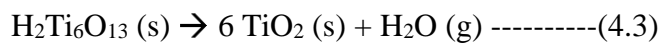
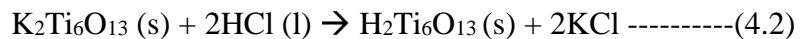
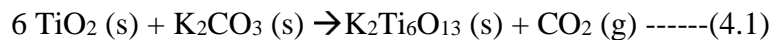


Figure 4.3. a) Scanning electron microscopy image analysis of porous titania NWs b) Hi resolution TEM image analysis of porous titania NWs, and c) BET surface area analysis of porous titania NWs

The potassium titanate ($K_2Ti_6O_{13}$ (s)) nanowires synthesized by the solvo plasma method undergoes the following reaction mechanisms from equation 4.1 to equation 4.3. Porous TiO_2 NWs can be produced via a simple treatment by immersing $K_2Ti_6O_{13}$ NWs powder in 1M HCl solution for 1 h to etch the potassium-rich titanium oxide nanowires. In the etching step, many of the K atoms are ion changed with hydrogen atom may cause the dislocations or defects throughout nanowires.



Porosity can be controlled from equation 3 by adjusting the calcination temperature of the reaction. A range of 450-600 deg C temperatures were used to obtain the higher surface area nanowires. As shown in Figure 4.4, the highest surface area obtained is about $43.5 \text{ m}^2/\text{g}$ at a temperature of 450 deg C in comparison to the starting material has only the surface area of $5\text{-}6 \text{ m}^2/\text{g}$.

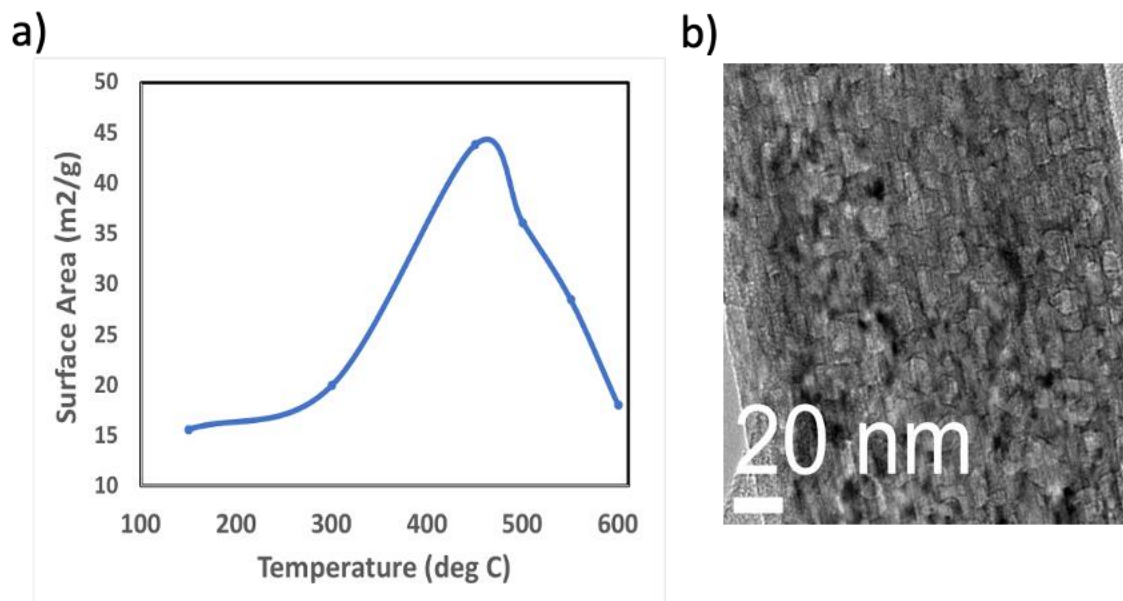


Figure 4.4. Experimental data showing the a) Surface area control in the porous titania nanowires with the change in the calcination temperature b) Hi resolution TEM image analysis of porous titania NWs

It is observed that the surface area is gradually reduced with the increase in the calcination temperature. To understand the decrease in the surface area of titania NWs with the increase in calcination temperature, the samples were characterized with X-ray diffraction analysis and SEM image analysis. As shown in Figure 4.5, from X-ray diffraction analysis for samples with the increase in calcination temperature indicate the gradual phase transformation of titania anatase phase to rutile phase. Also, SEM image analysis shows the porous NWs modification to solid titania nanowires at higher calcination temperature. The decrease in surface area of titania NWs could be related to the phase transformation and structural rearrangement of titania NWs crystal lattice at higher calcination temperatures.

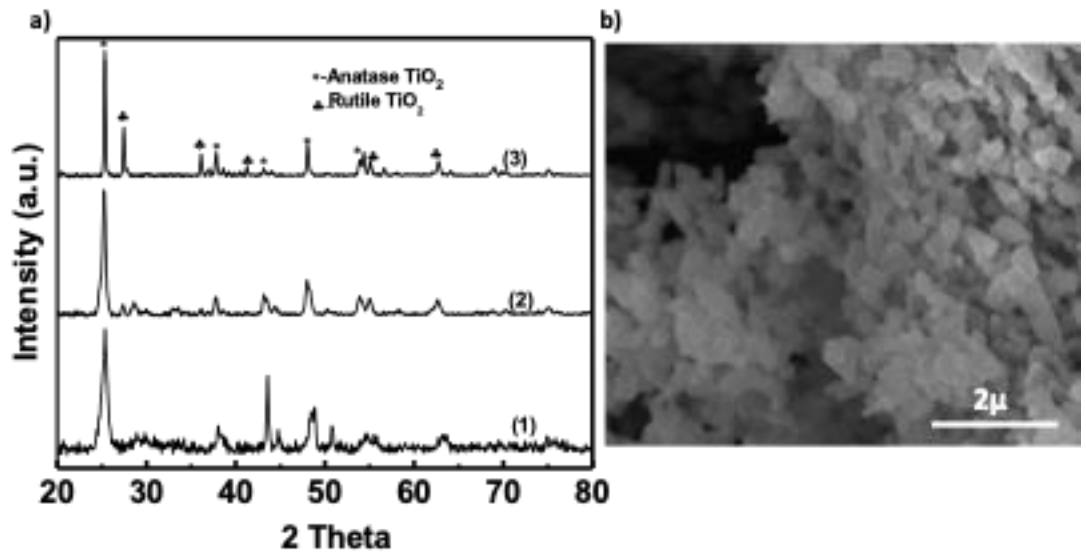


Figure 4.5. Experimental data of a) Calcined porous titania NWs X-ray diffraction analysis at different temperatures (1) at 450 deg C for 2 h (2) 600 deg C for 2h (3) 800 deg C for 6 h b) SEM image analysis of calcined porous titania nanowires at 800 deg C for 6 h.

In-situ TEM analysis on the hydrogen titanate nanowires

In situ TEM heating experiments were also conducted to understand the pore formation mechanism and to identify the temperature of the pore formation. This experiment was carried out on the synthesized hydrogen titanate nanowires. The measurements are collected at a different temperature of 25 deg C, 200 deg C, 400 deg C and 470 deg C. The nanowires were diligently analyzed for any surface modifications. It was observed that the morphology of HTO (hydrogen titanium oxide) nanowires remained like the pristine nanowire form. However, at a temperature of 400 deg C, the surface started to form the brighter spots should be related to formation of pores. The pores were clearly visible at a temperature 470 deg C as shown in Figure 4.5e. This temperature of pore formation is closer to the synthesis temperature of high surface area nanowire experimental data.

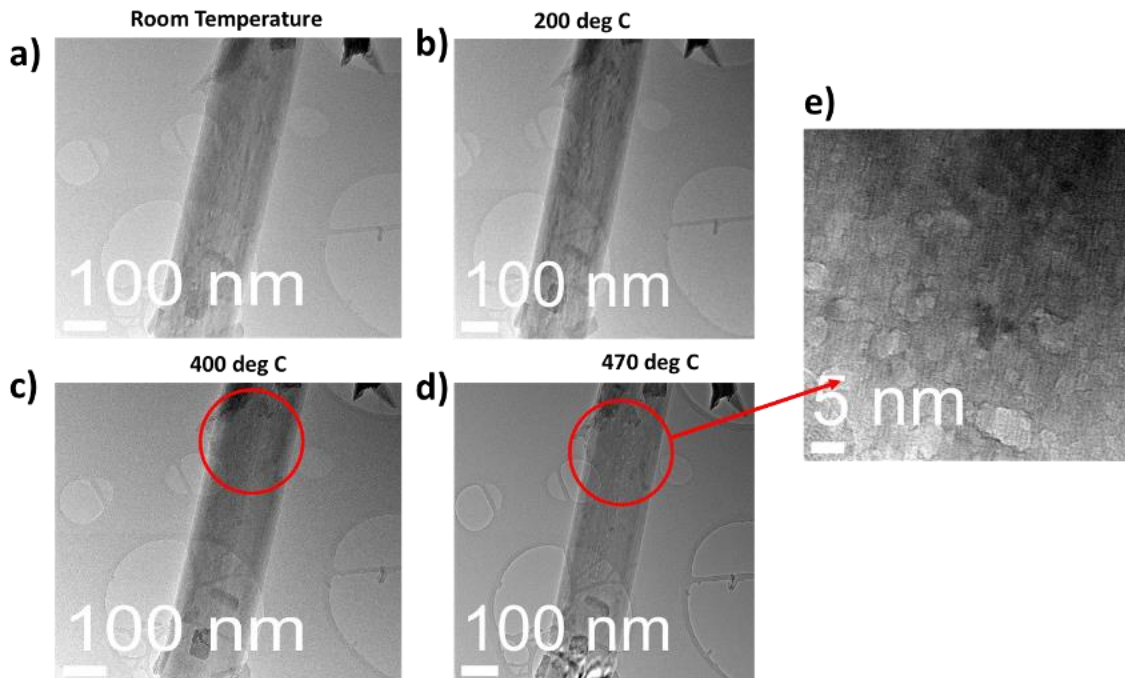
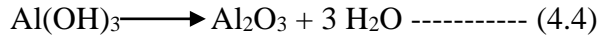


Figure 4.5. In-situ TEM experimental data on the hydrogen titanate nanowires collected at heating temperatures of a) 25 deg C b) at 200 deg C c) at 400 deg C d) at 470 deg C e) at higher magnification and 470 deg C

4.4 Synthesis of porous alumina nanowires

Porous alumina nanowires with high surface area have been synthesized by using a wet chemical method. High surface area alumina nanowires could be used as catalyst support to anchor the active metals on the support, thus anchoring the support material and preventing the sintering of particles during the high temperature catalysis reactions. Also, alumina NWs provides the optimal acid-base sites needed for the higher activity of the catalyst. The synthesis process of alumina nanowires is as follows: aluminum metal powder is slowly mixed with 0.5 M potassium hydroxide/potassium carbonate and P_H of the solution measured is about 11-13. The temperature solution is maintained around 100 deg C by using the hot plate. The aluminum metal is added slowly to the beaker as the reaction is exothermic and liberates lot of heat during the reaction. This reaction took place in about

6-7 h to yield the mixed phases of potassium alumina nanowires and aluminum hydroxide nanowires. Furthermore, potassium aluminate nanowires are water washed and acid treated in concentration of 0.1 M HCl to transform into the aluminum hydroxide nanowires. Furthermore, thermal decomposition of alumina hydroxide nanowires at a temperature of 650 deg C to form the γ -Alumina nanowires as observed in reaction (4.4).



As shown in Figure 4.6, X-ray diffraction analysis confirms the transformation of potassium alumina nanowires to aluminum hydroxide nanowires and the formation of gamma alumina nanowires from the aluminum hydroxide nanowires. The porous alumina NWs formation involves the following steps, first step is to conversion of all the as synthesized alumina NWs into the alumina hydroxide nanowires by the ion exchange of potassium ions with the hydrogen ions. Second step involves the calcination of the converted alumina hydroxide nanowires to form the γ -alumina nanowires. The high porosity of the nanowires could be a result of phase transformation and dehydration of water molecules from the alumina hydroxide NWs.

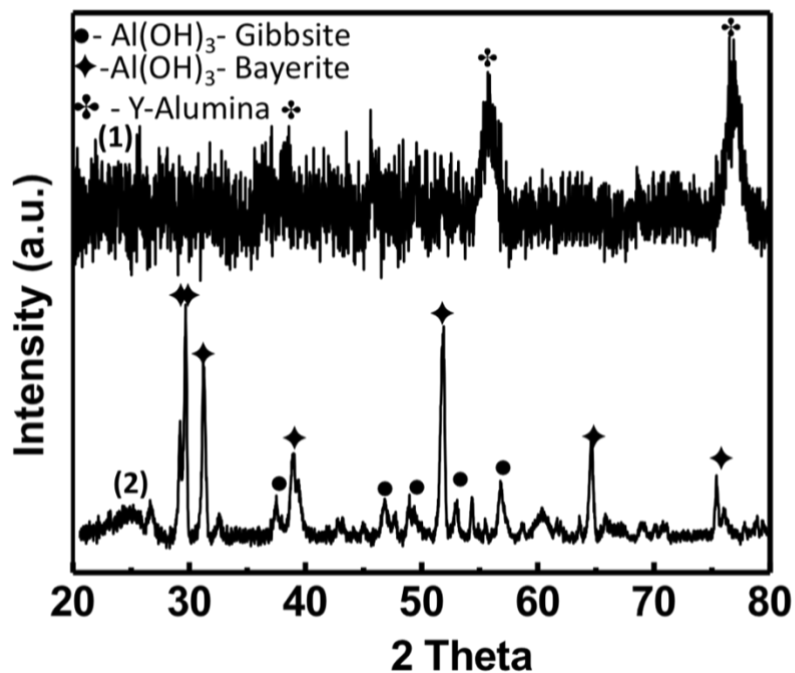


Figure 4.6. X-ray diffraction analysis of alumina NWs (1) After the calcination at 650 deg C (2) Before the calcination

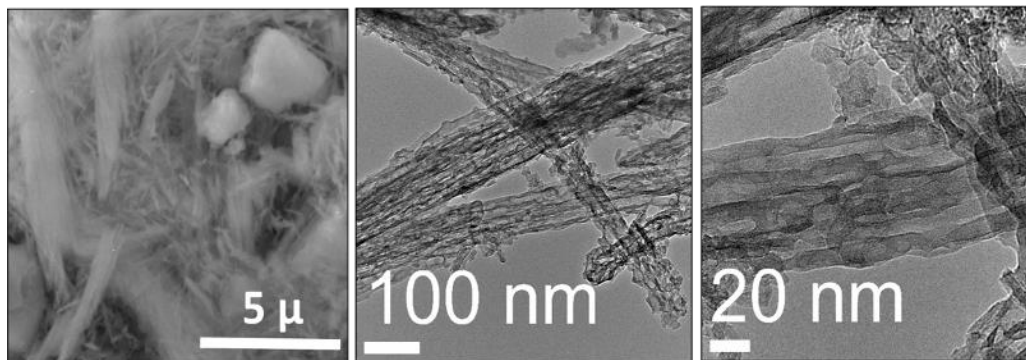


Figure 4.7. Electron microscopy images of porous alumina nanowires: (a) SEM image analysis and (b) & (c) Brightfield TEM image analysis.

Porous nanowires are further characterized by using the SEM and TEM image analysis as shown in Figure 4.7. Alumina nanowires with the diameters of about 20-50nm and length of 500 nm-1μm has been synthesized. TEM image analysis shows that the nanowires are

very thin and contains several micro pores. In addition, BET surface area for porous alumina nanowires is measured for several samples and it is in the range of 160-300 m²/g.

4.5 Mechanism of pore formation in the nanowires

A mechanism is proposed to explain the pore formation in nanowires based on the experimental observations, experimental data analysis and phase transformation. The mechanism is explained with the example system of titania nanowires. A schematic representation of pore formation mechanism is shown in Figure 4.8. Based on the equations (4.5) & (4.6), potassium titanate NWs are ion change with HCl to form the hydrogen titanate NWs. Furthermore, hydrogen titanate NWs are calcined to synthesize the porous titania NWs.

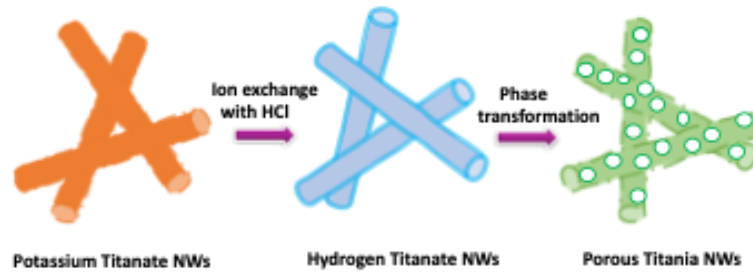
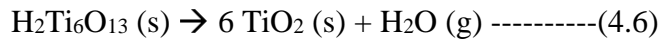
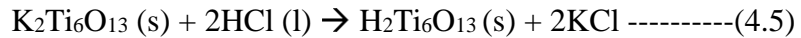


Figure 4.8. Schematic representation of the pore formation mechanism in the titania nanowires



In the ion exchange process step (2), potassium ions in the titanate structure are ion exchange with the hydrogen ions to form the hydrogen titanate. The formation of pores is related to the dehydration of interlayered OH groups in hydrogen titanate. The loss of OH groups may form two types of lattice defects such oxygen vacancy and hydrogen vacancy as reported¹¹². From the principle of charge neutrality and Kroger and vink's symbols, the reaction may be written as follows (equation 4.7)

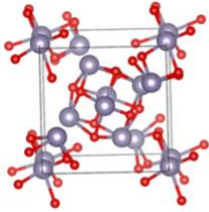
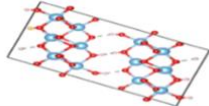
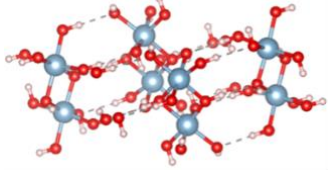
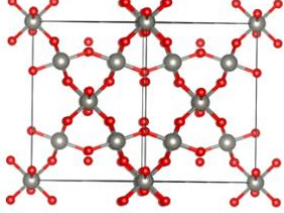


This loss of hydroxy ion and phase transformation lead to the formation of pores in the titania NWs. The lattice defects from oxygen and hydrogen ion could cluster together and the growth of the clusters lead to the formation of pores or voids in the nanowires. Similarly, dehydration of hydroxy ions in the hydrogen stannate and aluminum hydroxide phases lead to the formation of porous nanowires.

Also, it is calculated that material volume changes from hydrogen titanate to titania considerably high because of the density differences and loss of water molecules. This reduction in material volume compensated by the formation of pores in the nanowires during the phase transformation. For example, the molar volume for hydrogen titanate is reduced to 70% compared to the titania NWs molar volume. It is corresponding to a free volume creation of 30%. The free volume formation calculations are also shown for other systems as well (Table 4.2).

Furthermore, in-situ TEM experimental data of hydrogen titanate nanowires indicate that the pore formation appears to start at a calcination temperature of 400 deg C and further increase in temperature lead to the obvious pore formation at a temperature of 470 deg C. This is the similar calcination temperature used to obtain the porous nanowires experimentally and it is also reported that mesoporous transformation of hydrogen titanate occurs around a calcination temperature of 400 deg C¹¹³. Moreover, as shown in Figure 4.4 with the increase in the calcination temperature, the surface area increases up to 450 deg C, and then a decrease in surface area is noticed after the 450 deg C temperature. The decrease in surface area after the temperature of 450 deg C is attributed to the phase transformation of titania (anatase) to titania (rutile) phase.

Table 4.2. Free volume calculations and mesoporous phase transformation temperature for different nanowire systems

NWs material synthesized	Porous NWs BET Surface area measured (m ² /g)	Percentage free volume from solid NWs to porous NWs transformation	Temperature of mesoporous NWs transformation (deg C)	Structure of mesoporous material
Titanium dioxide	36-43	30%	400	
Tin dioxide	35-36	25%	473	
Alumina	150-180	40%	70-80	
Tungsten Oxide	3-6	18%	350	

Alumina NWs system exhibited the high surface area (150-180 m²/g) compared to the other systems. This could be related to the low phase transformation temperature of alumina at 150-180 deg C compared to the other nanowire systems from the Table 4.2. At low phase transformation temperatures, the limited mobility of atoms and vacancies and thus limiting

the growth of vacancy clusters. This leads to the smaller pore formation and smaller diameter nanowires.

4.6 Chapter summary

This chapter discusses the synthesis and mechanism of formation of porous tin oxide, titania nanowires, alumina nanowires. Porous tin oxide and titania nanowires were synthesized by using the solvo plasma method whereas alumina porous nanowires were synthesized by using a simple wet chemical method. The underlying mechanism for the formation of pores in the resulting nanowires is because of ion exchange mechanism and dehydration hydroxides ions followed by the phase transformation into the porous nanowires. In-situ TEM experimental data, XRD data, and BET data support the mechanism of pore formation. It is also observed that the calcination temperature for converting hydrogen titanate to titania is significant in control of surface area of resulting titania nanowires. Furthermore, phase transformation from anatase titania to rutile titania structural rearrangement lead to the lower surface area NWs.

CHAPTER 5 SYNTHESIS OF MIXED METAL OXIDE NANOWIRES VIA SOLID STATE ALLOYING OF SOLUTES WITH BINARY METAL OXIDE NANOWIRES

This chapter presents a generic method for synthesis of mixed metal oxide nanowires using solid-state diffusion of solutes into binary oxide nanowires. The solid-state alloying of metal oxide nanowires is performed using a few liquid and solid phase precursors to produce mixed metal oxide alloy nanowires. Specifically, copper alloying using copper nitrate precursor into the titania nanowires is studied in detail as an example. Several fundamental studies were performed using differential scanning calorimetry. The resulting nanowires are characterized using electron microscopy image analysis, TEM EDX elemental analysis and X-ray diffraction analysis techniques to understand the uniformity in alloying and crystal structure changes in the nanowires. This chapter also covers many other experiments involving solid state alloying of alumina, zinc oxide and titania nanowires with copper, nickel, cobalt, and zirconium containing precursors. Based on the experimental data and thermodynamics, a model is proposed to explain mechanistic aspects of solid-state alloying of solutes in to nanowires.

5.1 Synthesis of alloyed nanowires via solid state alloying

5.1.1 Synthesis of copper alloyed titania nanowires via solid state alloying

Copper alloying experiments with titania nanowires were performed using the following simple procedure. First, titania nanowires were mixed with the copper nitrate precursor dissolved in water. The amount of nitrate precursor was determined based on the amount

of copper alloying desired in nanowires. Several experiments were conducted using different amounts of copper nitrate precursors toward obtaining titania nanowires with composition of copper ranging from 2 at% to 15 at% to that of titania NWs. Second, the precursor materials were dried at 80 deg C for 1h. Finally, the dried materials were exposed under the inert atmosphere at 500 deg C for 1h. Figure 5.1a shows scanning electron microscope images of the TiO₂ NWs before and after alloying with the precursors. SEM images show that nanowire morphology is retained even after the alloying reaction. The average diameters of nanowires ranged from 150 to 200nm and lengths ranged from 1 to 2 microns. So, there were no morphological changes to the alloyed nanowires compared to original titania nanowires. Figure 5.1b shows the X-ray diffraction analysis of alloyed titania NWs. The diffraction peaks correspond to only titania anatase phase in the alloyed nanowires with a nominal composition of 12 at% for copper. There are no other peaks observed indicating that no copper oxide is formed. Furthermore, a slight shift in X-ray diffraction peaks occurred towards higher angles. The observed shift in the X-ray diffraction peaks indicates that the copper is alloyed into the crystal lattice of titania NWs. In this case, lattice contraction of titania NWs could have occurred as the ionic radii of copper atom (0.57 Å) is smaller than that of the titania atom ionic radii (0.605 Å). This might be correlated with the substitutional replacement of Ti⁴⁺ sites with Cu²⁺ ions. As shown in Figure 5.1 e&f, Raman structural analysis is performed on the alloyed titania nanowires. An apparent shift in Raman peaks were seen because of structural changes in the solvent titania phase. Only the spectral bond changes or vibrations from the titania molecules were detected, no secondary phases of copper oxide were observed. The results from the Raman experiment were in consistence with the X-ray diffraction analysis studies.

However, experiments involving molar composition of copper nitrate precursor extended above 12% into the titania yielded the secondary phase of copper oxide along with the titania anatase phase.

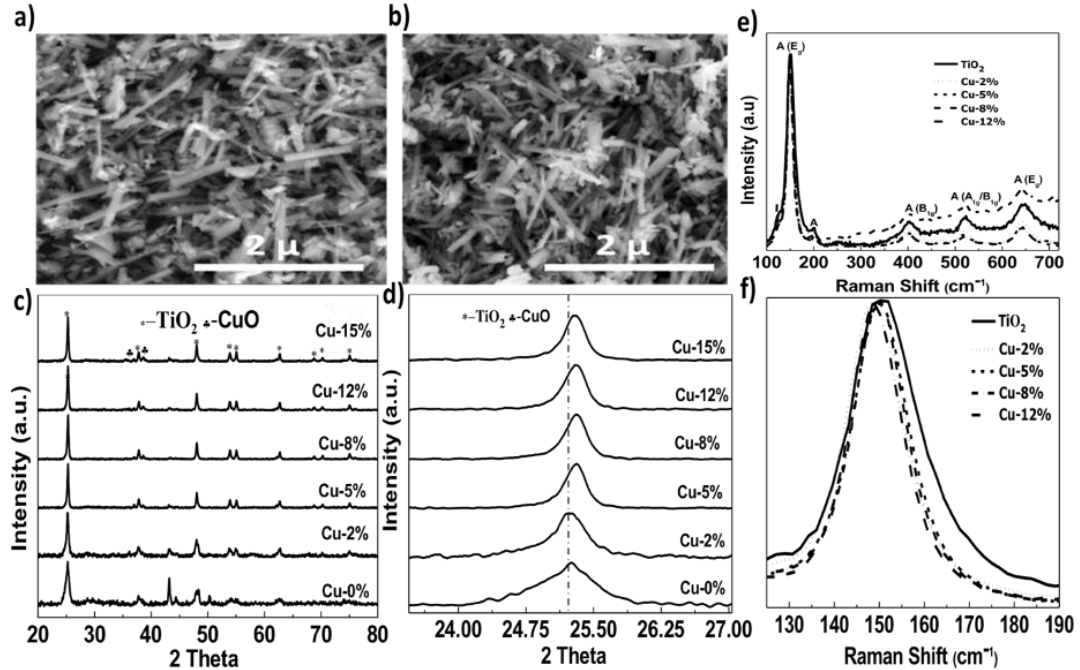


Figure 5.1. SEM image analysis of cu (8 at%) alloyed titania nanowires a) before alloying b) after alloying; c) X-ray diffraction analysis of alloying from 0 at% to 15% of Cu into the titania NWs; d) Peak shift analysis of copper alloyed titania NWs; e) Raman analysis of copper alloyed titania NWs; and f) Raman peak shift analysis of copper alloyed titania NWs.

Furthermore, copper alloying into the titania NWs is verified by using the HRTEM (High resolution transmission electron microscopy). Before the alloying, Figure 5.2a TEM image analysis shows the presence of nano clusters of dried copper nitrate precursor on the nanowire surface. After the alloying, the nanoclusters were appeared to be dissolved into the titania NWs. This is also confirmed with the elemental TEM EDX elemental analysis as shown in Figure 5.2a. The data shows that the nanoclusters of copper on the surface of titania NWs before alloying. Copper precursor layer appeared to be uniformly incorporated into the lattice of titania NWs after the alloying. There were no surface or segregated

particles of copper is seen on the titania NWs. Moreover, as seen in Figure 5.2d TEM EDX line scan profile on a single nanowire shows the straight-line profile of copper concentration after the alloying. This confirms that the copper concentration is uniform along the diameter of NWs. In contrast, TEM EDX elemental line scan profile before the alloying shows the non-uniform distribution of copper as shown in Figure 5.2c. Also, it is measured from the TEM EDX elemental analysis for a nominal composition of 12 at%, an atomic composition of about 8 at% of copper is alloyed into a single titania NW.

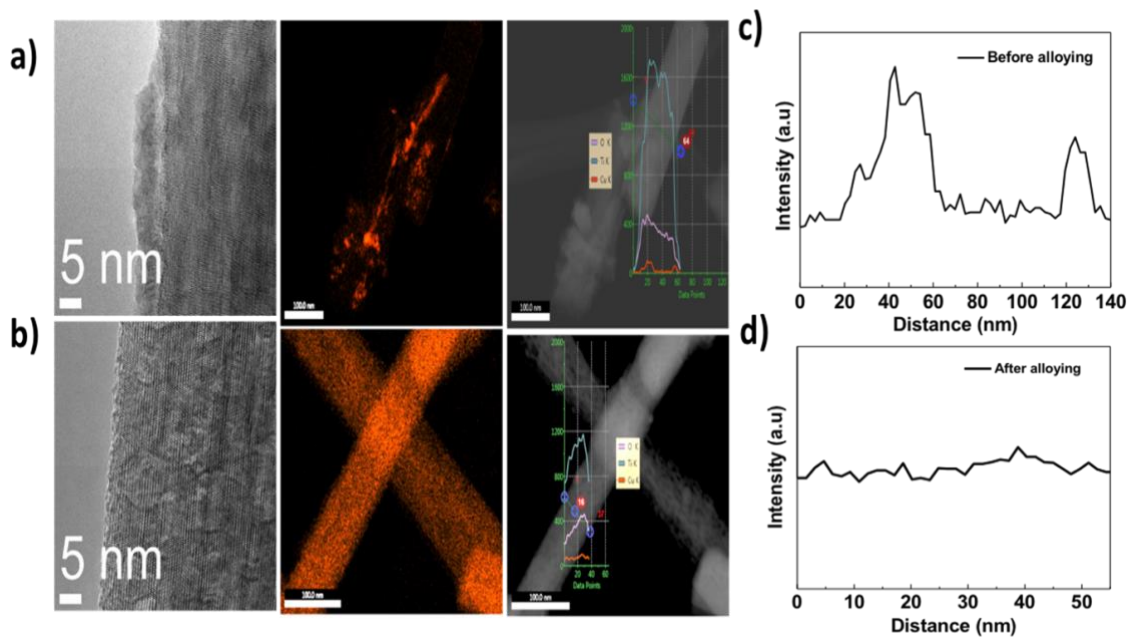


Figure 5.2. TEM image analysis of copper alloyed titania NWs: a) before alloying and b) after alloying. TEM EDX line profile analysis of copper alloyed titania NWs along the diameter of NWs c) before alloying, and d) after alloying

Next, we performed the UV-Vis spectroscopy experiment on copper alloyed titania NWs to understand the changes in the optical spectrum. The light absorption edge of copper alloyed titania NWs was extended from ultraviolet into the visible spectral range of the spectrum. As shown in Figure 5.3d, the shift towards visible spectrum was increased with the higher amount of copper alloying into the titania NWs. The increase in the range of

visible light to be captured to generate the more carriers were useful in the photo catalysis application.

5.1.2 Copper alloying into the titania NWs at a shorter reaction time

To lower the alloying reaction time, the samples were exposed for a short duration of 30 mins in inert atmosphere. As shown in Figure 5.3, TEM EDX elemental analysis confirms that the copper is distributed uniformly along length and diameter of the titania nanowires. There is no segregation of copper on the nanowire surface. This result shows that the solid-state reaction could occur at shorter time under the nanoscale in comparison to the solid-state alloying in bulk materials carried out for several hours to days.

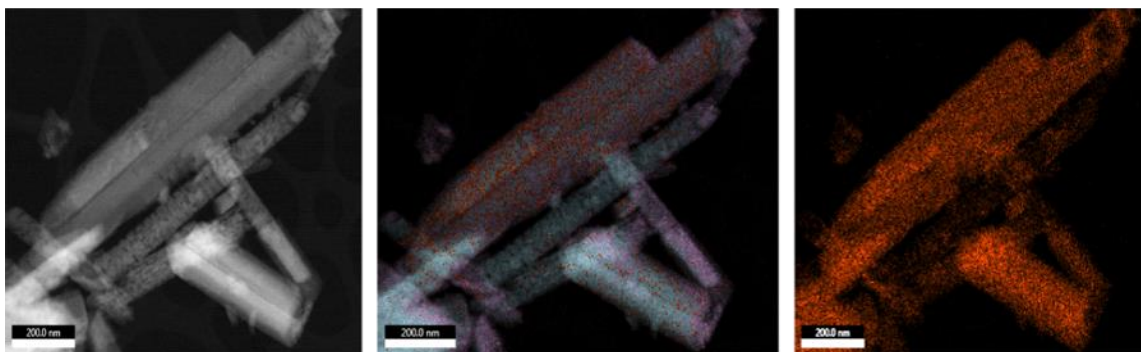


Figure 5.3. TEM EDX elemental analysis of copper (8 at%) alloyed titania NWs in a vacuum furnace

5.1.3 Synthesis of nickel alloyed titania nanowires via solid state alloying method

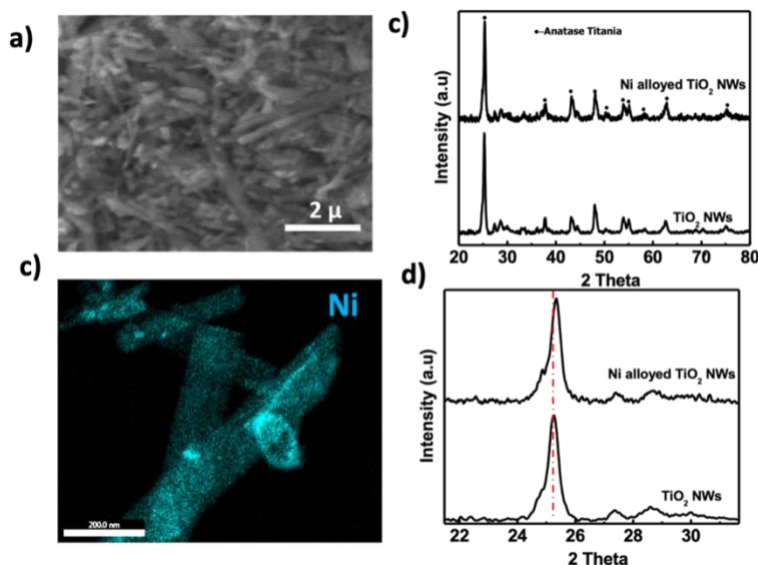


Figure 5.4. Nickel alloying into the titania NWs a) SEM image analysis of nickel alloyed titania NWs; b) TEM EDX elemental analysis of nickel alloyed titania NWs; and c) X-ray diffraction analysis of nickel alloyed titania NWs and titania NWs d) Peak shift analysis of nickel alloyed titania NWs

Here, experiments were conducted to obtain a nominal composition of 8 wt% of nickel into titania NWs. The sample is prepared by mixing the nickel nitrate precursor with titania NWs. Later, the precursor materials were dried at 80 deg C for 1h. The sample was grounded, and solid state alloyed at 500 deg C under the inert atmosphere for 1h. SEM image analysis, X-ray diffraction analysis, and TEM EDX elemental analysis performed to understand the extent of alloying and distribution of nickel in the titania NWs. From the Figure 5.4, SEM image analysis of the titania nanowires alloyed with nickel shows the morphology of nanowires with the lengths are of around 4-6 micron and 150-200 nm in diameter. Also, as shown in Figure 5.5c, TEM EDX elemental analysis on the nickel alloyed sample indicate that the nickel is distributed uniformly throughout titania nanowires. Furthermore, X-ray diffraction analysis reveals that the sample contains the anatase phase of titania as major phase, and no other X-ray diffraction analysis peaks of

nickel oxide are observed. Also, the peak shift towards the right side indicates that the titania lattice is contracted due to the alloying of nickel atoms. This result clearly indicate that the nickel is alloyed into the titania NWs.

5.1.4 Alloying experiments using various metal oxide nanowires and solutes

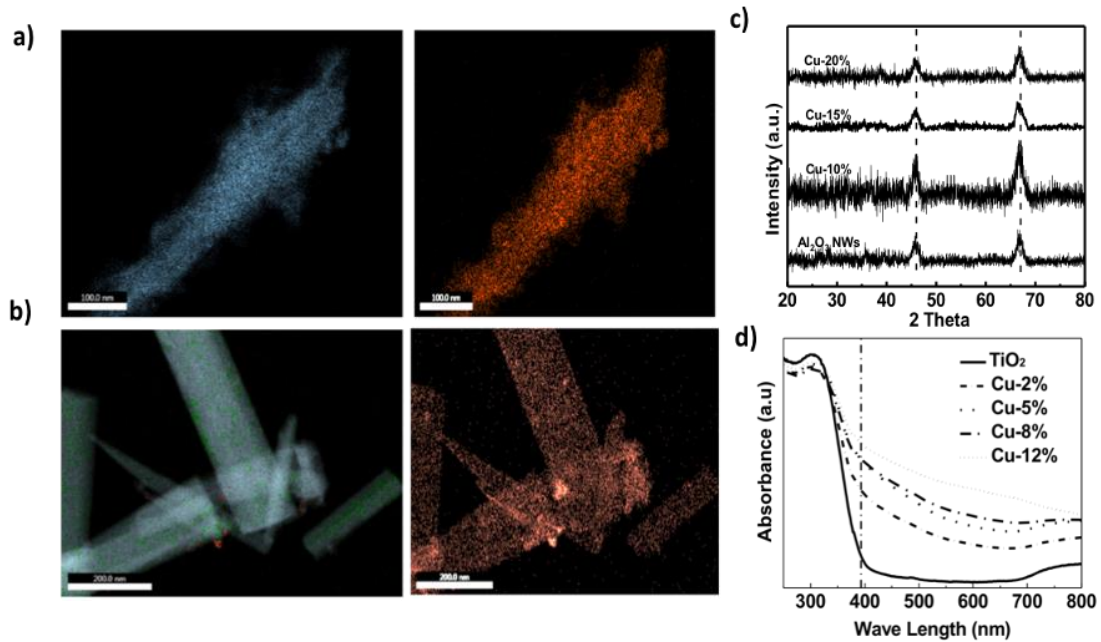


Figure 5.5. TEM EDX elemental analysis of a) copper alloyed alumina NWs (up to 20%) b) Zirconia alloyed titania NWs up to 8% c) X-ray diffraction analysis of copper alloyed alumina NWs d) UV-Vis analysis of copper alloyed titania NWs

To check the applicability of the alloying process to the other nanowire systems, solid state alloying experimental studies performed with titania, alumina and zinc oxide nanowires using various solute precursors. It is reported that the thermodynamic solubility of zirconium into titania is very limited. So, experiments involving zirconium (ionic radii- 0.72 Å) alloying into titania nanowires were performed to understand the solubility at nanoscale. Similarly, experiments were also conducted on solid state alloying of solutes in to zinc oxide nanowires to understand solubilities at nanoscale. Alumina NWs dimensions are relatively smaller in comparison to the titania NWs. So, several experiments on alumina

NWs were conducted to understand the effect of smaller dimensions of nanowires on the thermodynamic solubility limits at smaller nanowire diameters. Figures 5.5a and 5.5b show the images of porous alumina, titania NWs alloyed with the copper precursor, and zirconium nitrate precursor. Porous alumina nanowires were alloyed with copper precursor using a procedure like that described for titania NWs earlier. The resulting alloyed nanowires were characterized using X-ray diffraction analysis and TEM EDX elemental analysis. The results confirmed that the uniform alloying of copper into alumina NWs with no signs of the copper oxide secondary phase formation. Furthermore, copper alloying is extended up to 18 at % in alumina nanowires in comparison to titania nanowires at 8 at%. This could attribute to the reduced dimensions of (diameter of 20-50 nm) of alumina NWs in comparison to the diameter of titania NWs (150-200 nm diameter). TEM EDX elemental analysis on a titania nanowire shows that it is alloyed with zirconium alloyed up to 8 at%. It is reported that the zirconium thermodynamic solubility in titania very low. Zirconia is thermodynamically soluble up to 5 at% in titania at 1700 deg C from the thermodynamic phase diagrams¹¹⁴. Also, ex-situ alloying of zirconia using thin uniform coating of zirconium around titania nanowires were attempted in the literature and only a trace amount of zirconia is found to be alloyed into the titania NWs²⁰. Moreover, the thermodynamic phase diagrams of CuO-TiO₂ and CuO-Al₂O₃ systems at 500 deg C indicate non-existence of solid solutions^{115, 116}. So, the results obtained here clearly show an extended solubility in nanowires than that of bulk materials. This could be attributed to the available higher surface energy at the nanowire surface. Higher surface energy of nanoscale surfaces promotes alloying with solutes. Increased concentration of solutes at surfaces leads to diffusion of solutes into bulk of the nanowires. As the length scales between pores are as

small as few nanometers, the surface alloying leads to re-distribution of solute uniformly into nanowires. The net effect is that the increased surface energy of nanowires leads to increased dissolution of solutes into nanowires.

5.1.5 Synthesis of cobalt alloyed zinc oxide nanowires via solid state alloying

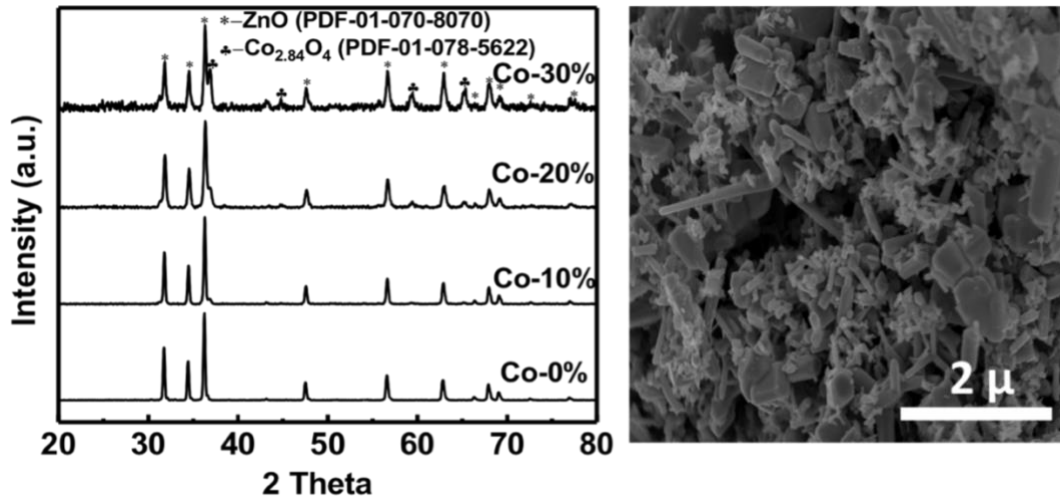


Figure 5.6. Alloying of cobalt into the zinc oxide nanowires a) X-ray diffraction analysis of zno nws alloyed with cobalt nitrate precursor b) SEM image analysis of zinc oxide nanowires alloyed with the cobalt precursor

In the Figure 5.6, solid state alloying of cobalt into the zinc oxide nanowires was carried out using the cobalt nitrate precursor and zinc oxide nanowires as the solvent phase. The experiment was conducted at a temperature of 500 deg C for 1h under the inert atmosphere. From the X-ray diffraction analysis, it is noticed that the cobalt is alloyed upto the nominal composition of 20 at% cobalt nitrate; beyond that composition there is a segregation of cobalt oxide observed. SEM image analysis shows that the nanowire morphology still retained after the alloying process. Higher amount of alloying of up to 20 at% of cobalt into the zinc nanowires seems possible. Such high concentrations are probably due to higher thermodynamic solubility limit expected for cobalt in the zinc oxide at nanoscale.

5.2 Differential scanning calorimetric studies of copper alloying with titania nanowires

Furthermore, differential scanning calorimetry (DSC) tests were conducted at different heating rates using the 8 at% of copper precursors coated on titania NWs. This data is used to understand the alloying temperature of the copper alloyed titania NWs. Figure 5.7a shows the thermograms at different heating rates of (2, 5, 7.5 and 10 deg/min). In the thermogram, endothermic peak corresponds to a temperature of 179.3 deg C shifted to the lower temperatures as the heating rate is decreased. The shifting of endothermic peak could correspond to reaching thermal equilibrium at lower heating rates. Figure 5.7d shows the decomposition of the precursor at a heating rate of 10 deg/min, endothermic peaks at around 130 deg C corresponds to chemically bonded water evaporation and at a temperature 270 deg C for the decomposition of copper nitrate into the oxides of copper, nitrous oxide, oxygen as reaction products. DSC experiments were also performed in different gas environments of nitrogen and air as shown in Figure 5.6b. Sample exposed under atmospheric pressure showed thermogram peaks closer to the copper nitrate decomposition temperature of 248 deg C. Whereas, the sample exposed under nitrogen environment showed the different endothermic peak at 179.2 deg C. This result may indicate that alloying under oxygen lean atmosphere is occurring at a lower temperature than the decomposition temperature of precursor. Furthermore, similar DSC tests were conducted on bulk titania samples under nitrogen atmosphere to understand why copper was not alloying into bulk materials. Interestingly, from Figure 5.6c endothermic peaks correspond to bulk titania sample showed around 261 deg C closer to the decomposition temperature of copper nitrate precursor. These results indirectly correlate with the segregated phase formation of bulk titania and copper oxide and the effect of partial

pressure of oxygen in the environment. Based on the above experiments, two types of reactions are inferred: decomposition reaction at around 250-260 deg C and alloying reaction at around 180 deg C.

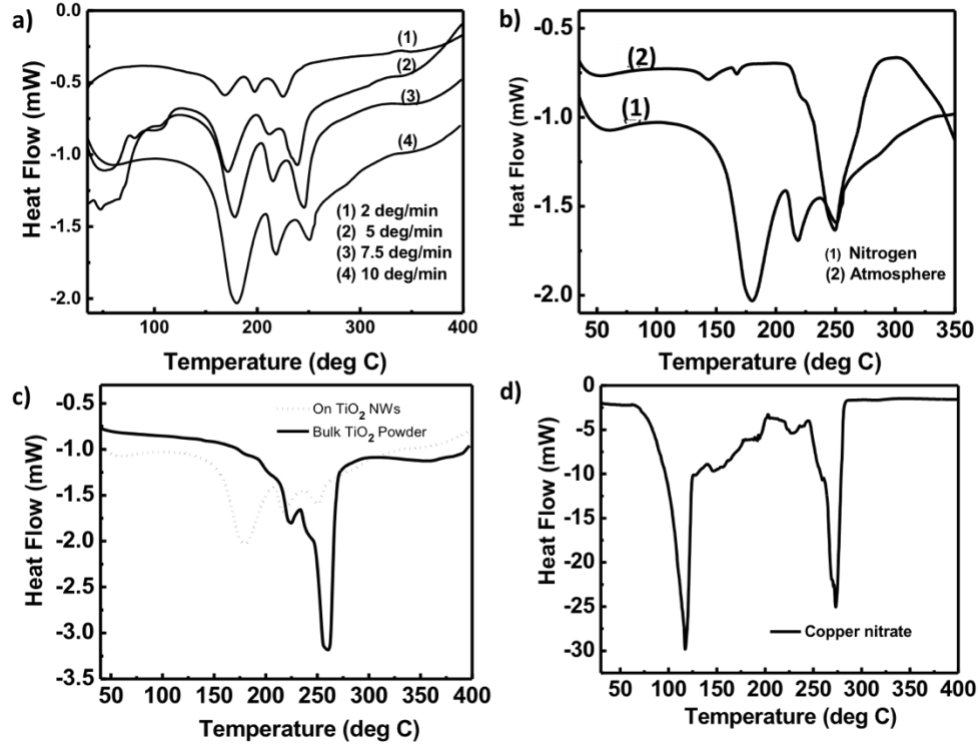


Figure 5.7. DSC analysis of copper alloyed titania NWs a) with different heating rates; b) with in different atmospheres; c) copper nitrate loaded (12 at%) TiO₂ NWs and TiO₂ bulk powder; and d) on copper nitrate precursor

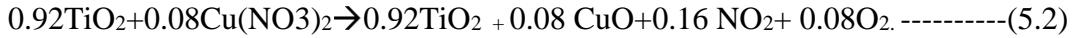
Gibbs free energy is calculated as a function of temperature on the copper nitrate decomposition reaction and copper nitrate alloying reaction of with the titania NWs. The Gibbs free energy values for reactions 5.1 and 5.2 are shown in Figure 5.8. Here, for the Gibbs free energy calculations, it is assumed that the alloyed copper titania phase has the similar Gibbs free formation energy that of composite mixture of titania and copper oxide. The decomposition reaction reaches the negative values of Gibbs free energy at about 227 deg C and alloying reaction reaches negative value at about 135 deg C. This observation

indicates that the alloying reaction is favorable at lower temperature than the decomposition reaction. This result is consistent with the DSC data analysis as well.

Decomposition reaction: Copper nitrate decomposition is given as



Alloying reaction: Precursor alloying reaction with the titania NWs



$$\Delta G_{\text{Decomposition rxn}} = G_{f,\text{CuO}}^0 + 2 * G_{f,\text{NO}_2}^0 + 0.5 G_{f,\text{O}_2}^0 - G_{f,\text{Cu(NO}_3)_2}^0$$

$$\Delta G_{\text{Alloying rxn}} = 0.08 * G_{f,\text{CuO}}^0 + 0.16 * G_{f,\text{NO}_2}^0 + 0.08 * G_{f,\text{O}_2}^0 - 0.08 * G_{f,\text{Cu(NO}_3)_2}^0$$

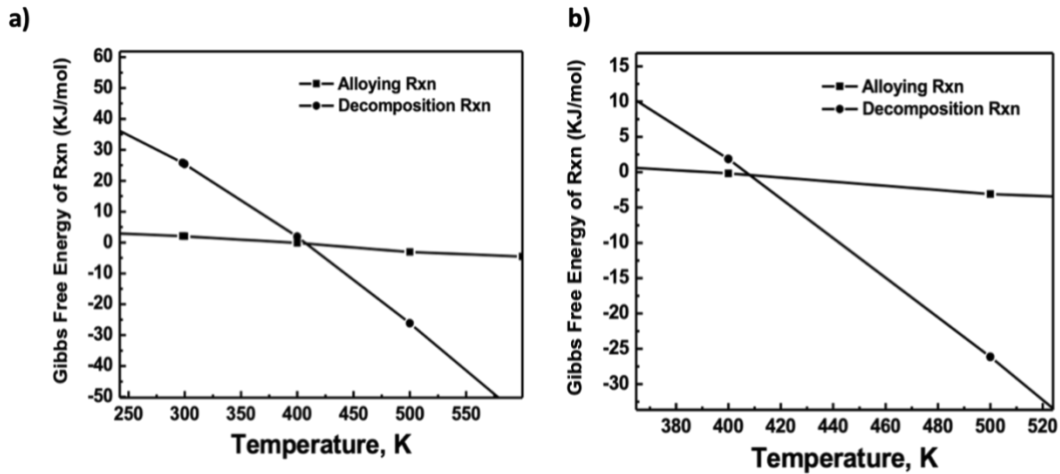


Figure 5.8. a) Gibbs free energy calculated as a function of increase in temperature b) Inset of 5.8 (a)

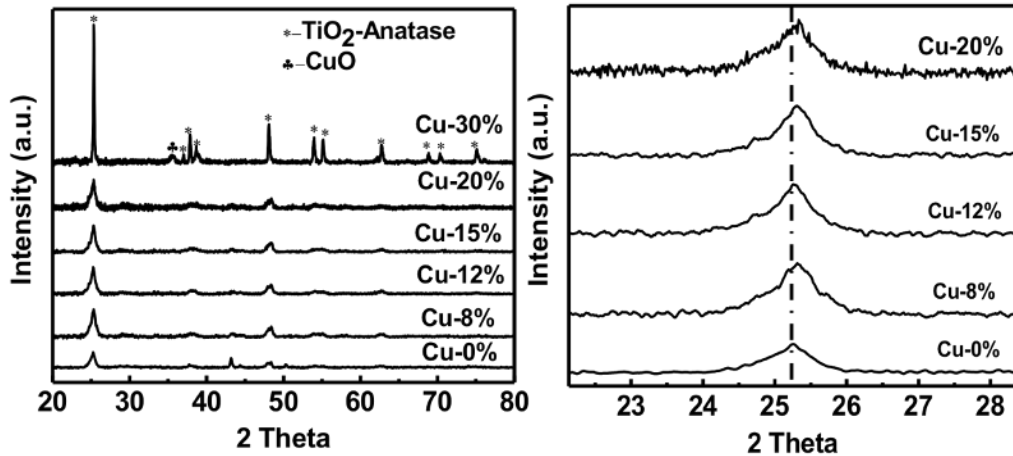


Figure 5.9. X-ray diffraction analysis of copper alloying in titania NWs at a temperature lower than the decomposition temperature (at around 190 deg C)

Furthermore, alloying experiments were carried out at lower temperature than the decomposition temperature of 225-250 deg C. From Figure 5.9, X-ray diffraction analysis performed on alloyed samples synthesized at 190 deg C. The samples showed uniform alloying up to the composition of 20 at% precursor. This further confirms that the alloying reaction takes place at a temperature lower than the decomposition temperature.

Kissinger plot to determine the kinetic parameters K, Ea

From the DSC data of Figure 5.6a, the peak temperatures are obtained at different heating rates and plotted as shown in Figure 5.10.

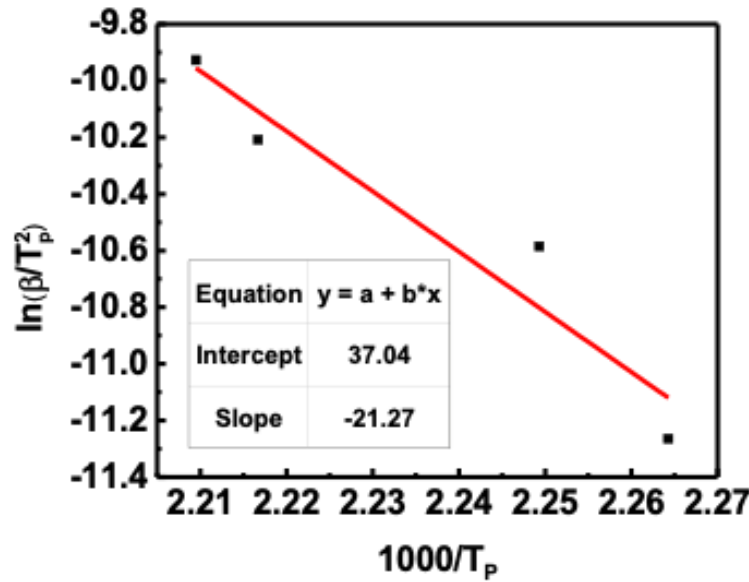


Figure 5.10. Kissinger plot obtained from the data using the DSC experimental technique to determine the kinetic parameters of the reaction

where T_p is the peak temperature of the DSC curve

$$\frac{d}{dt} \left(\frac{d\alpha}{dt} \right) = A * \exp\left(-\frac{E_a}{RT}\right) * \frac{E_a}{RT^2} (1 - \alpha)^n \frac{dT}{dt} - n(1 - \alpha)^{n-1} A * \exp\left(-\frac{E_a}{RT}\right) \frac{(d\alpha)}{dt} = 0$$

Here beta is $\frac{dT}{dt}$, assuming the first order reaction and at constant heating ramp rate. By using the slope and intercept of the equation (5.3), kinetic parameters A, Ea are determined from the above plot.

$$\ln\left(\frac{\beta}{T_p^2}\right) = \ln\left(\frac{A R}{E_a}\right) - \frac{E_a}{R T_p} \quad \text{----- (5.3)}$$

By using the equation $k=A*\exp(-E_a/R*T)$ the value of K is determined, at equilibrium the value of Gibbs Free energy of alloying reaction is determined by using the following equation

$$\Delta G_0 = R * T * \ln(K)$$

Table 5.1. Values of kinetic parameters evaluated from the DSC data

Value of activation Energy (E _a)	176.45 KJ/mol
Pre exponential factor (A)	2.563*10 ²⁰
Rate Constant (K)	3.10753*10 ⁻⁸ s ⁻¹

As reported in the literature that diffusion of metal ions inside the metal oxide lattice may contribute to major portion of the activation energy¹¹⁷. So, it is possible that the activation energy of 176.45 KJ/mol could correspond to the activation energy needed for diffusion of copper ions inside the lattice of titania NWs.

5.3 Alloying studies with various physical forms of the precursors

5.3.1 Copper metal precursor coated on titania NWs

It is also important to understand the rationale behind the selection of precursors toward solid state alloying reaction. In an experiment, a thin layer of 20nm uniform copper metal layer was deposited on titania nanowires using a thermal evaporator. The sample was subjected to heating inside a TEM microscope using in-situ heating stage. The TEM stage

was heated up to 500 deg C and was kept at the reaction time of 1h. In comparison, similar sample was treated under the conditions of vacuum annealing. The samples were analyzed with TEM EDX elemental analysis. As shown in Figure 5.11b, it is observed that the 20nm copper layer tends to form smaller nanosized particles on the surface of nanowires under the TEM in-situ heating conditions. The similar sample under the conditions of vacuum annealing also showed the similar particle formation on the top of nanowire instead of alloying. This observation clearly indicates that solid copper layers are not suitable for solid state alloying reactions. The cohesive energy of copper may prevent it from reacting with titania surfaces. Additional experiments were carried out using other solid and liquid precursors of copper oxide and copper acetate.

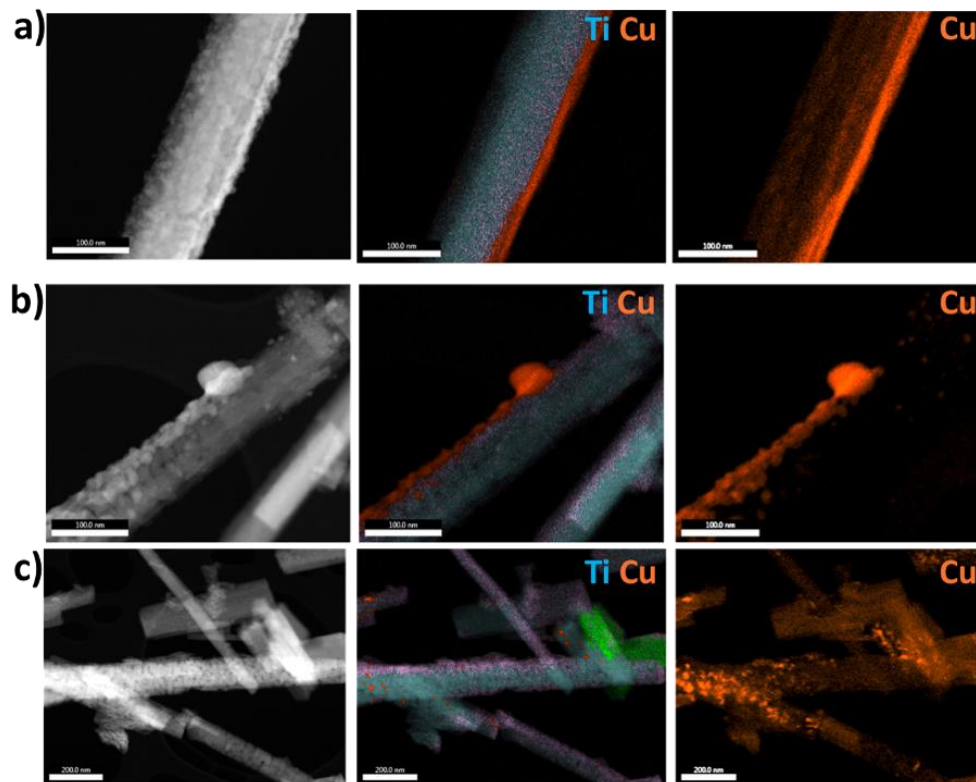


Figure 5.11. Thermal evaporation of cu metal layer on the titania NWs a) Metal copper 20nm layer as coated; b) after the In-situ heating in the TEM at 500 deg C for 1h; and c) vacuum annealing of copper metal coated on titania NWs at 500deg C

5.3.2 Copper nitrate precursor coated on the titania nanowires

TEM image analysis performed on the as prepared titania NWs, copper nitrate coated titania nanowires, and, on the copper alloyed nanowires as shown in Figure 5.12. The TEM image analysis is performed at different image resolutions. As prepared titania nanowires shows the crystalline nanowires with defects. The copper precursor coated on titania nanowires shows a thin (less than 1nm) non continuous layer of copper nitrate precursor. In the alloyed nanowires, the copper precursor layer was completely alloyed into the nanowires. There is no noticeable layer of copper nitrate precursor coating is observed.

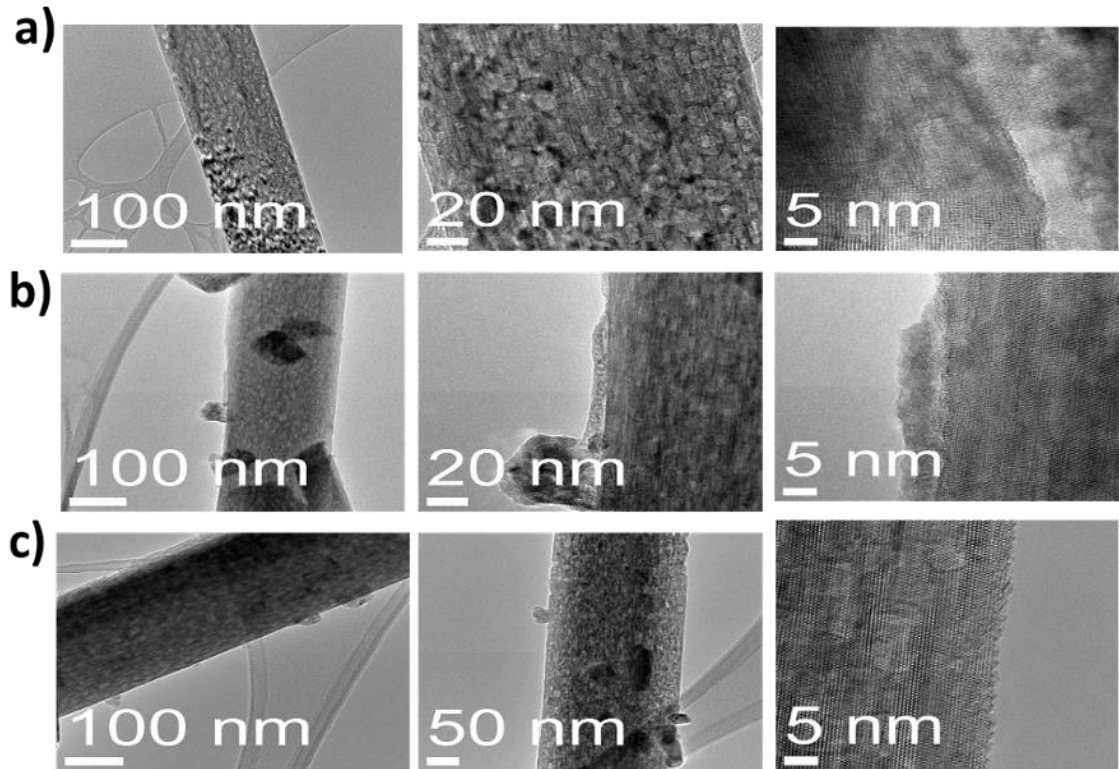


Figure 5.12. TEM image analysis at different resolutions of a) as synthesized titania porous nanowires; b) copper nitrate precursor coated porous titania nanowires with discrete nanoclusters of copper nitrate; and c) copper alloyed titania nanowires after solid state alloying under inert atmosphere.

5.3.3 Copper acetate and copper oxide precursor coated on titania NWs

Solid state alloying experiments were performed using solid and liquid precursors of copper oxide and copper acetate. The precursors were first dissolved in water. Later, a fine paste was prepared by mixing with the titania NWs. The samples were dried at a temperature of 85 deg C under the atmosphere conditions. Then the samples were grounded and used with the DSC analysis. The change in enthalpy of reaction as a function of the temperature is measured. Figure 5.13c shows that at about 120 deg C there is an endothermic peak corresponding to the water evaporation from the sample. The peak at about 200 deg C corresponds to the alloying of copper acetate precursor with the titania NWs and at about 250 deg C the copper acetate decomposition occurred along with other gaseous by products. The peak at about 200 deg C could be attributed to the slower alloying kinetics of copper acetate reaction with the titania nanowires.

Also, the titania NWs were alloyed with the copper oxide precursor, as shown in the Figure 5.14c. The data shows that the copper oxide shown a small endothermic peak at about 250 deg C. This could correspond to the copper oxide transformation to other oxides of copper. Also, the TEM EDX elemental analysis on the copper oxide alloyed with titania sample shows the segregated copper oxide on the titania NWs. The studies using different precursors suggest that acetates and nitrates of precursors are more favorable for reaction with metal oxide surfaces than oxide and/or metallic precursors.

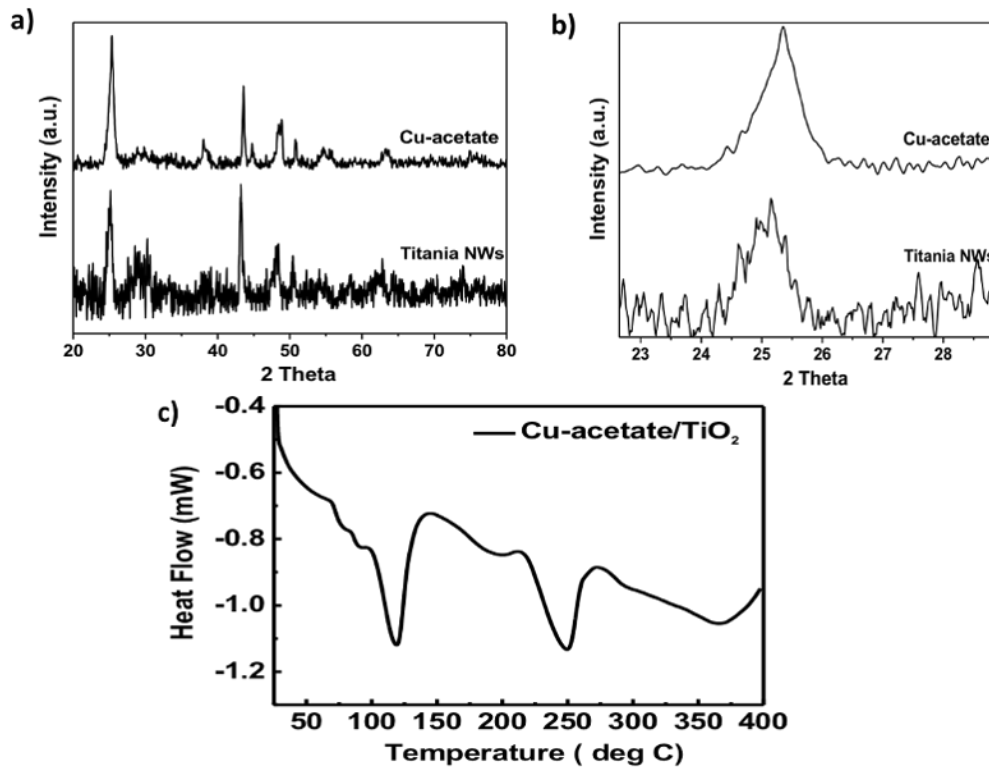


Figure 5.13. a) &b) X-ray diffraction analysis of copper acetate precursor alloyed with titania NWs; and c) DSC analysis of titania nanowires coated with the copper acetate precursor.

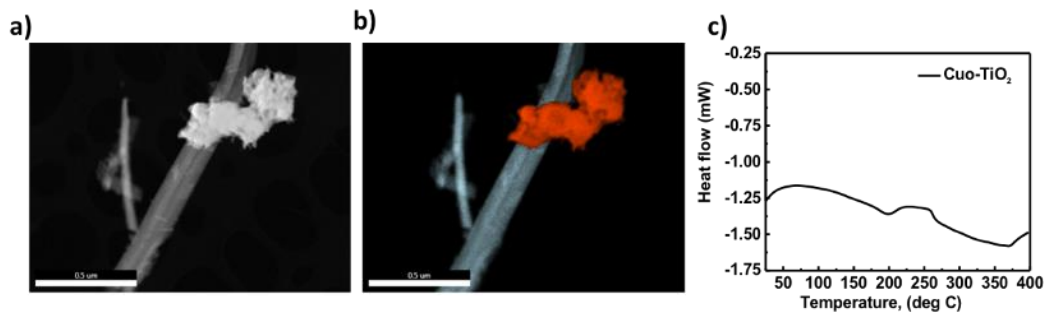


Figure 5.14. a) &b) TEM EDX elemental analysis of copper oxide alloyed with the titania NWs; and c) DSC analysis of the copper oxide precursor coated titania NWs

5.3.4 Alloying studies on the solid-state precursors

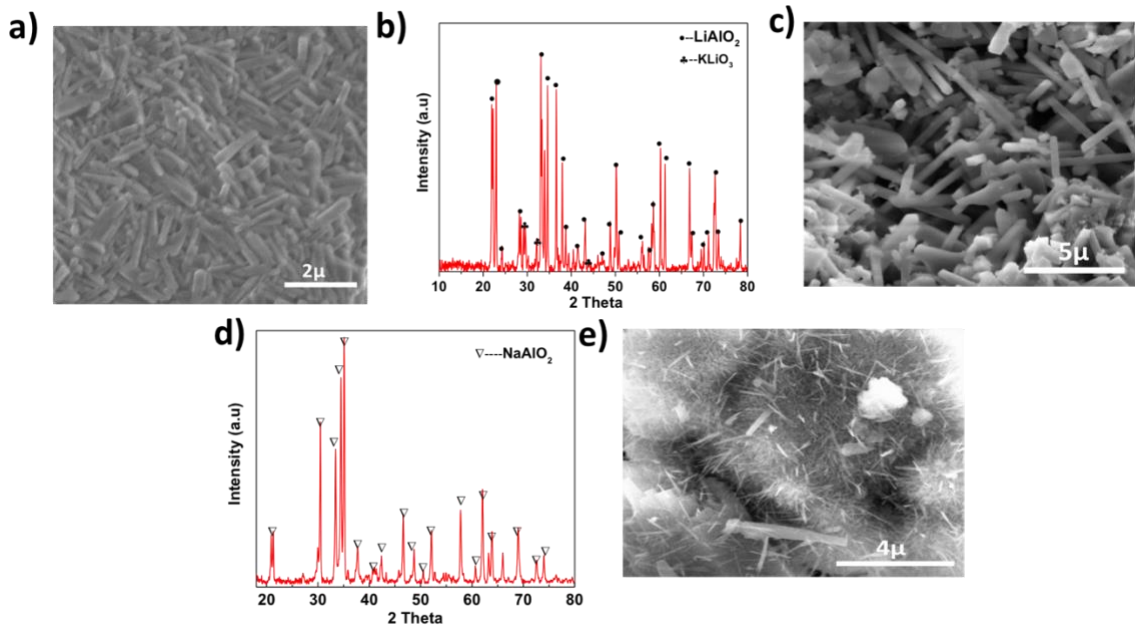


Figure 5.15. SEM image analysis and X-ray diffraction analysis of the lithium aluminate, sodium aluminate and nanowires

Here, lithium aluminate and sodium aluminate thermodynamically stable metal oxide nanowires were synthesized by reacting the solid precursors of sodium hydroxide or lithium hydroxide with the alumina nanowires at the thermodynamically desired temperatures. In brief, the required molar composition of precursors was wet mixed and dried at a temperature of 80 deg C for 1h. Later, the precursor mixture was grounded, and solid state alloyed at a temperature of 700 deg C for 3h to obtain the thermodynamically stable mixed metal oxide nanowires. As shown in Figure 5.15., SEM image analysis shows the nanowires morphology is retained after the reaction and X-ray diffraction analysis shows the pure phases of lithium aluminate and sodium aluminate nanowires.

5.4 Copper alloying with the bulk sized precursor and studies on flame environments to enhance the solubility limits

The following alloying experiments were conducted with titania nanowires in comparison with the bulk sized titania precursor materials. Like the previous studies of copper alloyed with titania NWs, copper nitrate precursor is mixed with the 5-micron bulk sized titania powder. The precursor mixer was dried, and vacuum annealed to obtain the alloyed nanowires. Figure 5.16a shows the TEM EDX elemental analysis on the copper alloyed with bulk titania material. There is a presence of surface segregated copper oxide and no alloying of copper into the bulk of the titania sample is observed. Also, X-ray diffraction analysis of the copper alloyed with bulk titania shows the peaks related to the secondary crystalline copper oxide. These results indicate that the copper is not alloyed into the bulk of titania as observed in the case of copper alloyed titania nanowires. Also, the copper oxide formed is remained as a binary composite of $\text{TiO}_2\text{-CuO}$.

Experiments were conducted with different plasma flame exposures to check the effect of rapid heating on alloying process and possibility to promote the oxygen vacancy formation during the alloying process. The hypothesis is that the alloying can be enhanced through the creation of more oxygen vacancies, and this could accelerate the vacancy diffusion of alloying element into bulk of nanowire. Copper nitrate precursor with the composition of 12 at% loaded on titania nanowire samples were exposed to nitrogen and hydrogen plasma environments for a duration of 1 min in a different experiment. The samples were characterized with the X-ray diffraction analysis to check the possibility of expanding the alloying limits under rapid heating environments. From Figure 5.16c, the sample exposed with nitrogen plasma X-ray diffraction pattern exhibited separate diffraction peaks of two crystalline phases of titania rutile and anatase titania. Also, there

were diffraction peaks correspond to crystalline phase of copper oxide as well. This result indicates that the rapid heat could have caused the immediate decomposition of the copper nitrate precursor into the copper oxide and higher plasma temperature caused the phase change of titania nanowires from anatase to the rutile phase. On the other hand, a similar sample is exposed under the hydrogen plasma environment. The plasma power used was relatively low plasma power compared to the nitrogen plasma. As shown in Figure 5.16c, X-ray diffraction pattern shows the peaks correspond to the crystalline copper phase and titania anatase phase. The formation of copper crystalline phase could relate to the reduction of copper oxide formed from the decomposition of copper precursor under the reductive environments. There are no phase changes to titania nanowires at the low power microwave plasma.

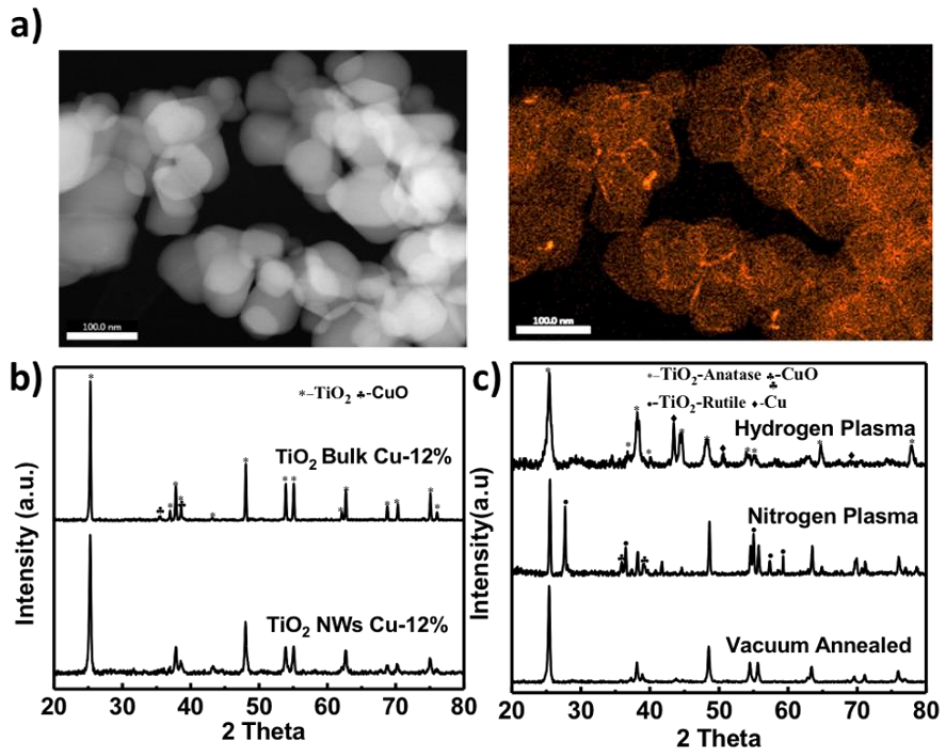


Figure 5.16. a) TEM EDX elemental analysis; b) X-ray diffraction analysis of the copper alloyed titania NWs and bulk titania; and c) Exposure of copper nitrate coated titania NWs under different flame environments.

5.5 Proposed mechanism of alloying of copper into the titania NWs

A model for the alloying of copper into the titania nanowires is proposed based on the experimental observations. Figure 5.17 (A) shows that copper nitrate precursor forms a reactive intermediate non continuous layer of copper nanoclusters (<1 nm) on the surface of titania nanowires. It is hypothesized that the copper atoms are dissolved through the nanoscale surface reaction between copper nitrate precursor and titania NWs. The diffusion of copper atoms from the surface to bulk of the titania NWs could be aided by the counter diffusion of oxygen vacancies from bulk to surface of titania NWs.

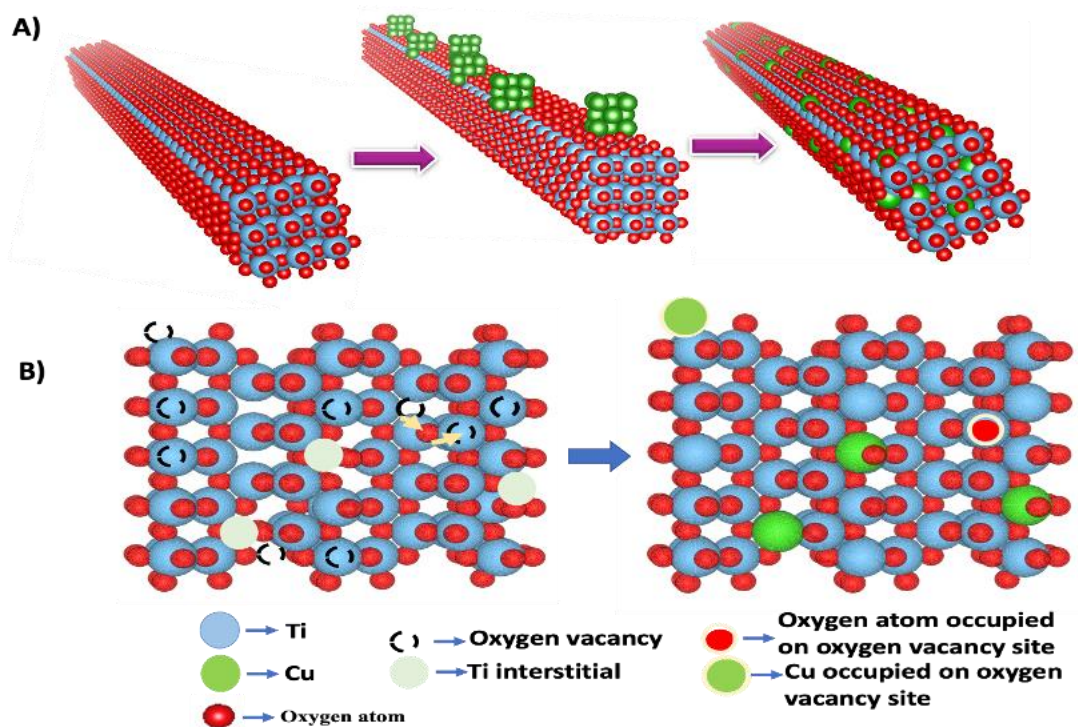


Figure 5.17. Structural model depiction of mechanism of copper alloying process into the titania NWs using the VESTA software A) Schematic of alloying process on the nanowires B) Atomic model visualization of copper alloying process in the titania NWs.

The solid-state alloying mechanism is explained through the following steps.

Step (a)- As synthesized nanowires coated with the copper nitrate precursor

Step (b)- Formation of the reactive intermediate of copper nitrate on the surface of titania NWs

Step (c)- Favored by the vacancy mediated diffusion of copper atoms into the bulk of the titania nanowire material.

From Figures 5.7 and 5.8 DSC data and Gibbs energy calculations, it is possible that alloying reaction of copper nitrate precursor with titania nanowires and decomposition reaction of copper nitrate to copper oxide, nitrous oxide, are the two major competing reactions. The alloying reaction temperature is measured around 170-190 deg C and the decomposition temperature of copper nitrate precursor is about 225-250 deg C from the DSC experiments. It is found from the DSC experiments that the decomposition of precursor may not be necessary for alloying. Therefore, alloying experiments were conducted before the decomposition temperature of precursor 225-250 deg C. The alloying experiments were conducted at 190 deg C as shown in Figure 5.9. It was observed from the X-ray diffraction analysis that copper is completely alloyed into the nanowires. There is no phase segregation of copper oxide up to 20 at% of alloying. Also, X-ray diffraction peak shift towards the higher two theta angles suggests the lattice contraction of titania. So, it may possible that Ti^{4+} ions are substituted by the Cu^{2+} ions. So, the copper atoms may present in the substitutional sites of titania lattice. This experiment confirms the alloying reaction are favorable before the decomposition temperature of the precursor. Also, Gibbs free energy calculations of alloying reaction were performed, and it was found that alloying reaction is more favorable at lower temperature of about 130-140 deg C. The decomposition reaction calculated Gibbs free energy is more -ve at 220-230 deg C. So,

these observations indicate that decomposition precursor may not be necessary to alloy copper into the titania NWs.

Moreover, extended solubility of copper solute species into the titania NWs is related to the excess free energy on the surface of nanostructures. It is reported that for the nanostructures there is an additional free surface energy associated on the unsaturated nano surfaces^{54, 118}. Therefore, nanostructures tend to minimize the surface energy by extending to the higher solubility limits to achieve thermodynamic stabilization. From Figure 5.16 (a), it is also observed that the alloying is not favorable in bulk titania materials. The reaction mechanism in bulk titania material is more favorable towards the decomposition of copper nitrate precursor reaction than the surface reaction with the titania nanowires. So, the formation of segregated phases of titania and copper oxide is observed. This is in line with the proposed mechanism and experimental data of favorable reaction of copper nitrate precursor on the surface of titania NWs.

Experiments were conducted on different precursor of copper shown in Figures 5.11, 5.12, 5.13, and 5.14 indicated the role of ionic species in favoring the alloying reaction. The liquid precursors of nitrates, acetates are more favorable than solid precursors Cu metal and copper oxide precursors for the alloying reaction. Also, the lean oxygen environment might have favored the enhanced Ti self-diffusion coefficient and oxygen vacancy formation in the titania lattice. As shown in Figure 5.7 (b), DSC thermogram data suggests the alloying reaction is more favorable at oxygen lean atmosphere (under nitrogen exposure) and decomposition reaction of precursor is favorable under the atmospheric pressure. The reported data under the oxygen lean environment also suggests the increase in self-diffusion coefficient of Ti and O diffusivity¹¹⁹. It is found out that the enhancement

in the Ti diffusivity is due to the formation of Ti interstitials, oxygen diffusion enhancement is due to the production of more oxygen vacancies. It is possible that the oxygen vacancies move towards the surface of nanowires and aid the copper atoms moving towards the bulk of the nanowires. This could further enhance the copper nitrate reaction with the surface of nanowires due to presence of higher density of oxygen vacancies on the NW's surface. So, the copper atoms diffusion in the titania lattice is promoted through the oxygen vacancies and titania interstitials.

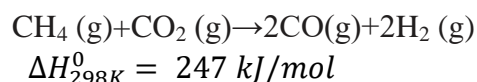
5.6 Chapter summary

We demonstrated a simple and general scalable method for synthesis of mixed metal oxide nanowires from porous pristine binary oxide nanowires. In this study, porous titania nanowires and alumina nanowires were alloyed with copper and zirconium without any secondary phases. X-ray diffraction results show that titania could alloy up to a nominal composition of 20 cu% without any segregated secondary phases. Alumina could alloy up to cu 30% nominal copper composition without the secondary phases. From the thermodynamic phase diagrams there is no solid solutions possible for both systems of CuO-TiO₂ and CuO-Al₂O₃ at 500 deg C. The extended solubility improvement is related to the enhanced surface energy in nano structures compared to bulk material. Also, high solubility for zirconia alloying into the titania NWs is observed shown up to 8 at% from EDX elemental analysis. However, the bulk solubility of zirconia in titania is only 5 at% at 1700 deg C. The utility of synthesized nanowires increases the UV absorption range of titania NWs. A model for the alloying copper into the titania nanowires is proposed. Herein, copper nitrate precursor forms a reactive intermediate non-continuous layer of copper nanoclusters (<1 nm) on the surface of titania nanowires. The reactive intermediate could

undergo competing reactions between the alloying and decomposition reactions. It is hypothesized that copper atoms are dissolved by concentration gradient into the titania NWs lattice and further undergo vacancy diffusion mechanism to diffuse into the bulk of the nanowire material. The copper diffusion in titania lattice is promoted by oxygen vacancies and Ti interstitials. We further demonstrate the effect the of the different flame exposures and the size of the solvent on the alloying. Study of thermograms with the DSC experiments and Gibbs free energy calculations indicates that the alloying of copper into the titania could occur at lower temperature of 179.3 deg C than the decomposition temperatures copper nitrate precursor at 225-250 deg C, and the effect of size of solvent nanowires on alloying process has been studied. Liquid precursors of copper are shown to be more favorable towards the alloying reaction than the solid precursors.

CHAPTER 6 MIXED METAL OXIDE NANOWIRES AS DUAL ATOM CATALYSTS IN DRY METHANE REFORMING REACTION

DMR (Dry methane reforming) reaction is an environmentally important process as it uses the greenhouse gases such as methane and CO₂¹²⁰. Also, it produces a mixture of CO & hydrogen known as syngas, a fuel gas used production of high value chemicals. The product formation reaction is an endothermic reaction. However, rapid coke formation and sintering of catalyst particles at high reaction temperature are the bottlenecks to the commercialization of the DMR reaction. Also, Ni catalyst particle size is (such as > 7nm) is known to significantly influence coke formation during the DMR reaction¹²¹. It is hypothesized that a catalyst with atomically dispersed sites can potentially prevent coke formation. Also, catalysts in the form of nanowires could exhibit less to no sintering at higher reaction temperatures. Thus, the mixed metal oxide nanowires appear to be a promising solution due to dispersion of active sites at atomic level in nanowires. Nickel alloyed titania nanowires are proposed as a catalyst to test in DMR (Dry methane reforming) reaction,



Furthermore, the DMR reaction test results of mixed metal oxide nanowires were compared against the metal supported nanowires.

6.1 Nickel alloyed titania nanowires synthesis and material analysis

The samples of nickel alloyed titania nanowires were prepared using the alloying method described in Chapter 3. Specifically, nickel nitrate was mixed in desired quantities with titania nanowires followed by drying at 80 deg C, calcining at 500 deg C under inert conditions for 1h to synthesize nickel alloyed titania NWs. Materials analysis was performed using the scanning electron microscope to show morphology of nanowires with the lengths around 4-6 micron and 150-200 nm in diameter. TEM EDX elemental analysis on fresh catalysts indicates that the nickel is distributed uniformly as an alloyed element throughout nanowires as shown in Figure 6.1c. Furthermore, X-ray diffraction pattern reveals that the fresh catalyst only contains the phase of titania anatase as major phase. No nickel oxide peaks are seen suggesting nickel is alloyed into titania nanowire and no segregated nickel oxide particles are present on the top of the nanowires. Also, XRD peak shift in titania peaks are observed after the alloying indicates that there are changes in the titania lattice.

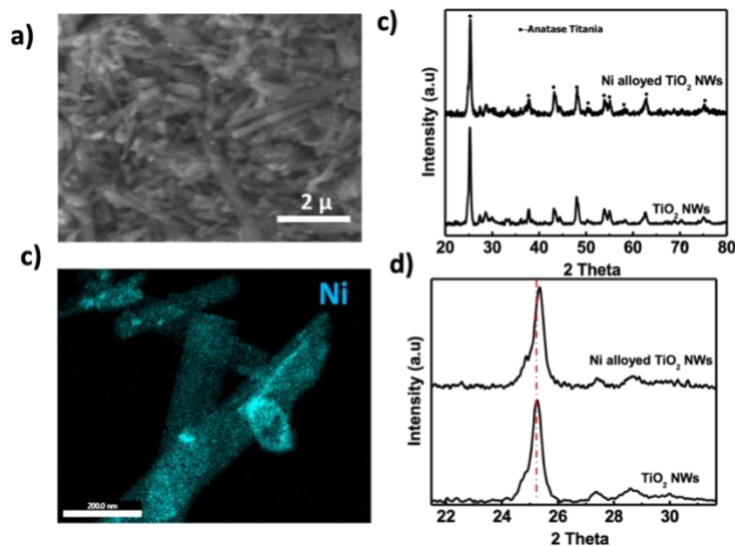


Figure 6.1. Nickel alloyed titania sample (8 wt%) a) SEM image analysis of fresh catalyst sample b) TEM EDX analysis of nickel alloyed titania sample c) XRD analysis of fresh catalyst sample d) Peak shift analysis of nickel alloyed titania sample

6.2 DMR test with nickel alloyed/decorated titania nanowires

The DMR reaction was carried out in a packed bed reactor set up as shown in Chapter 3. The reaction was carried out at atmospheric pressure using reactant gas flow with a GHSV of $60000 \text{ mlgr}^{-1} \text{ h}^{-1}$, at stoichiometric ratio of 1:1 for reactants. The reaction temperature was varied from 750-850 deg C. Figure 6.2a shows that a conversion of 79-81% for CO_2 and 50-53% for methane over a period of 20h is achieved at the reaction temperature of 750 deg C. At 800 deg C the conversion increased to 93-95% for CO_2 and 76-77% for methane over 10 h. At 850 deg C, the conversion for reactants as high as 96-97% for CO_2 and 83-86% for methane is observed over a period of 20 h. There is no carbon deposition observed on the catalyst from TGA data and TEM EDX data.

In comparison, as shown in Figure 6.2b, nickel particles decorated/supported on titania nanowires yielded 96-97% conversion for CO₂ and 55-58% for methane a period of 20 h. At 800 deg C the conversion increased to 98-100% for CO₂ and 55-58% for methane over 50 h. Most importantly, carbon deposition is observed in decorated nickel on titania nanowire samples.

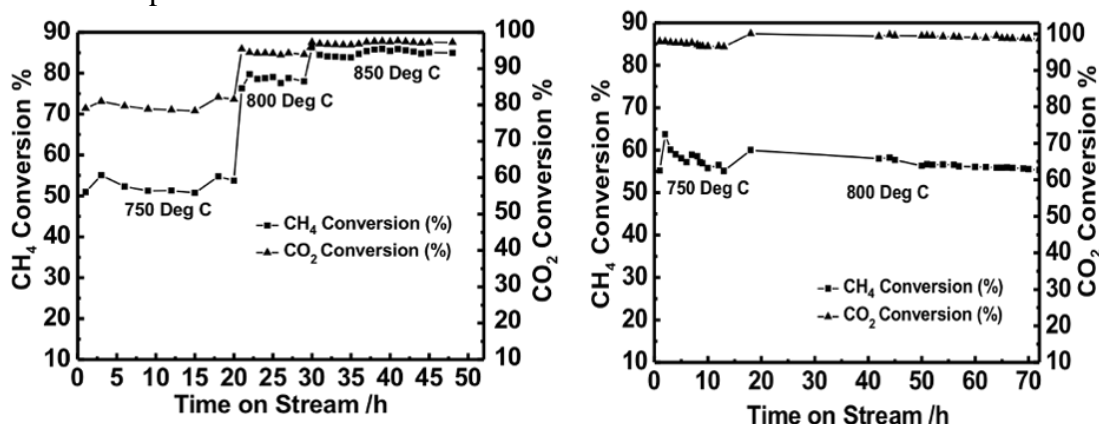


Figure 6.2. Nickel alloyed/decorated titania NWs sample DMR test performance a) nickel alloyed sample b) Ni metal decorated on titania NWs, Methane and CO₂ conversion at different temperatures (at 750-850 deg C, GHSV of 60000mlgr⁻¹h⁻¹, feed ratio of methane to carbon dioxide of 1).

Table 6.1 Comparison DMR catalyst performance data

Process reaction	Ni alloyed into the titania NWs Catalyst	Ni decorated/supported on titania NWs catalyst
Dry reforming of (CH ₄ +CO ₂) conversion to syngas	CO ₂ /CH ₄ , GHSV-60-300 L/h, T-750-850 °C, P-1 bar Result: CO ₂ conversion 80-100% and CH ₄ conversion-55-86%	CO ₂ /CH ₄ -1, GHSV-60-300 L/h, T-750-850 °C, P-1 bar Result: CO ₂ conversion 85-100% and CH ₄ conversion-58-61%

6.3 DMR test spent catalyst material analysis

Furthermore, thermogravimetric analysis (TGA) was performed on the spent materials to quantify and characterize the carbon deposits formed in both supports. A

starting weight of approximately 20 mg was placed in a porcelain cup in the SDT-Q600 instrument. The sample was heated up to 1000°C using a heating rate of 10°C per minute under the air flow of 100 ml/min. From Figure 6.3a TGA analysis on the alloyed samples have not shown any change in weight indicating the absence of carbon deposition. On the other hand, TGA analysis from the nickel decorated titania nanowires shows a decrease in weight from temperatures at 508 deg C and stabilized at around 726 deg C. The observed weight loss is due to burning of coke formed on the catalyst.

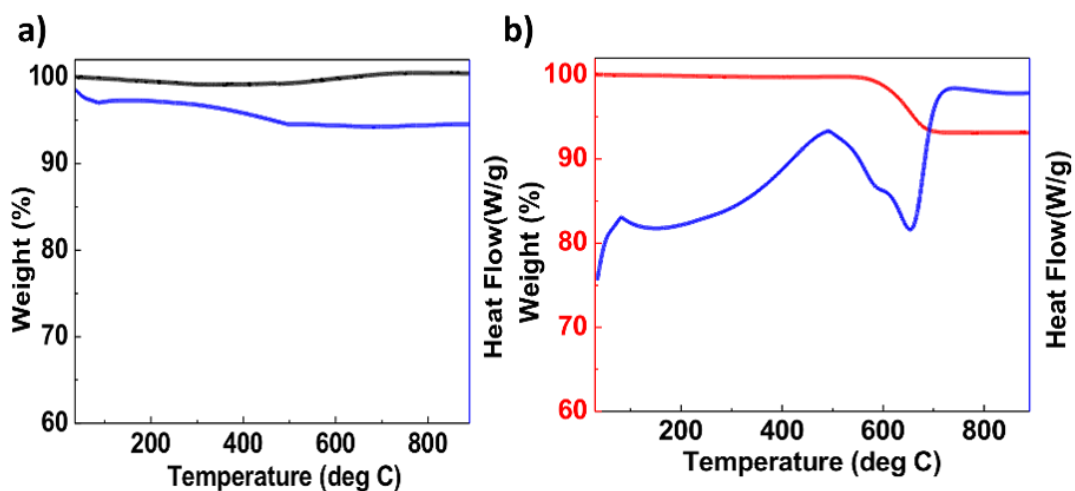


Figure 6.3. DMR reaction spent catalyst samples nickel alloyed and decorated titania NWs TGA analysis a) spent catalyst sample of nickel alloyed titania NWs b) spent catalyst sample of nickel decorated on titania NWs

Several characterization analyses such as SEM image analysis, X-ray diffraction analysis and TEM EDX analysis was performed on both the alloyed and supported catalysts to understand the catalyst durability. The XRD analysis of fresh and spent sample of nickel decorated catalyst shown that there is change of phase of titania from anatase to rutile. See Figure 6.4, Also, the nickel oxide in the fresh sample is converted to the nickel metal during the reduction reaction. TEM EDX analysis on the fresh sample shows well dispersed nickel on the titania NWs and absence of carbon. However, the spent sample contains larger sintered nickel particles along with carbon deposits.

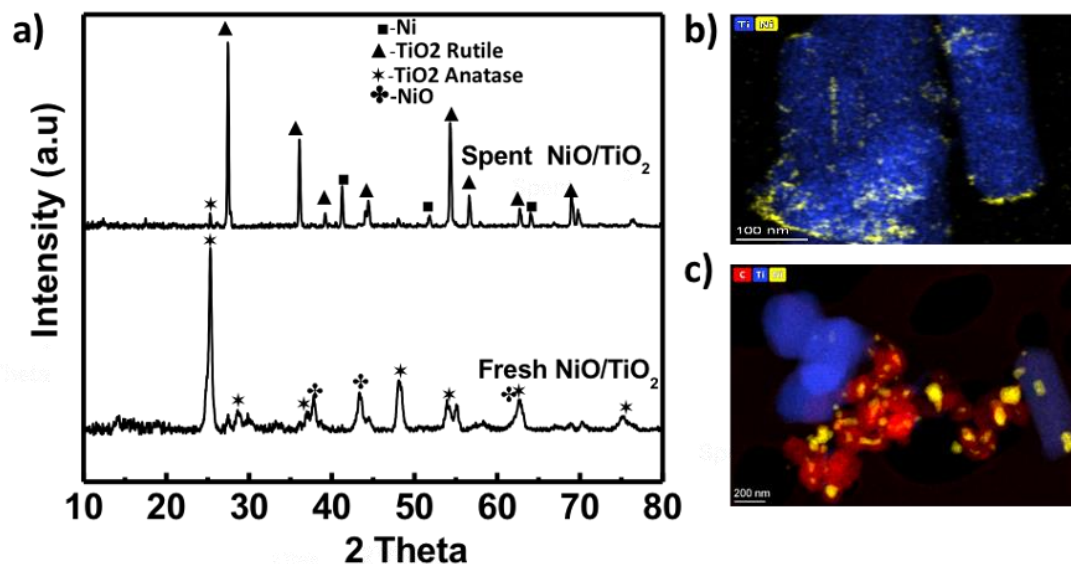
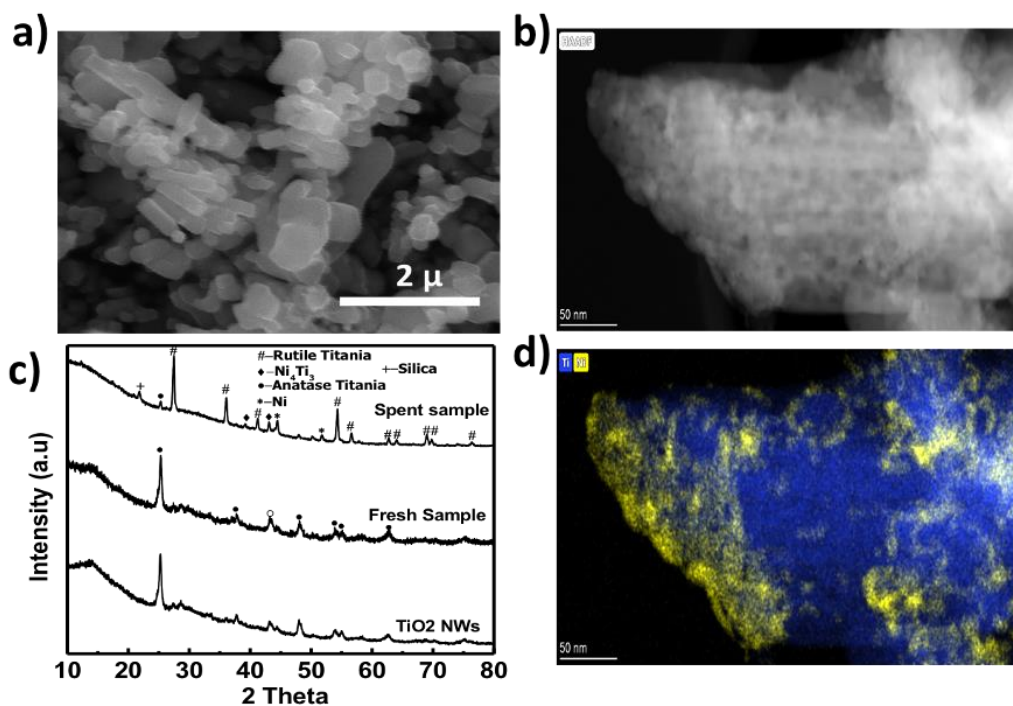


Figure 6.4. Nickel decorated titania NWs a) X-ray diffraction analysis of fresh catalyst sample and spent catalyst sample of the dry methane reforming reaction c) TEM EDX analysis of fresh catalyst sample d) TEM EDX analysis of spent catalyst sample of the DMR testing.

In contrast, the SEM image of nickel alloyed titania spent sample in Figure 6.5 shows that the nanowire morphology is still retained even after the 50h on the stream. Also, X-ray diffraction analysis shows the presence of alloy phase of Ni_4Ti_3 . Moreover, the TEM EDX analysis clearly indicates there is no coke deposit in the spent sample and nickel is distributed uniformly throughout nanowires like that of fresh sample. The alloyed sample with no carbon deposition and no changes with structure suggest durability with performance compared to supported catalyst. In the case of supported nanowire catalysts, the deposition of carbon could block the active sites of the catalyst sample and the sintering nickel particles could heavily promote coke deposition. Also, it is observed that there is a slight decrease in the performance of nickel supported catalyst as the reaction proceeds. This could further support the argument of catalyst surface is modified compared to the

fresh catalyst. The proposed mechanism of alloyed catalyst is shown in Figure 6.5e. Nickel alloying in titania could create the oxygen vacancies on the titania surface. This could provide the surface with oxygen vacancy next to the nickel atom. This synergy on the titania nanowire surface could enhance performance of the catalyst. As shown in Figure 6.5e, the carbon dioxide could chemisorb on the oxygen vacant site and on the methane, molecule could favor to react on the nickel surface. The reported data shows that the activation of methane on the nickel surface is the rate limiting step in the DMR reaction¹²². Ni site along with oxygen vacancy could lead to dual atom type catalyst. The synergy of Ni alloying into the titania NWs is contributing to the higher performance of the catalyst.



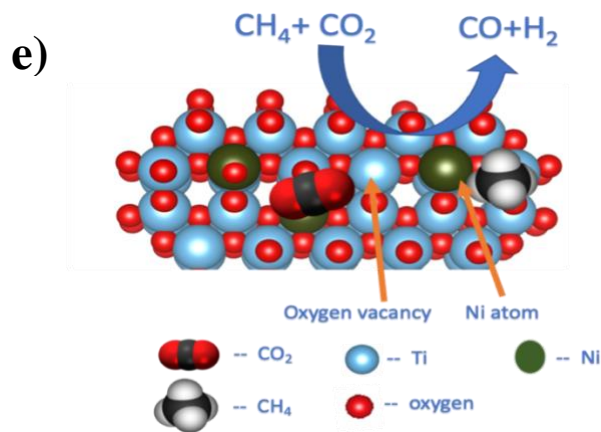


Figure 6.5. Nickel alloyed titania NWs spent catalyst sample of DMR reaction a) SEM image analysis b) & d) TEM image and EDX analysis of spent sample showing the distribution of nickel and titania c) X-ray diffraction analysis of spent sample in comparison with fresh sample e) Molecular level depiction of proposed DMR reaction mechanism on Ni alloyed titania NWs

6.4 Chapter summary

The chapter summarizes experimental results obtained with dry methane reforming reaction using mixed metal oxide nanowire catalysts. The use of mixed metal oxides specifically with nickel alloyed titania represent as first of its kind single or dual atom nanowire catalysts for DMR reaction. The catalyst activity of nickel alloyed into the titania nanowires sample is 96-97% for CO₂ and 83-86% for methane conversion to more than 50 hours. In comparison, nickel supported on commercial titania nanowires exhibited activity of 98-100% for CO₂ and 55-58% for methane conversion over 50 h. The spent samples SEM image analysis, X-ray diffraction analysis, TGA analysis and TEM EDX analysis provided more insights into the catalyst performance. The deposition of carbon on the catalyst surface lead to the blocking of the active sites and decrease in efficiency of catalyst from the sintering of nickel particles is observed in nickel decorated titania nanowire samples. The alloyed nickel titania sample is resistant to the coking and catalyst surface modifications and showed durability over temperature range and time. This is due to the

dual type of catalyst sites were formed on the nickel alloyed titania surface. Also, this helps in promoting the activation of methane on the nickel sites and CO₂ activation on the oxygen vacant site.

CHAPTER 7 APPLICATION OF POROUS TIN OXIDE NANOWIRES IN ELECTROCHEMICAL CONVERSION OF CO₂

7.1 Introduction

Despite significant progress in the field of carbon-neutral renewable energy production, global atmospheric CO₂ concentration continues increasing and has reached a level unprecedented in human history (~ 400 ppm).¹²³ There is growing concern this could have potentially devastating consequences from the associated CO₂ greenhouse gas effects.¹²⁴⁻¹²⁶ Thus, both the development of a carbon-neutral economy and the fixation of human sources of CO₂ emissions are of prime importance in current research efforts.¹²⁷ Numerous CO₂ fixation technologies such as the transformation of CO₂ to carbonate salts,¹²⁸ formation of carbamates,^{129, 130} chemical conversion,¹³¹ and photo- or electrochemical reduction into useful products^{132, 133} are emerging rapidly. Electrochemical conversion of CO₂ is especially advantageous as it facilitates the conversion of CO₂ emissions into energy-dense and higher value chemicals such as syngas, ethanol, etc. Liquid products (e.g., formic acid, ethanol) produced via the CO₂ electrochemical reduction process are particularly suited for the energy-dense storage of electrical energy from renewable sources for use at night, during periods of off-peak demand, or in transportation applications.^{134, 135}

However, achieving a simultaneously high product selectivity and conversion rate is challenging due to high kinetic barriers and the myriad possible reaction pathways for CO₂ reduction. Numerous elemental metals (e.g., Ag, Au, Cu,) oxide-derived metal

nanostructures (e.g., reduced CuO_x, SnO_x), carbon nanomaterials (N-doped graphene, carbon nanotube arrays, carbon nanofibers) and metal complexes (e.g., copper complex) have been investigated as catalysts for CO₂ reduction in search of a practically viable electrochemical CO₂ recycling process.^{132, 133, 136, 137} Particularly, Sn and related catalysts (e.g., Sn/SnO_x) are more selective for HCOOH formation, which is usable as a fuel in direct formic acid fuel cells (DFAFC).¹³⁸⁻¹⁴⁰ HCOOH has recently shown promise as a basis for a hydrogen storage technology.^{141, 142} Despite a low H₂ mass content (4.4 wt%), formic acid is an attractive H₂ storage media due to its low volatility (vapor pressure of 40 mmHg at 20°C), stability, portability, and comparably high volumetric capacity (53.4 g H₂/L at ambient temperature and pressure) in comparison to current state-of-the-art H₂ storage materials (e.g., chemical hydride and liquid hydrogen).¹⁴²

Recent work has shown pure elemental Sn with the native oxide layer chemically removed did not appreciably reduce CO₂ at relevant potentials.¹⁴⁰ The native oxide layer was reported to facilitate the CO₂ reduction, but only at > 0.8 V overpotential with a current density of only 3 – 4 mA cm⁻².¹⁴³ The HCOOH formation faradaic efficiency (F.E.) and CO₂ reduction reaction rate are highly sensitive to the oxide layer thickness,¹⁴⁴ nanoparticle catalyst size,¹³⁹ and experimental conditions (e.g., pH of the electrolyte).¹⁴⁵ Some studies have modestly enhanced the HCOOH formation ability of Sn-based catalysts by varying the oxide layer thickness on hierarchical catalyst nanostructures without altering the original active sites.^{139, 146}

On the other hand, grain boundaries (GBs) are proposed to be enhanced active sites for CO₂ and CO electrochemical reduction into valuable products due to their favorable electronic and chemical properties.¹⁴⁷⁻¹⁴⁹ In particular, computational studies have

suggested that the broken local spatial symmetry near a GB tunes the binding energy of the reaction intermediate facilitating CO₂ electrochemical reduction.¹⁵⁰ GBs in a Sn catalyst are thus predicted to enhance HCOOH formation, particularly in terms of selectivity and overpotential. We therefore synthesized SnO₂ porous nanowires (Sn-pNWs) with a high density of GBs with a scalable plasma synthesis technology and characterized their CO₂-to-HCOOH formation ability. Our results confirm that Sn-pNWs with a high GB density began reducing CO₂ at a lower overpotential (~350 mV) and with > 10x higher current density compared to crystalline SnO₂ nanowires (Sn-NWs) without grain boundaries.

7.2 Material analysis of the porous tin oxide NWs

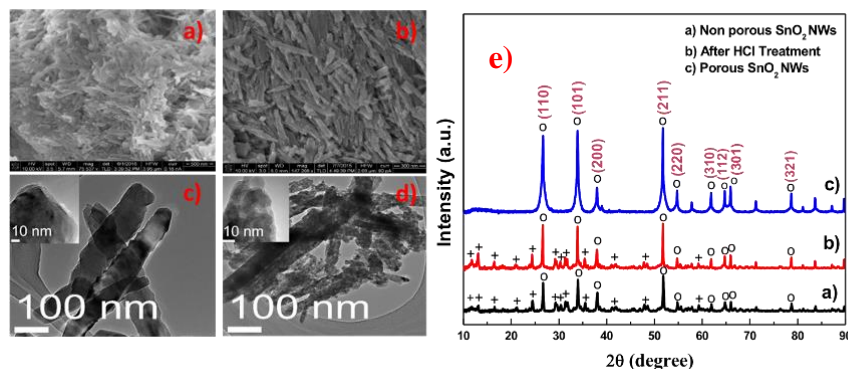


Figure 7.1. Experimental data of a)&b) SEM image analysis c)&d) TEM image analysis and, e) X-ray diffraction analysis of as synthesized and porous tin oxide nanowires

The SnO₂ porous nanowires (Sn-pNW) catalysts explored in this work were derived from a potassium-rich SnO₂ nanowires form (Sn-NW) synthesized by a previously described scalable solvo-plasma technique (see materials and methods chapter for more details).¹⁵¹ The morphology of the as-synthesized nanowires was consistent with an absence of any observable structural defects (Grain Boundaries-GBs) even at the nanoscale (Figure 7.1c inset). However, after an acid etch treatment in 0.5 M HCl and a subsequent annealing process, the morphology of the Sn-NWs changed drastically into the Sn-pNW

catalyst type with the wire-like morphology converted into porous nanowires where individual nanodomains are observed to be interconnected through GBs (Grain Boundaries) (Fig. 7.1d). The formed GBs are clearly visible in the high-resolution TEM Image (Figure. 7.1d inset).

7.3 Electrochemical testing of tin oxide NWs with cyclic voltammetry

Catalyst electrochemical characterization was conducted in CO₂-saturated 0.1 M KHCO₃ solution (Figure 7.2a) by casting particles on a porous carbon gas diffusion layer (GDL) substrate. CO₂ reduction polarization curves illustrated that Sn-pNWs exhibited ~10 mA cm⁻² current density at -1.0 V vs. RHE. At the same potential, 0.7 mA cm⁻² current density was recorded for Sn-NWs. Note that current densities were determined based on the geometrical surface area of the electrode with equal catalyst mass loadings per area. A straightforward interpretation of this data would be to assume that the Sn-pNW current density increased relative to the Sn-NWs due to an increase in the catalyst surface area after the acid etch and concomitant increase in the number of active sites. This hypothesis was tested by comparing the Sn-pNWs catalyst performance with commercially available SnO₂ nanoparticles (Sn-NPs, diameter ~15 nm) measured to have a high surface area per mass (~55 m²/g), as determined by a gas adsorption method. This type of Sn-NP with a native oxide layer has been reported as an effective CO₂ reduction catalyst due to an optimal binding energy of the intermediate CO₂ radical.^{139, 140} The surface area per mass of the Sn-pNWs (~35 m²/g) was measured to be lower than the commercial Sn-NPs, yet ~6 times higher than that of the Sn-NWs (~6 m²/g) before the acid etch treatment. Despite this, the Sn-pNWs exhibited more than twice the current density of the Sn-NP (Sn-nano particle) catalysts (~10 mA cm⁻² compared to ~4.1 mA cm⁻² at -1.0 V vs. RHE, Fig. 2a) and roughly

twelve times higher current density than Sn-NWs ($\sim 10 \text{ mA cm}^{-2}$ compared to $\sim 0.82 \text{ mA cm}^{-2}$ at -1.0 V vs. RHE , Fig. 7.2a). Thus, catalyst surface area alone cannot account for the observed increase in electrocatalytic activity. Instead, the results are consistent with an increase in the density of active sites or the introduction of new types of active sites during the transformation into the porous nanowire form. Guided by the TEM and BET analysis and previous studies on the effects of GBs and nanopores in catalysts,^{147, 149}

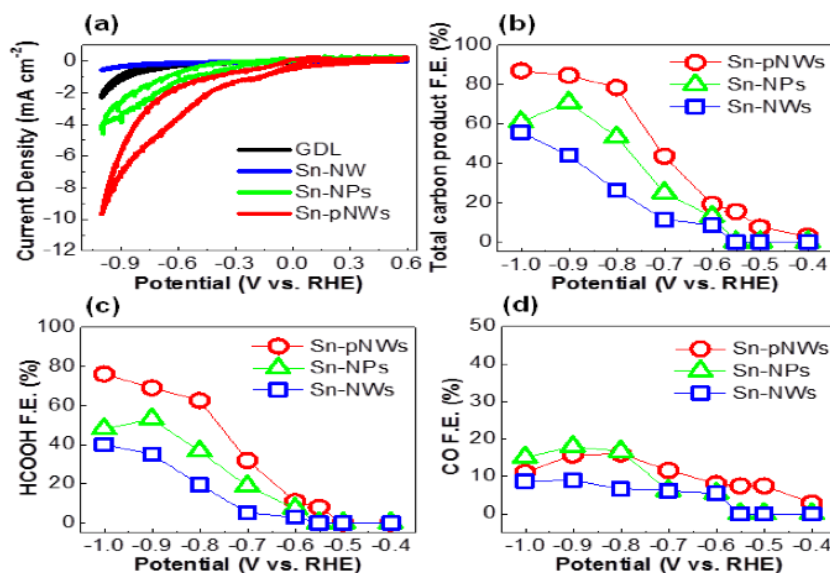


Figure 7.2. CO₂ electrochemical reduction performance data (a) J-E curves obtained in CO₂-saturated 0.1 M KHCO₃ solution for reduced Sn-NWs, Sn-NPs, Sn-pNWs, and bare GDL (substrate). Faradaic efficiency vs. potential collected over 2 h at each potential for (b) all carbon products, (c) HCOOH, and (d) CO. (Hydrogen was the only other species detected during the experiments)

Figure 7.2b shows the faradaic efficiency (F.E.) trends of the total C-products obtained for Sn-NWs, Sn-NPs, and Sn-pNWs as a function of applied potential. Only CO, H₂, and HCOOH were identified as products during the electrochemical process. At potentials more cathodic than -0.5 V vs. RHE , the total F.E. for all carbon products increased to a maximum of 55%, 70%, and 87% for Sn-NWs, Sn-NPs and Sn-pNWs, respectively. Additionally, the Sn-pNWs displayed superior C-product selectivity at each potential, further indicating that the GB sites and nanoporous morphology assist in

improving the rate of CO₂ reduction preferentially over hydrogen evolution (Figure 7.2b). For the Sn-pNW catalysts, HCOOH was identified as a product at -0.55 V vs. RHE (Fig. 5.2c), corresponding to an overpotential of only ~0.35 V (E° for the CO₂/HCOOH reaction is -0.2 V vs. RHE in aqueous media).^{137, 140} The observed overpotential is close to the reported value (~340 mV) for one of the most active HCOOH production catalysts, i.e., reduced SnO₂ nanoparticles on graphene measured under similar conditions in 0.1 M NaHCO₃.¹³⁹ At this potential, Sn-NWs and Sn-NPs were not able to reduce CO₂ into HCOOH, indicating insufficient driving force to overcome the rate-limiting step and/or relatively poor binding of the intermediate species.¹⁴⁰ Notably higher overpotential (~400 mV) at the onset voltage was observed for both Sn-NPs and Sn-NWs. Above the onset potentials, HCOOH formation F.E. continued increasing and attained a maximum value of 78%, 56%, and 45% F.E. for Sn-pNWs, Sn-NPs and Sn-NWs, respectively (Fig. 4.6c). The results indicate an enhanced HCOOH selectivity of the electrochemically reduced Sn-pNW catalysts relative to the other Sn catalyst nanostructures. CO was the only other identified carbonaceous product (Figure 7.2d). However, the F.E. for CO formation remained < 20% for all catalyst types in the measured potential range.

7.4 Electrocatalyst stability analysis

We also conducted extended chronoamperometric stability experiments for 15 hours for each of the catalysts, including the bare porous carbon GDL substrate, and examined the product distribution patterns with respect to time at an applied potential of -0.8 V vs. RHE. Gaseous products were measured at 30 min intervals while the liquid product HCOOH F.E. was calculated at the end of the experiments, i.e., after 15 hours. All the catalyst types displayed a relatively stable performance during this period. At this

potential, overall C-product (HCOOH + CO) faradaic efficiencies of ~92%, ~76%, and ~75% were obtained for Sn-pNWs, Sn-NPs, and Sn-NWs, respectively, with only ~5% observed for the substrate control measurement (Figure 7.3). The results confirm that the active CO₂ reduction sites occur primarily on the Sn nanostructured catalysts as opposed to the underlying substrate, and the observed carbonaceous products cannot be attributed to decomposition of the GDL or electrolyte.

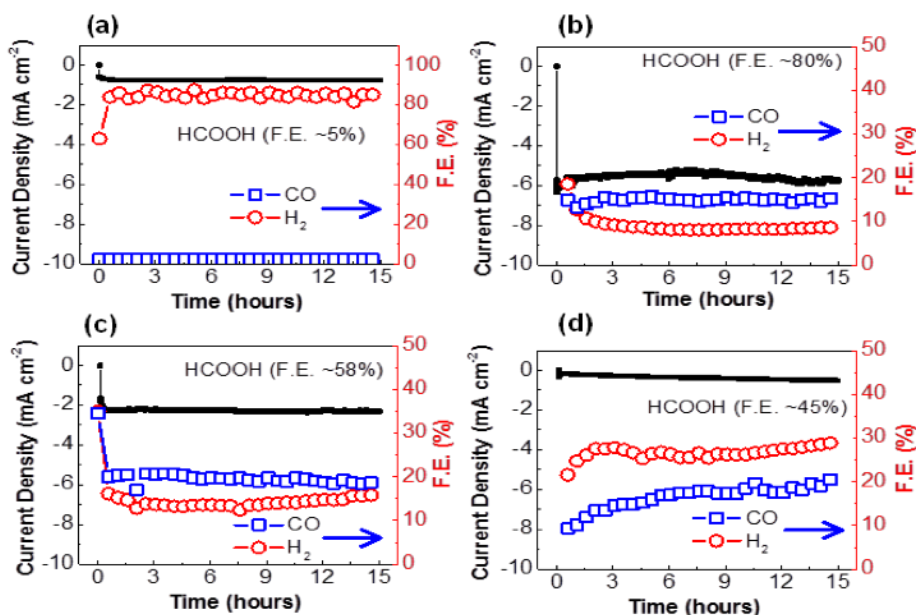


Figure 7.3. Catalyst stability: Current density (black line) and product faradaic efficiency (F.E.) vs. time for (a) a bare porous carbon GDL substrate; (b) Sn-pNWs; (c) Sn-NPs; and (d) Sn-NWs. In each case, the potential was maintained at -0.8 V vs. RHE.

The listed faradaic efficiency for HCOOH in each case was determined by NMR analysis of the liquid electrolyte after the 15 h experiments. The CO₂-to-HCOOH F.E. determined at the end of the stability measurements at -0.8 V vs. RHE for the Sn-pNW catalysts (F.E. ~80%) was 1.4x and 1.8x higher than that of Sn-NPs (F.E.~58%) and Sn-NWs (F.E.~45%), respectively. The reduced overpotential and increased C-product selectivity of the Sn-pNWs with high-density GBs and nano porous morphology suggest

an improved binding energy of CO₂ reduction intermediates and direction of protons to HCOOH formation rather than H₂ production.¹⁵⁰

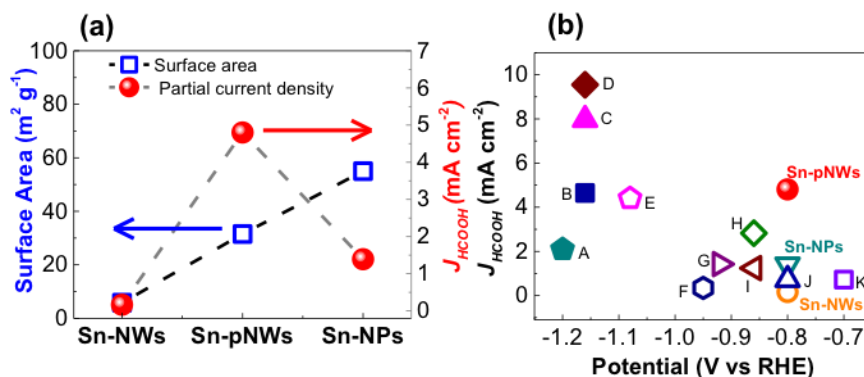


Figure 7.4. Comparison of the catalyst activity for formic acid formation (a) Measured BET surface area per catalyst mass and partial current density of formic acid production, J_{HCOOH} , of Sn-NW, Sn-NP, and Sn-pNW catalysts. Partial current density was calculated at -0.8 V vs. RHE. (b) Overview of various reported catalysts performance for HCOOH production from electrochemical CO₂ reduction in aqueous electrolyte. Here the letters represent: Sn-pNWs, Sn-NWs and Sn-NPs (this study), A – Sn plate,¹⁵² B - SnO_x/carbon black,¹³⁹ C - Sn dendrite (heated),¹⁴⁶ D - SnO_x/graphene,¹³⁹ E - Sn metal electrode,¹⁴³ F - Sn foil,¹⁵³ G - Cu₅₇Sn₄₃,¹⁵⁴ H - Sn dendrite (heated),¹⁴⁶ I - Sn dendrite,¹⁴⁶ J - Sn₆O₄(OH)₄,¹³⁸ and K - Sn/SnO_x/Ti¹⁴⁰.

A more comprehensive metric for the formic acid productivity of the catalysts is the partial current density of HCOOH formation, J_{HCOOH} , (current density times the faradaic efficiency), since it incorporates both selectivity and the reaction rate.^{155, 156} The HCOOH partial current density along with the measured BET surface area per catalyst mass for each of the catalyst types is presented in Figure 5.4a. The surface area per mass of the Sn-pNWs is ~6 times higher than that of the Sn-NWs but the J_{HCOOH} is a factor of ~30 greater. Compared to the commercial Sn-NPs, the surface area per mass of the Sn-pNWs is lower, but the J_{HCOOH} is still more than 3x higher than that of the Sn-NPs. These results further suggest that the high catalytic activity is mainly due to the increased density of GBs and nanoporous morphology of the Sn-pNWs and cannot be attributed strictly to increased electrochemical surface area. Here it should be noted that the nanopores are also considered

highly active sites where the curved internal surface offers not only a large number of active sites but also provides optimal binding sites for CO₂ reduction intermediates during electrochemical conversion.¹⁵⁷ Therefore, GBs within the nanopores could have a high impact on CO₂ reduction activity.

7.5 Chapter summary

An application of porous tin oxide nanowires with the high-density grain boundaries for CO₂ electrochemical reduction to formic acid has been studied. It is concluded that the high-density grain boundary structure is a primary factor in the observed enhancement of the selectivity and rate of HCOOH formation and associated minimization of the H₂ evolution reaction during the electrochemical reduction of CO₂. The results for the Sn-pNWs were also compared to related literature-reported catalysts to show that this nanostructure can reduce CO₂ to formic acid more efficiently than current state-of-the-art electrodes including Sn nanoparticles with a native oxide layer deposited on graphene as well as heat-treated Sn nano dendrite structures. Electrochemically reduced SnO₂ porous nanowire catalyst (Sn-pNWs) with a high density of grain boundaries (GBs) exhibits an energy conversion efficiency of CO₂-into-HCOOH higher than analogous catalysts. HCOOH formation begins at lower overpotential (350 mV) and reaches a steady Faradaic efficiency of ca. 80 % at only -0.8 V vs. RHE. With the demonstrated high selectivity for HCOOH formation, high current density at relatively low overpotential, high cathodic energy efficiency, robust chemical stability, and synthesis via a scalable plasma technique with demonstrated promise for bulk nanoparticle production, these Sn porous nanowire catalysts have promise for commercial conversion of waste CO₂ to valuable formic acid product.

CHAPTER 8 CONCLUSIONS AND RECOMMENDATIONS FOR FUTURE WORK

8.1 Results summary and conclusions

This dissertation work demonstrated the synthesis of binary porous tin oxide NWs, porous titania nanowires, porous alumina NWs using the solvo plasma method and wet chemical method. Most importantly, a viable method for the synthesis of mixed metal oxide nanowires from ex-situ alloying of binary oxide nanowires with various solutes, applicability to the several material systems, and understanding the mechanistic steps of alloying reaction. In this concept, different precursors of solutes in the form of either solid hydroxides or liquid precursors of nitrates is mixed with the synthesized nanowires and subjected to calcination at different temperatures under inert atmosphere. Results showed that the alloying depended upon the physical state of the precursor. Several experiments were conducted using in-situ TEM and differential scanning calorimetry to understand the underlying mechanism involved. Based on the results, a mechanism is proposed for the solid-state alloying process with the nanowires. Furthermore, as an examples porous tin oxide nanowire are demonstrated for the formic acid formation from the electrochemical CO₂ reduction reaction and nickel alloyed titania NWs as a dual atom catalyst for the dry methane reforming reaction. Results showed that the alloying of nickel into the titania yielded the superior performance in comparison to the nickel decorated titania catalyst.

First set of experiments were performed using copper nitrate as precursor for alloying with titania nanowires. Results showed complete alloying of titania with concentration of copper up to 8 at%. The results were confirmed using X-ray diffraction and TEM EDX elemental mapping analysis. In-situ TEM experiment was conducted with the thin layer of copper metal deposited on titania nanowires. Results indicated the formation of segregated copper particles on the surface of the titania nanowires. This could be related to the metal precursor alloying reaction is not selective to the formation of alloyed titania nanowires, and the precursor reaction with titania is favorable to the formation of copper oxide. Also, experiments were conducted with the copper oxide and copper acetate precursors for the alloying reaction with titania nanowires. Materials were analyzed with the DSC analysis and X-ray diffraction peak shift analysis. Results with copper acetate precursor indicated the feasibility of alloying reaction. On the other hand, results with copper oxide shown completely segregated phases of titanium dioxide and copper oxide. Alloying reaction studies on titania nanowires with the precursors copper nitrate, copper acetate, copper metal, and copper oxide confirm that the alloying reactions are favorable with the liquid precursors than the solid precursors. Also, it is confirmed that the uniform layer of solute on solvent nanowires is not necessary for uniform alloying.

For the general applicability of solid-state alloying method, similar concept applied for alloying of zirconium into the titania nanowires, copper into the alumina nanowires, and cobalt into the zinc oxide nanowires. Results indicated higher solubility of copper 18 at% into the alumina nanowires, upto 8 at% of zirconium into the titania nanowires, and up to 20 at% of cobalt into the zinc oxide nanowires. All the results were confirmed with the X-ray diffraction and TEM EDX elemental analysis. It is demonstrated from the results

that the alloying method could be expanded to the alloying of precursors into the other mixed metal oxide nanowire materials. Although, these materials thermodynamically do not favor the higher solubility of solutes from the thermodynamic phase diagram; the alloyed experimental results strongly suggest the formation of alloys. The apparent extended solubility could potentially attribute to the available higher surface energy at nanoscale.

Additionally, the effect of size of solvent material on the solubility of solute material is studied with bulk titania loaded copper nitrate. The results shown that bulk titania is not alloyed with copper solute, the formation of segregated copper oxide and titania were as the products. This result could ascribe to the higher surface energy available at the nano scale than the bulk material surface. In addition, to understand the influence of flame atmosphere in favoring the oxygen vacancies formation and to promote the extended solubility of solute materials. Copper coated titania samples were alloyed under the flame environments of hydrogen and nitrogen plasma. However, the results showed the segregated phases copper oxide, copper, and titania. This result may be an effect of rapid reactions under the high energy flame environments.

Furthermore, DSC experimental analysis was performed to identify the reaction temperature of the alloying process, effect of ambient conditions on the alloying process. These experiments were conducted on the copper nitrate as precursor on the titania nanowires. The results showed the DSC peaks corresponds to the temperatures range of 175-180 deg C and 240-250 deg C. Additional controlled DSC experiments shown that the first stronger peak corresponds to the alloying reaction, whereas second weaker peak is correlated with the copper oxide formation from the decomposition reaction of copper

nitrate. Moreover, Gibbs free energy of hypothetical alloying reaction and decomposition of copper nitrate as a function temperature is calculated. Based on the calculations, Gibbs free energy of the titania with copper nitrate alloying reaction is favored at a lower temperature of 140 deg C, decomposition reaction of copper nitrate is favored at a temperature of 227 deg C. The obtained reaction Gibbs free energy calculations are in correlation with the DSC experimental data. It is most important to understand that the alloying reaction is competing with the decomposition reaction of nitrate precursor.

A hypothetical mechanism for the alloying of copper into the titania nanowires has been proposed based on experimental and theoretical information. Herein, copper nitrate precursor forms a non-continuous layer of copper nanoclusters (<1 nm) on the surface of titania nanowires. The intermediate layer could undergo competing reactions of alloying and decomposition. In alloying reaction, it is hypothesized that copper atoms are dissolved through the surface of titania NWs and undergoes the vacancy diffusion mechanism to diffuse into the bulk of the nanowire material. The vacant oxygen sites would counter diffuse to the surface of titania NWs during the bulk diffusion of copper atoms. This will further enhance the oxygen vacancy density on the surface of titania NWs and promote the copper nitrate reaction on the surface of titania nanowires.

Also, nickel alloyed titania nanowires were used in dry methane reforming reaction. This catalyst is compared with the nickel supported on titania. The activity of nickel alloyed titania nanowires yielded 96-97% for CO₂ conversion and 83-86% for methane conversion. The reaction was carried out for more than 50 hours for catalyst stability testing. In comparison, nickel supported on titania nanowires exhibited activity of 98-100% for CO₂ conversion and 55-58% methane conversion. The nickel alloyed titania catalyst showed

superior performance for dry methane reforming reaction in comparison to the nickel supported titania catalyst. In addition, the fresh and spent catalyst samples were analyzed with SEM image analysis, X-ray diffraction analysis, TGA analysis and TEM EDX elemental analysis. Material characterization results indicated that the fresh and spent catalyst of nickel alloyed titania are very similar. Whereas nickel supported titania samples morphology and composition was changed. Furthermore, materials characterization data revealed more insights into the catalyst performance such as the deposition carbon on the catalyst surface and sintering of nickel particles observed in nickel decorated titania nanowire catalyst. These results would confirm that the alloying in the nanowires helped with no carbon deposition on the catalyst surface and preventing the sintering of nickel particles at higher operating temperatures. The dual type of catalyst sites helped in activation of methane on the nickel surface and CO₂ activation on the oxygen vacant site.

An application of porous tin oxide with high grain boundaries for CO₂ reduction performance of porous Sn-pNWs, Sn-NWs, and Sn-NPs has been studied. It is concluded that the high-density grain boundary structure is a primary factor in the observed enhancement of the selectivity and rate of HCOOH formation and associated minimization of the H₂ evolution reaction during the electrochemical reduction of CO₂. Electrochemically reduced SnO₂ porous nanowire catalyst (Sn-pNWs) with a high density of grain boundaries (GBs) exhibits an energy conversion efficiency of CO₂ -into-HCOOH higher than analogous catalysts. HCOOH formation begins at lower overpotential (350 mV) and reaches a steady faradaic efficiency of ca. 80 % at only -0.8 V vs. RHE. The results for the Sn-pNWs were also compared to the literature-reported catalysts. The reported data show that Sn-pNWs can reduce CO₂ to formic acid more efficiently than the

current state-of-the-art electrodes. This includes Sn nanoparticles with a native oxide layer deposited on graphene as well as heat-treated Sn nano dendrite structures. With the demonstrated high selectivity for HCOOH formation, high current density at relatively low overpotential, high cathodic energy efficiency, robust chemical stability, and synthesis via a scalable plasma technique with demonstrated promise for bulk nanowire production, these Sn porous nanowire catalysts have promise for commercial conversion of waste CO₂ to valuable formic acid product.

To summarize, a viable, simple, and scalable method for the synthesis of mixed metal oxide nanowires has been demonstrated. It is based on the ex-situ solid state alloying of binary oxide nanowires with various solutes. Versatility of the method is validated by the synthesis of several mixed metal oxide NWs. Also, uniform ALD (atomic layer deposition) thin layer of solute is not necessary to obtain the mixed metal oxides nanowires. Extended solubility of solutes is obtained by using the solvent materials at nanoscale, potentially used to make various mixed metal oxide nanowires. A hypothetical mechanism for the alloying of copper into the titania nanowires has been proposed based on experimental data analysis. Also, mixed metal oxide nanowires of nickel alloyed titania showed superior performance for dry methane reforming reaction in comparison to the nickel supported titania catalyst. This is because of no carbon deposition on the catalyst surface and prevention of sintering of nickel particles at higher operating temperatures. The applicability of porous nanowires is verified with CO₂ electrochemical conversion to formic acid. The adsorption of reaction intermediates is favored by the presence of internal pores and by the presence of grain boundaries of the nanowires.

8.2 Recommendations for future work

Surface energy of nanowires is a key thermodynamic parameter in expanding the solute solubility in the nanowires. Although, this dissertation explained the solubility limit of the solutes, it is helpful to calculate the surface energy of NWs to estimate the solubility limit of solutes. Experimental determination of surface energy could be performed on the nanostructured materials by using the high temperature oxide melt calorimetry method. This technique uses a calvet type twinned microcalorimeter. It involves the dissolving the oxide mixture in molten lead borate at temperature $T=973$ K or $T=1073$ K. The difference in heat of solution or heat of drop of solution between the products and reactants gives the enthalpy of reaction. The value of enthalpy of reaction could be used to determine the Gibbs free energy as a function of temperature and to calculate the solubility limit of solute in the solvent material.

In this dissertation, X-ray diffraction analysis and TEM EDX elemental analysis are used to determine the lattice changes with alloying, distribution of alloyed atoms in the nanowires. However, to obtain more detailed information such as oxidation state solute in the alloyed material and chemical environment within the host lattice, X-ray absorption fine Structure spectroscopy (XANES (near-edge spectroscopy), EXAFS (extended X-ray absorption fine structure)) could be used. In the X-ray absorption spectroscopy, a core electron is excited to an empty state and X-ray absorption probes the unoccupied part of electronic structure of the system. This experiment would provide the information of alloyed atoms in the substitutional or interstitial sites. Furthermore, it will also provide additional details such as oxidation state of solute atoms, coordination number, distance of neighboring atoms, and disorder of neighboring atoms. Also, electron energy loss

spectroscopy (EELS) experimental analysis could be performed to extract the more information about the oxygen vacancies distribution along the surface to bulk of the nanowires. This would provide insights into the vacancy promoted diffusion mechanism.

Also, thermodynamic solubility of solutes could increase with the decrease in the dimensions of the solvent nanowires. Experimental studies related to the decrease in the diameter of nanowire could be performed. It is reported that the hydrogen plasma etching could reduce the dimensions of solvent nanowires. So, experimental studies under mild hydrogen plasma environment could be performed on the solvent NWs.

REFERENCES

1. ON, B. R. N. W.; Technology, S. S. f. E. R., <https://science.energy.gov/bes/community-resources/reports/>, Ed.
2. Yuan, C.; Wu, H. B.; Xie, Y.; Lou, X. W., Mixed Transition-Metal Oxides: Design, Synthesis, and Energy-Related Applications. *Angewandte Chemie International Edition* **2014**, *53* (6), 1488-1504.
3. Gawande, M. B.; Pandey, R. K.; Jayaram, R. V., Role of mixed metal oxides in catalysis science—versatile applications in organic synthesis. *Catalysis Science & Technology* **2012**, *2* (6), 1113-1125.
4. Liu, Y.; Mao, Z.-Q., Unconventional superconductivity in Sr₂RuO₄. *Physica C: Superconductivity and its Applications* **2015**, *514*, 339-353.
5. Chen, S.-H.; Jiang, Y.-S.; Lin, H.-y., Easy Synthesis of BiVO₄ for Photocatalytic Overall Water Splitting. *ACS Omega* **2020**, *5* (15), 8927-8933.
6. Pinheiro, A. N.; Firmiano, E. G. S.; Rabelo, A. C.; Dalmaschio, C. J.; Leite, E. R., Revisiting SrTiO₃ as a photoanode for water splitting: development of thin films with enhanced charge separation under standard solar irradiation. *RSC Advances* **2014**, *4* (4), 2029-2036.
7. Li, Y.; Pan, G. L.; Liu, J. W.; Gao, X. P., Preparation of Li₄Ti₅O₁₂ Nanorods as Anode Materials for Lithium-Ion Batteries. *Journal of The Electrochemical Society* **2009**, *156* (7), A495-A499.
8. Wang, T.; Ren, K.; He, M.; Dong, W.; Xiao, W.; Pan, H.; Yang, J.; Yang, Y.; Liu, P.; Cao, Z.; Ma, X.; Wang, H., Synthesis and Manipulation of Single-Crystalline Lithium Nickel Manganese Cobalt Oxide Cathodes: A Review of Growth Mechanism. *Front Chem* **2020**, *8*, 747-747.
9. Xia, Y.; Yang, P.; Sun, Y.; Wu, Y.; Mayers, B.; Gates, B.; Yin, Y.; Kim, F.; Yan, H., One-Dimensional Nanostructures: Synthesis, Characterization, and Applications. *Advanced Materials* **2003**, *15* (5), 353-389.
10. Wagner, R. S.; Ellis, W. C., VAPOR-LIQUID-SOLID MECHANISM OF SINGLE CRYSTAL GROWTH. *Applied Physics Letters* **1964**, *4* (5), 89-90.
11. Garnett, E.; Mai, L.; Yang, P., Introduction: 1D Nanomaterials/Nanowires. *Chemical Reviews* **2019**, *119* (15), 8955-8957.
12. Hochbaum, A. I.; Yang, P., Semiconductor Nanowires for Energy Conversion. *Chemical Reviews* **2010**, *110* (1), 527-546.
13. Yan, R.; Gargas, D.; Yang, P., Nanowire photonics. *Nature Photonics* **2009**, *3* (10), 569-576.
14. Tang, J.; Huo, Z.; Brittman, S.; Gao, H.; Yang, P., Solution-processed core-shell nanowires for efficient photovoltaic cells. *Nat Nanotechnol* **2011**, *6* (9), 568-72.
15. Patolsky, F.; Timko, B. P.; Yu, G.; Fang, Y.; Greytak, A. B.; Zheng, G.; Lieber, C. M., Detection, stimulation, and inhibition of neuronal signals with high-density nanowire transistor arrays. *Science* **2006**, *313* (5790), 1100-4.

16. Tian, B.; Lieber, C. M., Nanowired Bioelectric Interfaces. *Chemical Reviews* **2019**, *119* (15), 9136-9152.
17. Chen, C.; Fan, Y.; Gu, J.; Wu, L.; Passerini, S.; Mai, L., One-dimensional nanomaterials for energy storage. *Journal of Physics D: Applied Physics* **2018**, *51* (11), 113002.
18. Chu, Y.; Zhang, N.; Yang, J.; Wang, H.; Dai, Z.; Wang, L.; Gao, J.; Tan, X., Designed synthesis of thin CeO₂ nanowires-supported Pt electrocatalysts with pore-interconnected structure and its high catalytic activity for methanol oxidation. *Journal of Materials Science* **2018**, *53* (3), 2087-2101.
19. Dasgupta, N. P.; Sun, J.; Liu, C.; Brittman, S.; Andrews, S. C.; Lim, J.; Gao, H.; Yan, R.; Yang, P., 25th Anniversary Article: Semiconductor Nanowires – Synthesis, Characterization, and Applications. *Advanced Materials* **2014**, *26* (14), 2137-2184.
20. Resasco, J.; Dasgupta, N. P.; Rosell, J. R.; Guo, J.; Yang, P., Uniform Doping of Metal Oxide Nanowires Using Solid State Diffusion. *Journal of the American Chemical Society* **2014**, *136* (29), 10521-10526.
21. Yunarti, R. T.; Lee, M.; Hwang, Y. J.; Choi, J.-W.; Suh, D. J.; Lee, J.; Kim, I. W.; Ha, J.-M., Transition metal-doped TiO₂ nanowire catalysts for the oxidative coupling of methane. *Catalysis Communications* **2014**, *50* (Supplement C), 54-58.
22. Pan, Y.; Shen, X.; Yao, L.; Bentalib, A.; Peng, Z., Active Sites in Heterogeneous Catalytic Reaction on Metal and Metal Oxide: Theory and Practice. *Catalysts* **2018**, *8* (10).
23. Hansen, T. W.; DeLaRiva, A. T.; Challa, S. R.; Datye, A. K., Sintering of Catalytic Nanoparticles: Particle Migration or Ostwald Ripening? *Accounts of Chemical Research* **2013**, *46* (8), 1720-1730.
24. Kulkarni, A. S.; Jayaram, R. V., Liquid phase catalytic transfer hydrogenation of aromatic nitro compounds on La_{1-x}Sr_xFeO₃ perovskites prepared by microwave irradiation. *Journal of Molecular Catalysis A: Chemical* **2004**, *223* (1), 107-110.
25. Yang, X.-F.; Wang, A.; Qiao, B.; Li, J.; Liu, J.; Zhang, T., Single-Atom Catalysts: A New Frontier in Heterogeneous Catalysis. *Accounts of Chemical Research* **2013**, *46* (8), 1740-1748.
26. Ke, J.; Xiao, J.-W.; Zhu, W.; Liu, H.; Si, R.; Zhang, Y.-W.; Yan, C.-H., Dopant-Induced Modification of Active Site Structure and Surface Bonding Mode for High-Performance Nanocatalysts: CO Oxidation on Capping-free (110)-oriented CeO₂:Ln (Ln = La–Lu) Nanowires. *Journal of the American Chemical Society* **2013**, *135* (40), 15191-15200.
27. Wang, J.; Ji, Y.; Shao, Q.; Yin, R.; Guo, J.; Li, Y.; Huang, X., Phase and structure modulating of bimetallic CuSn nanowires boosts electrocatalytic conversion of CO₂. *Nano Energy* **2019**, *59*, 138-145.
28. Wang, D.; Chen, H.; Chang, G.; Lin, X.; Zhang, Y.; Aldalbahi, A.; Peng, C.; Wang, J.; Fan, C., Uniform Doping of Titanium in Hematite Nanorods for Efficient Photoelectrochemical Water Splitting. *ACS Applied Materials & Interfaces* **2015**, *7* (25), 14072-14078.
29. Vaddiraju, S.; Chandrasekaran, H.; Sunkara, M. K., Vapor Phase Synthesis of Tungsten Nanowires. *Journal of the American Chemical Society* **2003**, *125* (36), 10792-10793.

30. Vayssieres, L., Growth of Arrayed Nanorods and Nanowires of ZnO from Aqueous Solutions. *Advanced Materials* **2003**, *15* (5), 464-466.
31. Cao, G.; Liu, D., Template-based synthesis of nanorod, nanowire, and nanotube arrays. *Advances in colloid and interface science* **2008**, *136* (1-2), 45-64.
32. Wu, Y.; Yang, P., Direct Observation of Vapor–Liquid–Solid Nanowire Growth. *Journal of the American Chemical Society* **2001**, *123* (13), 3165-3166.
33. Lieber, C. M., One-dimensional nanostructures: Chemistry, physics & applications. *Solid State Communications* **1998**, *107* (11), 607-616.
34. Morales, A. M.; Lieber, C. M., A Laser Ablation Method for the Synthesis of Crystalline Semiconductor Nanowires. *Science* **1998**, *279* (5348), 208-211.
35. Kumar, V.; Kim, J. H.; Pendyala, C.; Chernomordik, B.; Sunkara, M. K., Gas-Phase, Bulk Production of Metal Oxide Nanowires and Nanoparticles Using a Microwave Plasma Jet Reactor. *The Journal of Physical Chemistry C* **2008**, *112* (46), 17750-17754.
36. Nguyen, T. Q.; Atla, V.; Vendra, V. K.; Thapa, A. K.; Jasinski, J. B.; Druffel, T. L.; Sunkara, M. K., Scalable solvo-plasma production of porous tin oxide nanowires. *Chemical Engineering Science* **2016**, *154*, 20-26.
37. Guo, X.; Zhu, H.; Si, M.; Jiang, C.; Xue, D.; Li, Q., Tuning the composition of Zn–Fe–O nanotube arrays: from zinc ferrite ZnFe₂O₄ to hematite α -Fe₂O₃. *CrystEngComm* **2013**, *15* (41), 8306-8313.
38. Du, N.; Xu, Y.; Zhang, H.; Yu, J.; Zhai, C.; Yang, D., Porous ZnCo₂O₄ Nanowires Synthesis via Sacrificial Templates: High-Performance Anode Materials of Li-Ion Batteries. *Inorganic Chemistry* **2011**, *50* (8), 3320-3324.
39. Jiang, H.; Ma, J.; Li, C., Hierarchical porous NiCo₂O₄ nanowires for high-rate supercapacitors. *Chemical Communications* **2012**, *48* (37), 4465-4467.
40. Ahmad, M.; Zhao, J.; Iqbal, J.; Miao, W.; Xie, L.; Mo, R.; Zhu, J., Conductivity enhancement by slight indium doping in ZnO nanowires for optoelectronic applications. *Journal of Physics D: Applied Physics* **2009**, *42* (16), 165406.
41. Zhang, Z.; Yi, J. B.; Ding, J.; Wong, L. M.; Seng, H. L.; Wang, S. J.; Tao, J. G.; Li, G. P.; Xing, G. Z.; Sum, T. C.; Alfred Huan, C. H.; Wu, T., Cu-Doped ZnO Nanoneedles and Nanonails: Morphological Evolution and Physical Properties. *The Journal of Physical Chemistry C* **2008**, *112* (26), 9579-9585.
42. Wu, D.; Yang, M.; Huang, Z.; Yin, G.; Liao, X.; Kang, Y.; Chen, X.; Wang, H., Preparation and properties of Ni-doped ZnO rod arrays from aqueous solution. *Journal of Colloid and Interface Science* **2009**, *330* (2), 380-385.
43. Greene, L. E.; Yuhas, B. D.; Law, M.; Zitoun, D.; Yang, P., Solution-Grown Zinc Oxide Nanowires. *Inorganic Chemistry* **2006**, *45* (19), 7535-7543.
44. Cho, I. S.; Lee, C. H.; Feng, Y.; Logar, M.; Rao, P. M.; Cai, L.; Kim, D. R.; Sinclair, R.; Zheng, X., Codoping titanium dioxide nanowires with tungsten and carbon for enhanced photoelectrochemical performance. *Nature Communications* **2013**, *4* (1), 1723.
45. He, J. H.; Lao, C. S.; Chen, L. J.; Davidovic, D.; Wang, Z. L., Large-Scale Ni-Doped ZnO Nanowire Arrays and Electrical and Optical Properties. *Journal of the American Chemical Society* **2005**, *127* (47), 16376-16377.
46. West, A. R., *Solid state chemistry and its applications*. John Wiley & Sons: 2014.
47. Chapter 2 - Experimental. In *Comprehensive Chemical Kinetics*, Bamford, C. H.; Tipper, C. F. H., Eds. Elsevier: 1980; Vol. 22, pp 17-39.

48. Wautelet, M.; Duvivier, D., The characteristic dimensions of the nanoworld. *European Journal of Physics* **2007**, *28* (5), 953-959.
49. Das, V. D.; Karunakaran, D., Thickness dependence of the phase transition temperature in Ag₂Se thin films. *Journal of Applied Physics* **1990**, *68* (5), 2105-2111.
50. Schlexer, P.; Andersen, A. B.; Sebok, B.; Chorkendorff, I.; Schiøtz, J.; Hansen, T. W., Size-Dependence of the Melting Temperature of Individual Au Nanoparticles. *Particle & Particle Systems Characterization* **2019**, *36* (3), 1800480.
51. Porter, D. A.; Easterling, K. E., *Phase transformations in metals and alloys (revised reprint)*. CRC press: 2009.
52. McLean, D.; Maradudin, A., Grain boundaries in metals. *Physics Today* **1958**, *11* (7), 35.
53. Straumal, B.; Baretzky, B.; Mazilkin, A.; Protasova, S.; Myatiev, A.; Straumal, P., Increase of Mn solubility with decreasing grain size in ZnO. *Journal of the European Ceramic Society* **2009**, *29* (10), 1963-1970.
54. Ma, C.; Navrotsky, A., Thermodynamics of the CoO–ZnO System at Bulk and Nanoscale. *Chemistry of Materials* **2012**, *24* (12), 2311-2315.
55. Koumoto, K.; Terasaki, I.; Funahashi, R., Complex Oxide Materials for Potential Thermoelectric Applications. *MRS Bulletin* **2006**, *31* (3), 206-210.
56. Hou, Y.; Zhuang, X.; Feng, X., Recent Advances in Earth-Abundant Heterogeneous Electrocatalysts for Photoelectrochemical Water Splitting. *Small Methods* **2017**, *1* (6), 1700090.
57. Védrine, J. C., Importance, features and uses of metal oxide catalysts in heterogeneous catalysis. *Chinese Journal of Catalysis* **2019**, *40* (11), 1627-1636.
58. Pal, A. S.; Singh, A.; Mandal, R. K.; Basu, J., Evolution of Microstructures and Interfaces in Compositionally Graded Mixed Oxide Thin Films for Nanoelectronics and Energy. *Microscopy and Microanalysis* **2019**, *25* (S2), 2298-2299.
59. Arora, A. K.; Vivek Sheel, J.; Singh, K.; Singh, R., Applications of Metal/Mixed Metal Oxides as Photocatalyst: (A Review). *Oriental Journal of Chemistry* **2016**, *32* (4), 2035-2042.
60. Šesták, J.; Berggren, G., Study of the kinetics of the mechanism of solid-state reactions at increasing temperatures. *Thermochimica Acta* **1971**, *3* (1), 1-12.
61. Ernst Koch, C. W., Formation of Ag₂HgI₄ from AgI and HgI₂ by reaction in solid state. *Physik Chem* **1936**, *B34* (3-4), 317-21.
62. Lindner, R., Formation of spinels and silicates by reactions in solid state investigated by method of radio active tracers. *Z. Elektrochem* **1955**, *50*(10), 967-70.
63. CARTER, R. E., Mechanism of Solid-state Reaction Between Magnesium Oxide and Aluminum Oxide and Between Magnesium Oxide and Ferric Oxide. *Journal of the American Ceramic Society* **1961**, *44* (3), 116-120.
64. Schmalzried, H., Solid-State Reactions. In *Treatise on Solid State Chemistry: Volume 4 Reactivity of Solids*, Hannay, N. B., Ed. Springer US: Boston, MA, 1976; pp 233-279.
65. Ikesue, A.; Furusato, I.; Kamata, K., Fabrication of Polycrystal line, Transparent YAG Ceramics by a Solid-State Reaction Method. *Journal of the American Ceramic Society* **1995**, *78* (1), 225-228.

66. Mizushima, K.; Jones, P. C.; Wiseman, P. J.; Goodenough, J. B., Li_xCoO_2 ($0 < x < 1$): A new cathode material for batteries of high energy density. *Materials Research Bulletin* **1980**, *15* (6), 783-789.
67. Ohzuku, T.; Ueda, A.; Yamamoto, N., Zero-Strain Insertion Material of $\text{Li}[\text{Li}_{1/3}\text{Ti}_{5/3}]\text{O}_4$ for Rechargeable Lithium Cells. *Journal of The Electrochemical Society* **1995**, *142* (5), 1431-1435.
68. Yabuuchi, N.; Ohzuku, T., Novel lithium insertion material of $\text{LiCo}_{1/3}\text{Ni}_{1/3}\text{Mn}_{1/3}\text{O}_2$ for advanced lithium-ion batteries. *Journal of Power Sources* **2003**, *119-121*, 171-174.
69. Zheng, J.; Hu, X.; Ren, Z.; Xue, X.; Chou, K., Solid-state Reaction Studies in $\text{Al}_2\text{O}_3\text{-TiO}_2$ System by Diffusion Couple Method. *ISIJ International* **2017**, *57* (10), 1762-1766.
70. Sung, Y.-M.; Lee, Y.-J.; Park, K.-S., Kinetic Analysis for Formation of $\text{Cd}_{1-x}\text{Zn}_x\text{Se}$ Solid-Solution Nanocrystals. *Journal of the American Chemical Society* **2006**, *128* (28), 9002-9003.
71. Huang, C.; Wang, X.; Liu, X.; Tian, M.; Zhang, T., Extensive analysis of the formation mechanism of BaSnO_3 by solid-state reaction between BaCO_3 and SnO_2 . *Journal of the European Ceramic Society* **2016**, *36* (3), 583-592.
72. Nagata, K.; Nishiwaki, R.; Nakamura, Y.; Maruyama, T., Kinetic mechanisms of the formations of MgCr_2O_4 and FeCr_2O_4 spinels from their metal oxides. *Solid State Ionics* **1991**, *49*, 161-166.
73. Zhong, Z.; Chen, K.; Ji, Y.; Yan, Q., Methane combustion over B-site partially substituted perovskite-type LaFeO_3 prepared by sol-gel method. *Applied Catalysis A: General* **1997**, *156* (1), 29-41.
74. Sun, Y. K.; Oh, I. H.; Hong, S. A., Synthesis of ultrafine LiCoO_2 powders by the sol-gel method. *Journal of Materials Science* **1996**, *31* (14), 3617-3621.
75. Kurian, J.; Mathew, M. J., Structural, optical and magnetic studies of CuFe_2O_4 , MgFe_2O_4 and ZnFe_2O_4 nanoparticles prepared by hydrothermal/solvothermal method. *Journal of Magnetism and Magnetic Materials* **2018**, *451*, 121-130.
76. Kim, Y. I.; Kim, D.; Lee, C. S., Synthesis and characterization of CoFe_2O_4 magnetic nanoparticles prepared by temperature-controlled coprecipitation method. *Physica B: Condensed Matter* **2003**, *337* (1), 42-51.
77. Fan, Y.; Wang, J.; Ye, X.; Zhang, J., Physical properties and electrochemical performance of $\text{LiNi}_{0.5}\text{Mn}_{1.5}\text{O}_4$ cathode material prepared by a coprecipitation method. *Materials Chemistry and Physics* **2007**, *103* (1), 19-23.
78. Gröhn, A. J.; Pratsinis, S. E.; Sánchez-Ferrer, A.; Mezzenga, R.; Wegner, K., Scale-up of Nanoparticle Synthesis by Flame Spray Pyrolysis: The High-Temperature Particle Residence Time. *Industrial & Engineering Chemistry Research* **2014**, *53* (26), 10734-10742.
79. Ritchie, R. H., Plasma Losses by Fast Electrons in Thin Films. *Physical Review* **1957**, *106* (5), 874-881.
80. Ajayi, B. P.; Kumari, S.; Jaramillo-Cabanzo, D.; Spurgeon, J.; Jasinski, J.; Sunkara, M., A rapid and scalable method for making mixed metal oxide alloys for enabling accelerated materials discovery. *Journal of Materials Research* **2016**, *31* (11), 1596-1607.

81. Ajayi, B. P., Plasma oxidation of liquid precursors for complex metal oxides. **2019**.
82. Cvelbar, U., Towards large-scale plasma-assisted synthesis of nanowires. *Journal of Physics D: Applied Physics* **2011**, *44* (17), 174014.
83. Nguyen, T. Q.; Atla, V.; Vendra, V. K.; Thapa, A. K.; Jasinski, J. B.; Druffel, T. L.; Sunkara, M. K., Scalable solvo-plasma production of porous tin oxide nanowires. *Chemical Engineering Science* **2016**, *154* (Supplement C), 20-26.
84. Yuan, L.; Wang, C.; Cai, R.; Wang, Y.; Zhou, G., Spontaneous ZnO nanowire formation during oxidation of Cu-Zn alloy. *Journal of Applied Physics* **2013**, *114* (2), 023512.
85. Zhao, Z.; Geng, F.; Cong, H.; Bai, J.; Cheng, H.-M., Low-temperature synthesis of Fe-doped ZnO nanorod bundles in aqueous solution. **2006**.
86. Zhou, X.; Peng, F.; Wang, H.; Yu, H., Boron and nitrogen-codoped TiO₂ nanorods: Synthesis, characterization, and photoelectrochemical properties. *Journal of Solid State Chemistry* **2011**, *184* (11), 3002-3007.
87. Jung, H.; Chun, S. H.; Seok, J.; Kim, Y. L.; Lee, S. J.; Kim, M. H.; Lee, N.-S., Single-crystalline ternary mixed metal oxide 1-dimensional nanostructures of Ir_{1-x-y}Ru_xV_yO₂ by vapour phase transport. *CrystEngComm* **2015**, *17* (34), 6476-6482.
88. Han, S.-J.; Jang, T.-H.; Kim, Y. B.; Park, B.-G.; Park, J.-H.; Jeong, Y. H., Magnetism in Mn-doped ZnO bulk samples prepared by solid state reaction. *Applied Physics Letters* **2003**, *83* (5), 920-922.
89. Li, F.; Wang, H.; Wang, L.; Wang, J., Magnetic properties of ZnFe₂O₄ nanoparticles produced by a low-temperature solid-state reaction method. *Journal of Magnetism and Magnetic Materials* **2007**, *309* (2), 295-299.
90. Teresa Buscaglia, M.; Harnagea, C.; Dapiaggi, M.; Buscaglia, V.; Pignolet, A.; Nanni, P., Ferroelectric BaTiO₃ Nanowires by a Topochemical Solid-State Reaction. *Chemistry of Materials* **2009**, *21* (21), 5058-5065.
91. Cao, J.; Guo, S.; Yan, R.; Zhang, C.; Guo, J.; Zheng, P., Carbon-coated single-crystalline LiMn₂O₄ nanowires synthesized by high-temperature solid-state reaction with high capacity for Li-ion battery. *Journal of Alloys and Compounds* **2018**, *741*, 1-6.
92. Deka, S.; Joy, P. A., Synthesis and magnetic properties of Mn doped ZnO nanowires. *Solid State Communications* **2007**, *142* (4), 190-194.
93. Nørskov, J. K.; Bligaard, T.; Rossmeisl, J.; Christensen, C. H., Towards the computational design of solid catalysts. *Nature Chemistry* **2009**, *1* (1), 37-46.
94. Yang, Y.; Niu, S.; Han, D.; Liu, T.; Wang, G.; Li, Y., Progress in Developing Metal Oxide Nanomaterials for Photoelectrochemical Water Splitting. *Advanced Energy Materials* **2017**, *7* (19), 1700555.
95. Yang, Y.; Ajmal, S.; Zheng, X.; Zhang, L., Efficient nanomaterials for harvesting clean fuels from electrochemical and photoelectrochemical CO₂ reduction. *Sustainable Energy & Fuels* **2018**, *2* (3), 510-537.
96. Goldstein, J. I.; Newbury, D. E.; Michael, J. R.; Ritchie, N. W.; Scott, J. H. J.; Joy, D. C., *Scanning electron microscopy and X-ray microanalysis*. Springer: 2017.
97. Goldstein, J.; Yakowitz, H., Practical scanning electron microscopy. **1975**.
98. Ma, G.; Wang, X., Synthesis and Applications of One-Dimensional Porous Nanowire Arrays: A Review. *Nano* **2015**, *10* (01), 1530001.

99. Serra, A.; Grau, S.; Gimbert-Surinach, C.; Sort, J.; Nogues, J.; Valles, E., Magnetically-actuated mesoporous nanowires for enhanced heterogeneous catalysis. *Applied Catalysis B-Environmental* **2017**, *217*, 81-91.
100. Alia, S. M.; Zhang, G.; Kisailus, D.; Li, D. S.; Gu, S.; Jensen, K.; Yan, Y. S., Porous Platinum Nanotubes for Oxygen Reduction and Methanol Oxidation Reactions. *Advanced Functional Materials* **2010**, *20* (21), 3742-3746.
101. Kumar, B.; Atla, V.; Brian, J. P.; Kumari, S.; Nguyen, T. Q.; Sunkara, M.; Spurgeon, J. M., Reduced SnO₂ porous nanowires with a high density of grain boundaries as catalysts for efficient electrochemical CO₂-into-HCOOH conversion. *Angewandte Chemie International Edition* **2017**, *56* (13), 3645-3649.
102. Meduri, P.; Pendyala, C.; Kumar, V.; Sumanasekera, G. U.; Sunkara, M. K., Hybrid Tin Oxide Nanowires as Stable and High Capacity Anodes for Li-Ion Batteries. *Nano Letters* **2009**, *9* (2), 612-616.
103. Kolmakov, A.; Potluri, S.; Barinov, A.; Menteş, T. O.; Gregoratti, L.; Niño, M. A.; Locatelli, A.; Kiskinova, M., Spectromicroscopy for Addressing the Surface and Electron Transport Properties of Individual 1-D Nanostructures and Their Networks. *ACS Nano* **2008**, *2* (10), 1993-2000.
104. Wang, Y.; Jiang, X.; Xia, Y., A Solution-Phase, Precursor Route to Polycrystalline SnO₂ Nanowires That Can Be Used for Gas Sensing under Ambient Conditions. *Journal of the American Chemical Society* **2003**, *125* (52), 16176-16177.
105. Wang, Q.; Wang, D.; Wang, T., Shape-controlled Synthesis of Porous SnO₂ Nanostructures via Morphologically Conserved Transformation from SnC₂O₄ Precursor Approach. *Nano-Micro Letters* **2011**, *3* (1), 34-42.
106. Kolmakov, A.; Zhang, Y.; Cheng, G.; Moskovits, M., Detection of CO and O₂ Using Tin Oxide Nanowire Sensors. *Advanced Materials* **2003**, *15* (12), 997-1000.
107. Zhang, J.; Guo, J.; Xu, H.; Cao, B., Reactive-Template Fabrication of Porous SnO₂ Nanotubes and Their Remarkable Gas-Sensing Performance. *ACS Applied Materials & Interfaces* **2013**, *5* (16), 7893-7898.
108. Li, Y.; Somorjai, G. A., Nanoscale Advances in Catalysis and Energy Applications. *Nano Letters* **2010**, *10* (7), 2289-2295.
109. Waitz, T.; Becker, B.; Wagner, T.; Sauerwald, T.; Kohl, C. D.; Tiemann, M., Ordered nanoporous SnO₂ gas sensors with high thermal stability. *Sensors and Actuators B: Chemical* **2010**, *150* (2), 788-793.
110. Ye, J.; Zhang, H.; Yang, R.; Li, X.; Qi, L., Morphology-Controlled Synthesis of SnO₂ Nanotubes by Using 1D Silica Mesostructures as Sacrificial Templates and Their Applications in Lithium-Ion Batteries. *Small* **2010**, *6* (2), 296-306.
111. Sunkara, M. K.; Kumar, V.; Kim, J. H.; Clark, E. L., Methods for synthesizing metal oxide nanowires. Google Patents: 2013.
112. Zhang, M.; Jin, Z.; Zhang, J.; Guo, X.; Yang, J.; Li, W.; Wang, X.; Zhang, Z., Effect of annealing temperature on morphology, structure and photocatalytic behavior of nanotubed H₂Ti₂O₄(OH)₂. *Journal of Molecular Catalysis A: Chemical* **2004**, *217* (1), 203-210.
113. Feist, T. P.; Davies, P. K., The soft chemical synthesis of TiO₂ (B) from layered titanates. *Journal of Solid State Chemistry* **1992**, *101* (2), 275-295.

114. Dadfar, M. R.; Rahimipour, M. R.; Vaezi, M. R.; Gholamzadeh, A., Characterization of Yttria Stabilized Zirconia/Titania core-shell powders synthesized via air plasma spray method. *Materials Chemistry and Physics* **2017**, *200*, 280-286.
115. Nie, J.; Chan, J. M.; Qin, M.; Zhou, N.; Luo, J., Liquid-like grain boundary complexion and sub-eutectic activated sintering in CuO-doped TiO₂. *Acta Materialia* **2017**, *130*, 329-338.
116. Misra, S. K.; Chaklader, A. C. D., The System Copper Oxide—Alumina. *Journal of the American Ceramic Society* **1963**, *46* (10), 509-509.
117. Van Orman, J. A.; Crispin, K. L., Diffusion in oxides. *Reviews in Mineralogy and Geochemistry* **2010**, *72* (1), 757-825.
118. Park, T.-J.; Levchenko, A. A.; Zhou, H.; Wong, S. S.; Navrotsky, A., Shape-dependent surface energetics of nanocrystalline TiO₂. *Journal of Materials Chemistry* **2010**, *20* (39), 8639-8645.
119. Akse, J. R.; Whitehurst, H. B., Diffusion of titanium in slightly reduced rutile. *Journal of Physics and Chemistry of Solids* **1978**, *39* (5), 457-465.
120. Akri, M.; Zhao, S.; Li, X.; Zang, K.; Lee, A. F.; Isaacs, M. A.; Xi, W.; Gangarajula, Y.; Luo, J.; Ren, Y.; Cui, Y.-T.; Li, L.; Su, Y.; Pan, X.; Wen, W.; Pan, Y.; Wilson, K.; Li, L.; Qiao, B.; Ishii, H.; Liao, Y.-F.; Wang, A.; Wang, X.; Zhang, T., Atomically dispersed nickel as coke-resistant active sites for methane dry reforming. *Nature Communications* **2019**, *10* (1), 5181.
121. Kim, J. H.; Suh, D. J.; Park, T. J.; Kim, K. L., Effect of metal particle size on coking during CO₂ reforming of CH₄ over Ni-alumina aerogel catalysts. *Applied Catalysis A: General* **2000**, *197* (2), 191-200.
122. Vogt, C.; Kranenborg, J.; Monai, M.; Weckhuysen, B., Structure Sensitivity in Steam and Dry Methane Reforming over Nickel: Activity and Carbon Formation. *ACS Catalysis* **2019**, XXXX.
123. Dayton, L., Atmospheric carbon dioxide soars past crucial milestone. *Science* May. 16, 2016
124. Myers, S. S.; Wessells, K. R.; Kloog, I.; Zanobetti, A.; Schwartz, J., Effect of increased concentrations of atmospheric carbon dioxide on the global threat of zinc deficiency: a modelling study. *The Lancet Global Health* **2015**, *3* (10), e639-e645.
125. Kirschbaum, M. U. F.; Medlyn, B. E.; King, D. A.; Pongracic, S.; Murty, D.; Keith, H.; Khanna, P. K.; Snowdon, P.; Raison, R. J., Modelling forest-growth response to increasing CO₂ concentration in relation to various factors affecting nutrient supply. *Global Change Biology* **1998**, *4* (1), 23-41.
126. Karl, T. R.; Trenberth, K. E., Modern Global Climate Change. *Science* **2003**, *302* (5651), 1719-1723.
127. Mikkelsen, M.; Jorgensen, M.; Krebs, F. C., The teraton challenge. A review of fixation and transformation of carbon dioxide. *Energy & Environmental Science* **2010**, *3* (1), 43-81.
128. García-España, E.; Gaviña, P.; Latorre, J.; Soriano, C.; Verdejo, B., CO₂ Fixation by Copper(II) Complexes of a Terpyridinophane Aza Receptor. *Journal of the American Chemical Society* **2004**, *126* (16), 5082-5083.
129. Sanna, A.; Uibu, M.; Caramanna, G.; Kuusik, R.; Maroto-Valer, M. M., A review of mineral carbonation technologies to sequester CO₂. *Chemical Society Reviews* **2014**, *43* (23), 8049-8080.

130. Notni, J.; Schenk, S.; Görls, H.; Breitzke, H.; Anders, E., Formation of a Unique Zinc Carbamate by CO₂ Fixation: Implications for the Reactivity of Tetra-Azamacrocyclic Ligated Zn(II) Complexes. *Inorganic Chemistry* **2008**, *47* (4), 1382-1390.
131. Xu; Moulijn, J. A., Mitigation of CO₂ by Chemical Conversion: Plausible Chemical Reactions and Promising Products. *Energy & Fuels* **1996**, *10* (2), 305-325.
132. Kumar, B.; Brian, J. P.; Atla, V.; Kumari, S.; Bertram, K. A.; White, R. T.; Spurgeon, J., New trends in the development of heterogeneous catalysts for electrochemical CO₂ reduction. *Catalysis Today* **2016**, *270*, 19-30.
133. Qiao, J.; Liu, Y.; Hong, F.; Zhang, J., A review of catalysts for the electroreduction of carbon dioxide to produce low-carbon fuels. *Chemical Society Reviews* **2014**, *43* (2), 631-675.
134. Schreier, M.; Curvat, L.; Giordano, F.; Steier, L.; Abate, A.; Zakeeruddin, S. M.; Luo, J.; Mayer, M. T.; Gratzel, M., Efficient photosynthesis of carbon monoxide from CO₂ using perovskite photovoltaics. *Nat Commun* **2015**, *6*.
135. Liu, C.; Colón, B. C.; Ziesack, M.; Silver, P. A.; Nocera, D. G., Water splitting–biosynthetic system with CO₂ reduction efficiencies exceeding photosynthesis. *Science* **2016**, *352* (6290), 1210-1213.
136. Costentin, C.; Robert, M.; Saveant, J.-M., Catalysis of the electrochemical reduction of carbon dioxide. *Chemical Society Reviews* **2013**, *42* (6), 2423-2436.
137. Kumar, B.; Llorente, M.; Froehlich, J.; Dang, T.; Sathrum, A.; Kubiak, C. P., Photochemical and Photoelectrochemical Reduction of CO₂. *Annual Review of Physical Chemistry* **2012**, *63* (1), 541-569.
138. Baruch, M. F.; Pander, J. E.; White, J. L.; Bocarsly, A. B., Mechanistic Insights into the Reduction of CO₂ on Tin Electrodes using in Situ ATR-IR Spectroscopy. *ACS Catalysis* **2015**, *5* (5), 3148-3156.
139. Zhang, S.; Kang, P.; Meyer, T. J., Nanostructured Tin Catalysts for Selective Electrochemical Reduction of Carbon Dioxide to Formate. *Journal of the American Chemical Society* **2014**, *136* (5), 1734-1737.
140. Chen, Y.; Kanan, M. W., Tin Oxide Dependence of the CO₂ Reduction Efficiency on Tin Electrodes and Enhanced Activity for Tin/Tin Oxide Thin-Film Catalysts. *Journal of the American Chemical Society* **2012**, *134* (4), 1986-1989.
141. Singh, A. K.; Singh, S.; Kumar, A., Hydrogen energy future with formic acid: a renewable chemical hydrogen storage system. *Catalysis Science & Technology* **2016**, *6* (1), 12-40.
142. Mellmann, D.; Sponholz, P.; Junge, H.; Beller, M., Formic acid as a hydrogen storage material - development of homogeneous catalysts for selective hydrogen release. *Chemical Society Reviews* **2016**, *45* (14), 3954-3988.
143. Hori, Y.; Wakebe, H.; Tsukamoto, T.; Koga, O., Electrocatalytic process of CO selectivity in electrochemical reduction of CO₂ at metal electrodes in aqueous media. *Electrochimica Acta* **1994**, *39* (11), 1833-1839.
144. Wu, J.; Risalvato, F. G.; Ma, S.; Zhou, X.-D., Electrochemical reduction of carbon dioxide III. The role of oxide layer thickness on the performance of Sn electrode in a full electrochemical cell. *Journal of Materials Chemistry A* **2014**, *2* (6), 1647-1651.

145. Bumroongsakulsawat, P.; Kelsall, G. H., Effect of solution pH on CO: formate formation rates during electrochemical reduction of aqueous CO₂ at Sn cathodes. *Electrochimica Acta* **2014**, *141*, 216-225.
146. Won, D. H.; Choi, C. H.; Chung, J.; Chung, M. W.; Kim, E.-H.; Woo, S. I., Rational Design of a Hierarchical Tin Dendrite Electrode for Efficient Electrochemical Reduction of CO₂. *ChemSusChem* **2015**, *8* (18), 3092-3098.
147. Feng, X.; Jiang, K.; Fan, S.; Kanan, M. W., Grain-Boundary-Dependent CO₂ Electroreduction Activity. *Journal of the American Chemical Society* **2015**, *137* (14), 4606-4609.
148. Li, C. W.; Ciston, J.; Kanan, M. W., Electroreduction of carbon monoxide to liquid fuel on oxide-derived nanocrystalline copper. *Nature* **2014**, *508* (7497), 504-507.
149. Feng, X.; Jiang, K.; Fan, S.; Kanan, M. W., A Direct Grain-Boundary-Activity Correlation for CO Electroreduction on Cu Nanoparticles. *ACS Central Science* **2016**, *2* (3), 169-174.
150. Kim, K.-S.; Kim, W. J.; Lim, H.-K.; Lee, E. K.; Kim, H., Tuned Chemical Bonding Ability of Au at Grain Boundaries for Enhanced Electrochemical CO₂ Reduction. *ACS Catalysis* **2016**, *6* (7), 4443-4448.
151. Nguyen, T. Q.; Atla, V.; Vendra, V. K.; Thapa, A. K.; Jasinski, J. B.; Druffel, T. L.; Sunkara, M. K., Scalable solvo-plasma production of porous tin oxide nanowires. *Chemical Engineering Science*.
152. Wu, J.; Sharma, P. P.; Harris, B. H.; Zhou, X.-D., Electrochemical reduction of carbon dioxide: IV dependence of the Faradaic efficiency and current density on the microstructure and thickness of tin electrode. *Journal of Power Sources* **2014**, *258*, 189-194.
153. Kim, H.-Y.; Choi, I.; Ahn, S. H.; Hwang, S. J.; Yoo, S. J.; Han, J.; Kim, J.; Park, H.; Jang, J. H.; Kim, S.-K., Analysis on the effect of operating conditions on electrochemical conversion of carbon dioxide to formic acid. *International Journal of Hydrogen Energy* **2014**, *39* (29), 16506-16512.
154. Watanabe, M.; Shibata, M.; Kato, A.; Azuma, M.; Sakata, T., Design of Alloy Electrocatalysts for CO₂ Reduction: III. The Selective and Reversible Reduction of on Cu Alloy Electrodes. *Journal of The Electrochemical Society* **1991**, *138* (11), 3382-3389.
155. Asadi, M.; Kumar, B.; Behranginia, A.; Rosen, B. A.; Baskin, A.; Reppin, N.; Pisasale, D.; Phillips, P.; Zhu, W.; Haasch, R.; Klie, R. F.; Král, P.; Abiade, J.; Salehi-Khojin, A., Robust carbon dioxide reduction on molybdenum disulphide edges. *Nat Commun* **2014**, *5*.
156. Asadi, M.; Kim, K.; Liu, C.; Addepalli, A. V.; Abbasi, P.; Yasaei, P.; Phillips, P.; Behranginia, A.; Cerrato, J. M.; Haasch, R.; Zapol, P.; Kumar, B.; Klie, R. F.; Abiade, J.; Curtiss, L. A.; Salehi-Khojin, A., Nanostructured transition metal dichalcogenide electrocatalysts for CO₂ reduction in ionic liquid. *Science* **2016**, *353* (6298), 467-470.
157. Lu, Q.; Rosen, J.; Zhou, Y.; Hutchings, G. S.; Kimmel, Y. C.; Chen, J. G.; Jiao, F., A selective and efficient electrocatalyst for carbon dioxide reduction. *Nat Commun* **2014**, *5*.

CURRICULUM VITAE

Veerendra Atla

✉ veerendra.atla@louisville.edu

LinkedIn  <https://www.linkedin.com/in/veerendra-atla-22071815/>

Qualifications Summary

Working as associate research engineer and graduate research assistant with experience in materials design and synthesis research, developing new production procedures for nanowire materials scaleup, equipment maintenance, data analysis. Currently focuses on the development of mixed metal oxides nanowires for energy storage, energy conversion and heterogenous catalysis related applications. Equipment handling and troubleshooting experience with the nanowire materials production equipment such as vacuum furnaces, belt furnace, box furnaces, mixing tanks, belt filter, atmospheric plasma reactors, ALD thin film processing, PE-CVD reactors and fixed bed reactors. Hands on experience with the sample analysis tools like XRD, SEM, EDX, Raman, BET analysis, DSC-TGA and gas chromatography.

Education & Certification

-**University of Louisville (UofL), Louisville - Kentucky, United States** (2014 – Present)

- **Degree:** Ph.D. Chemical Engineering (CGPA 4.0/4.0)
- **Advisor:** Mahendra K. Sunkara, PhD
- **PhD Dissertation Title:** Mixed metal oxides nanowires via solid state alloying and related applications.

- **Indian Institute of Technology, Bombay, India** (2008 – 2010)

- **Degree:** M.Tech. Chemical Engineering (CGPA 4.2/5.0)
- **Advisor:** A.S. Moharir, PhD
- **MS Thesis Title:** Simulation studies on hydrogen Pressure Swing Adsorption process

- **Jawaharlal Nehru Technological University, Hyderabad, India** (2004 – 2008)

- **Degree:** B.Tech. Chemical Engineering (percentage 74.9/100)
- **Advisor:** B.Srinivas, PhD
- **Project Title:** Simulation of multiple feed/product distillation column

Experience

December 2017 – 2020 |Advanced Energy Materials LLC, Louisville, KY

Position: Associate Research Engineer (Intern)

Outline: Research development and commercial scale production of mixed metal oxide nanowire materials for energy storage, energy conversion and hydrodesulfurization catalyst products.

Key responsibilities:

- Synthesis of mixed metal oxide nanowire materials (Ni-ZnO, CuO-ZnO, Ni-Mo-TiO₂ nanowire materials).
- Advanced method to produce large quantities of spinel phase lithium titanate (LTO) nanowire as anode materials for lithium ion batteries.
- Analysis and evaluation of nanowire materials and reaction products with FE-SEM, EDX, XRD, BET, Raman, TGA-DSC and GC analysis tools.
- Develop new production procedures for commercial scale up of nanowire materials (in Kg's to

tons scale). Involved in handling and troubleshooting of production equipment's such as belt furnace, belt filter, mixing tanks, vacuum furnaces, box furnaces and atmospheric plasma reactor.

- Designed an atmospheric plasma catalysis reactor for CO₂ to methanol conversion, a DOE funded project

Key achievement:

- First to develop commercially scaled lithium titanate nanowire material for LTO battery anode application. Synthesized and tested the LTO nanowire-based anode material in lithium ion battery full cell configuration.

August 2014 – 2017| Conn Center for Renewable Energy Research, UofL, Louisville, KY

Position: Graduate Research Assistant

Outline: Developed solid state alloying method to produce mixed metal oxides nanowires with applications in energy conversion and storage technologies.

Key responsibilities:

- Design of mixed metal oxide nanowires material with various metal oxide systems such as Cu/TiO₂, Ni/TiO₂, Cu/Al₂O₃, Ni/WO₃, LiAlO₂, Li₄Ti₅O₁₂ (LTO) etc.
- Application of Ni/TiO₂ alloyed nanowire catalyst material in DMR (Dry Methane Reforming reaction) yielded a high CO₂ conversion of 80-100% and Methane with (CH₄)-55-86%. The test was performed in a custom designed continuous packed bed reactor.
- Synthesis of various metal oxide nano materials (SnO₂, TiO₂, WO₃) using the solvo plasma technology (using an atmospheric plasma flame reactor).
- Application of developed nanowire materials also tested in electrochemical conversion of CO₂ to formate and also used in the chemical adsorption of CO₂.
- Determination of structure-property relationships through characterization techniques such as FE-SEM, EDX, XRD, Raman, BET and TGA-DSC etc.
- Advanced crystallographic analysis with software ("GSAS") using the Rietveld method.
- Maintain laboratory instruments and enforce OSHA safety practices and high-quality lab documentation.

Key achievement:

- First to report new nanowire-based materials for the CO₂ electrochemical conversion and capture applications with high efficiencies and with a scalable nanowire synthesis process.
- High activity obtained with Ni/TiO₂ alloyed nanowire catalyst material in DMR (Dry Methane Reforming reaction), yielded a high CO₂ conversion of 80-100% and Methane (CH₄) conversion of 55-86% based on the reaction conditions.

Aug. 2010 – June 2014| RGU IIIT, Nuzvid, India

Position: Lecturer, Dept. of Chemical Engineering

Outline: Worked as lecturer to teach undergraduate students

Key responsibilities:

- Taught undergraduate courses such as chemical engineering thermodynamics, fluid mechanics, Numerical Methods for Chemical Engineering, Chemical Technology.
- Established undergraduate laboratories such as Fluid mechanics laboratory, Process control laboratory.

Sept. 2008 - May 2010| Indian Institute of Technology, Bombay, India

Position: Graduate Research Assistant

Outline: Simulation studies on hydrogen Pressure Swing Adsorption process to separate hydrogen from flue gas mixture using matlab

Key responsibilities:

- Studied Pressure Swing Adsorption (PSA) process to separate hydrogen from typical cracked gas mixture of (CO₂/CO/CH₄/H₂) to get purity of hydrogen by 99.99%. Mathematical modelling of adsorption column was done by using a detailed isothermal model and these equations are solved numerically by using MATLAB.

Patent

M. K. Sunkara, Vivekanand Kumar, **Veerendra Atla** (2018) "Spinel Lithium Titanium Oxide (LTO) Nanowire Anode Material for Lithium-Ion Batteries" U.S. Patent Application No. 16554619

Publications

Total Publications = 11, h-index = 7, i10 index=6, Total Citations = 542

1. Dharmasena, R.; Martinez-Garcia, A.; **Atla, V.**; Akram, M. Z.; Sumanasekera, G.; Sunkara, M. K., Lithium Molybdate (Li₂MoO₃) – Sulfur Battery. Batteries & Supercaps 2019(# of cit.= 1).
2. §Akram, M. Z.; §**Atla, V.**; Nambo, A.; Ajayi, B. P.; Jasinski, J. B.; He, J.; Gong, J. R.; Sunkara, M., Low-Temperature and Fast Kinetics for CO₂ Sorption Using Li₆WO₆ Nanowires. Nano Letters 2018, 18 (8), 4891-4899. (# of cit.= 4) (§**Authors contribute equally to this work**)
3. Akram, M. Z.; Thapa, A. K.; Ajayi, B. P.; **Atla, V.**; Gong, J. R.; Sunkara, M. K., A New Nanowire-Based Lithium Hexaoxotungstate Anode for Lithium-Ion Battery. Nanoscale Advances 2019(# of cit.= 2)..
4. Nambo, A.; He, J.; Nguyen, T. Q.; **Atla, V.**; Druffel, T.; Sunkara, M., Ultrafast Carbon Dioxide Sorption Kinetics Using Lithium Silicate Nanowires. Nano Letters 2017, 17 (6), 3327-3333. (# of cit.= 35)
5. Nguyen, T. Q.; **Atla, V.**; Venda, V. K.; Thapa, A. K.; Jasinski, J. B.; Druffel, T. L.; Sunkara, M. K., Scalable solvo-plasma production of porous tin oxide nanowires. Chemical Engineering Science 2016, 154, 20-26. (# of cit.= 12)
6. §Kumar, B.; §**Atla, V.**; Brian, J. P.; Kumari, S.; Nguyen, T. Q.; Sunkara, M.; Spurgeon, J. M., Reduced SnO₂ Porous Nanowires with a High Density of Grain Boundaries as Catalysts for Efficient Electrochemical CO₂-into-HCOOH Conversion. Angewandte Chemie International Edition 2017, 56 (13), 3645-3649. (# of cit.= 207) (§**Authors contribute equally to this work**)
7. Kumar, B.; Brian, J. P.; **Atla, V.**; Kumari, S.; Bertram, K. A.; White, R. T.; Spurgeon, J. M., Controlling the Product Syngas H₂:CO Ratio through Pulsed-Bias Electrochemical Reduction of CO₂ on Copper. ACS Catalysis 2016, 6 (7), 4739-4745. (# of cit.= 38)
8. Kumar, B.; Brian, J. P.; **Atla, V.**; Kumari, S.; Bertram, K. A.; White, R. T.; Spurgeon, J. M., New trends in the development of heterogeneous catalysts for electrochemical CO₂ reduction. Catalysis Today 2016, 270, 19-30. (# of cit.= 203)
9. Rao, K. R.; Pishgar, S.; Strain, J.; Kumar, B.; **Atla, V.**; Kumari, S.; Spurgeon, Joshua M., Photoelectrochemical reduction of CO₂ to HCOOH on silicon photocathodes with reduced SnO₂ porous nanowire catalysts. Journal of Materials Chemistry A 2018, 6 (4), 1736-1742. (# of cit.= 24)
11. **Veerendra Atla**, M.Z. Akram, M.K. Sunkara, "Mixed metal oxide nanowires Via solid state alloying" (in progress)

Selected Presentations

1. He, J.; Vasireddy, S.; Nguyen, T.; **Atla, V.**; Guhy, L.; Sunkara, M.; In Novel Hydro-Desulfurization Catalysts for Hydrocarbon Fuels, 2019 North American Catalysis Society Meeting, NAM: 2019.
2. "Fast CO₂ Sorption Kinetics Using Nanowire Based Materials" Mahendra Kumar Sunkara, Apolo Nambo, **Veerendra Atla** and Muhammed Zain, ECS Meeting Abstracts-2018
3. **Veerendra Atla**, Tu Nguyen, M. Sunkara, "Solvo Plasma synthesis of porous tin oxide nanowires", Renewable Energy & Energy Efficiency (RE³) Workshop, Louisville, Kentucky, March 2015

Honors and Awards

- University of Louisville Ph.D. Fellowship, 2014-2016
- Indian Institute of Technology, Graduate Assistantship, Bombay 2008